EUMETSAT

The Meteosat Surface Albedo Climate Data Record Validation Report

Doc.No. : EUM/OPS/REP/13/726421
Issue : v1B
Date : 8 December 2014
WBS :

EUMETSAT
Eumetsat-Allee 1, D-64295 Darmstadt, Germany
Tel: +49 6151 807-7
Fax: +49 6151 807 555
http://www.eumetsat.int

© EUMETSAT
The copyright of this document is the property of EUMETSAT.

Document Change Record

Issue / Revision	*Date*	*DCN. No*	*Summary of Changes*
1	16 October 2013		Initial version created.
1A	28 April 2014		Document revised to update validation results.
1B	8 December 2014		Make a more clear reference to the ALBEDOVAL study done by Fell et al. 2012 in the Purpose and Scope part.

Table of Contents

1 Introduction 7
1.1 Purpose and Scope 7
1.2 Document Structure 7
1.3 Applicable Documents 7
1.4 Reference Documents 7
1.5 User Requirements 8
1.6 The Evaluation Strategy 8
1.7 Terminology Specific to this Validation 9
2 Meteosat surface albedo Technical Description 10
2.1 The Meteosat Surface Albedo (MSA) Product 10
2.1.1 The Meteosat Visible and Infrared Imager (MVIRI) 10
2.1.2 Nominal coverage areas and periods 10
2.1.3 The MSA Scientific Approach 13
2.1.4 MSA implementation overview 14
2.1.5 MSA Implementation Details 15
3 Data used for the validation 18
3.1 Surface Albedo Using *in situ* Data 18
3.1.1 Availability 18
3.1.2 Scaling Up to MSA Pixel Size 20
3.2 Satellite-derived Surface Albedo Values 20
3.3 Other relevant datasets 21
3.4 Reference sites 21
3.4.1 Site selection 21
3.4.2 Surface characterisation 22
4 Evaluation of the MSA dataset 23
4.1 Product availability 23
4.2 Pixel navigation 24
4.2.1 Results overview 24
4.2.2 Scene selection 25
4.2.3 Evaluation methods 26
4.2.4 Average Navigation Offsets between Different satellites 27
4.2.5 Variations for individual satellites 28
4.3 MVIRI Stability and Consistency 30
4.3.1 Site selection 30
4.3.2 Time Series for Selected Sites 30
4.4 Aerosol effects 32
4.4.1 Aerosol optical thickness against AERONET 32
4.4.2 Spatial analysis using MACC-II 34
4.4.3 Analysis using AERONET data 38
4.5 Angular Effects 39
4.5.1 Spatial Analysis 40
4.5.2 Temporal Analysis 42
4.5.3 Conclusions on angular effects 43
4.6 Satellite to Satellite Data Comparisons 44
4.6.1 Comparing MSA with Geostationary Products 44
4.6.2 MSA with Polar-orbiting Products 48
4.7 Cloud Screening 49
4.8 Comparison with Surface Reference Sites: MODIS Era 51
4.9 Comparison with Surface Reference Sites: Pre-MODIS Era 55
4.9.1 Validation Summary Files 55
4.10 Comparison with MSA 56

5 Summary and conclusions 58
5.1 Summary of findings 58
5.1.1 General findings 58
5.1.2 MSA strengths 59
5.1.3 MSA Weaknesses 59
5.2 MSA requirement matching 60
5.3 Conclusions 61
Annex A: 62
5.4 A.1 Reference data 62
5.4.1 A.1.1 In-situ Surface Albedo 62
5.4.4 A.1.2 Satellite-Derived Surface Albedo 63
5.4.7 A.1.3 Ancillary Data 64
5.6 A.1.4 Reference Surface Targets 65
Annex B: GCOS Climate Monitoring Principles 66
Annex C: MSA time series at Selected Sites 67
5.7 C.1 Murzuq Desert 67
5.8 C.2 Libya 68
5.9 C.3 Egypt One 69
5.10 C.4 Omani Desert 70
5.11 C.5 Toravere 71
5.12 C.6 Moldova 71
5.13 C.7 Mongu 73
5.14 C.8 Skukuza 74
5.15 C.3 Solar Village 75
Appendix D: Georeferencing software 76
5.16 D.1 MPEF_georef.pro: latitude/longitude to column/row 76
5.16.1 D.2 MPEF_refgeo.pro: column/row to latitude/longitude 76
5.16.2 D.3 Georeferencing Example 77
Appendix E: Scientific References 78
Appendix E: Acronyms and Terms Used in this Document 83

List of Figures

Figure 1: Sensor spectral response of the MVIRI VIS band for Meteosat First Generation satellites…10
Figure 2: The five different coverage areas in native MSA projection. 12
Figure 3: MSA retrieval scheme. Observations accumulated during the day are used as an angular sampling of the surface. 13
Figure 4: Example of the data consistency procedure (DCP) for MVIRI-7. Green: BRF from MVIRI measurements. Blue: Best-fit. 16
Figure 5. Aerial image of the area around the BSRN site (red-white symbol) at Toravere, Estonia The typical extension of a MODIS pixel is shown by the black square. An MSA pixel would roughly cover the whole area shown [Image source: Google Earth]. 19
Figure 6. FLUXNET sites within the MVIRI 0DEG field-of-view taking albedo measurements. Green dots represent sites with sufficient plant cover homogeneity at a 1 km² scale. 19
Figure 7: MSA temporal coverage for 0DEG and IODC. Note that Meteosat-5 was positioned at 57°E over the IODC whereas Meteosat-7 is located at 63°E. 23
Figure 8: Practical MSA availability for 0DEG, IODC_57 and IODC_63. White areas do not supply any data. Black areas can provide MSA data occasionally. 24
Figure 9: Reference coastlines used for studying MSA geo-location stability and accuracy.. 25
Figure 10: Example of MVIRI-7 time series of BHR_{ISO} for pixel 9 (ocean), 6 (coastline) and 3 (land) for test area V_NAV_C. The red solid line gives the long-term average for each pixel. 26
Figure 11: Long-term temporal averages of the function y (t,i) as defined in Equation (3) for all transects and satellites.. 27
Figure 12: σ_{GEO} as function of the mean fraction of right surface observed in each pixel and as navigation uncertainty derived from a simple numerical experiment over an idealized coastline. 29
Figure 13: Similar to Figure 12 but for standard deviations from actual MSA observations for all test areas. The colours indicate the different Meteosat satellites. 29
Figure 14: DHR_{30} time series for four desert sites. The colours represent the different MVIRIs on the 0DEG disk from MVIRI-2 (violet) to MVIRI-7 (orange). 31
Figure 15: Location of the 18 AERONET sites used in this study. 33
Figure 16: Comparison of AERONET and MSA aerosol optical depth (AOD). Left: 0DEG coverage, right: IODC_57 and IODC_63. 34
Figure 17: Average of DHR_{30} estimates for the period 2003 to 2006 for cases where dust AOD is higher, (top) resp. lower (middle) than its climatology by at least half a standard deviation;.. 35
Figure 18: Average of BHR_{ISO} estimates for the period 2003 to 2006 for cases where dust AOD is higher, (top) resp. lower (middle) than its climatology by at least half a standard deviation;. 37
Figure 19: Relative deviation of DHR_{30} (left panel) and BHR_{ISO} (right panel) from their long-term averages as function of the AOD for the AERONET station Solar Village. 38
Figure 20: Viewing angle for the MVIRI-7 (0DEG, left) and MVIRI-5 (IODC_57, right) overlapping region in Northern Africa and the Middle East. 39
Figure 21: DHR_{30} and BHR_{ISO} time series for a test site in the Omani desert. Large systematic differences are observed for 0DEG (coloured dots) and IODC (grey dots) observations. 39
Figure 22: Differences between collocated 0DEG (MVIRI-7) and IODC_57 (MVIRI-5) estimates of DHR_{30} over "barren" pixels within the overlapping region (see Figure 20) for the 1-10 Jan. 2006 compositing period, grouped into viewing angle difference intervals. 40
Figure 23: Average (circles) and standard deviation (vertical bars) of the difference between 0DEG (MVIRI-7) and IODC_57 (MVIRI-5) retrievals of DHR_{30} (upper panel) as well as BHR_{ISO} (lower panel) for different land cover types as function of the viewing angle difference. 41
Figure 24: BHR_{ISO} differences as function of satellite viewing angle difference. The left panel shows the five desert sites (rows 1 to 5 in Table 8). 43
Figure 25. Upper panel: MSA DHR_{30} for the 1-10 Jan 2006 compositing period (left); average of daily values of SEVIRI black sky albedo obtained for the same period (central panel) and the difference [MVIRI-7– SEVIRI] (right). 45
Figure 26: Scatterplots of MSA DHR_{30} (x-axis) vs. SEVIRI black-sky albedo (y-axis) for pixels classified as "Barren" for the 0DEG coverage for the 1-10 Jan. 2006 compositing period.. 46
Figure 27: Scatter plots of MSA BHR_{ISO} versus SEVIRI white-sky albedo (y-axis) for pixels classified as "barren" for the 0DEG coverage for the 1-10 Jan. 2006 compositing period. 46

Figure 28 Scatterplots of MSA DHR_{30} (x-axis) vs. SEVIRI black-sky albedo (y-axis) for pixels classified as "evergreen broadleaf forest" for the 0DEG coverage for 1-10 Jan. 2006 compositing period.47
Figure 29: Scatterplots of MSA vs. MODIS Collection 5 (top panel) and MISR (bottom panel) surface albedo products. 48
Figure 30: Distribution of MSA estimated retrieval uncertainty for "evergreen broadleaf forest" pixels, for the 4 compositing periods:. 49
Figure 31: As shown in Figure 27 and Figure 28, but with retrieval errors additionally fulfilling this condition: retrieval error is less than mean retrieval error + 0.5* standard deviation for surface types "barren" (upper four left panels) and "evergreen broadleaf forest" (lower three panels). 50
Figure 32: Scatter plot for 19 FLUXNET sites within the MSA geographical coverage. 51
Figure 33: Comparison of FLUXNET ground truth data ("Tower") against surface albedo products from GlobAlbedo, MODIS ("MCD43C3"), MISR, MSA on MVIRI_5 (IODC) and MVIRI_7 (0DEG) 53
Figure 34: Box-whiskers plots comparing satellite-derived vs. ground-based measurements of the surface albedo at two FLUXNET sites. 54
Figure 35: Location of the validation sites with surface albedo observations predating the MODIS era.55
Figure 36: Comparison of MSA versus *in situ* albedo observations. The box-and-whisker diagrams represent the spatial variability of the MSA observations.. 57
Figure 37: GCOS Climate Monitoring Principles (GCMPs) ensure effective climate monitoring 66
Figure 38: Long-term time series of BHR_{ISO} and DHR_{30} for the Murzuq Desert site. The lower three plots show the position of the target site on the respective 0-degree and IODC disks. 67
Figure 39: Long-term time series of BHR_{ISO} and DHR_{30} for the Libyan Desert site 68
Figure 40: Long-term time series of BHR_{ISO} and DHR_{30} for the Egypt One site. 69
Figure 41: Long-term time series of BHRISO and DHR30 for the site Omani Desert site. 70
Figure 42: Long-term time series of BHRISO and DHR30 for the Toravere, Estonia site. 71
Figure 43: Long-term time series of BHRISO and DHR30 for the Moldova site. 72
Figure 44: Long-term time series of BHRISO and DHR30 for the Mongu, Zambia site.. 73
Figure 45: Long-term time series of BHRISO and DHR30 for the Skukuza, South Africa site. 74
Figure 46: Long-term time series of BHRISO and DHR30 for the Solar Village, Saudi Arabia site.. 75
Figure 47: Location and orientation of the MVIRI pixels around the Toravere (Estonia) reference site at 58.254 N/ 26.462 E. The different grey-shaded areas represent the different MVIRI pixels. 77

Table of Tables

Table 1: List of requirements for validation testing applicable to the MSA product. 8
Table 2: Terminology used in this report. 9
Table 3: Overview of MVIRI observations in standard operation mode. The coverage acronyms refer to Indian Ocean Data Coverage (IODC) and [Extended] Atlantic data coverage ([X]ADC). 11
Table 4: Discretisation values used for MSA forward modelling. 15
Table 5: Selected MVIRI characteristics with relevance to MSA retrieval as compared to other space-borne instruments. 20
Table 6: Vertical navigation uncertainty in units of MVIRI VIS pixels. The horizontal navigation uncertainty could not be assessed due to residual cloud contamination. 30
Table 7: Regression slopes of the datasets shown in Figure 38 to Figure 41. IODC data are restricted to the 63° coverage (MVIRI-5) to avoid potential effects caused by the different observation angles of IODC_63 and IODC_57. Regression slopes exceeding ±0.01/decade in bold. 32
Table 8: Specific sites used to study angular effects on the MSA. Also listed are the corresponding satellite zenith angles for the 0DEG, IODC_57 and IODC_63 areas. 42
Table 10: Validation summary file format. Time information refers to the first day of each 10-day MSA period. 55
Table 11: This is essentially the same table as Table 1. The last column on the right has been added to indicate if theMSA product matches a particular requirement, either Y or N or Not applicable.**Error! Bookmark**
Table 12: Selection of reference surface targets used for the MSA quality assessment purposes. Only targets explicitly mentioned in this report are listed. 65
Table 13: Image dimensions of the different MSG coverage areas as well as the position of the lower left corner on the full MVIRI disk. 76

1 INTRODUCTION

1.1 Purpose and Scope

This document is a validation report for the Meteosat Surface Albedo product. This report summarizes the findings of EUMETSAT's AlbedoVal project (Fell et al., 2012). Figures, captions, text, and conclusions are used directly from Fell et al. and are only slightly reformatted to fit to EUMETSAT documents guidelines [Fell et al., 2012]. The MSA derivation has been developed jointly at EUMETSAT and the Joint Research Centre (JRC) [Pinty et al., 2000-A; Govaerts and Lattanzio, 2007]. The MSA product is the surface albedo retrieval over terrestrial surfaces from the visible channel of the MVIRI instrument onboard Meteosat First Generation (MFG) satellites. Details of the derivation of this product can be found in [RD2].

In this report, MSA data has been compared to surface targets in desert regions to investigate temporal stability. Also, MSA data has been compared to a few ground-based observations (FLUXNET sites) that also include other satellite estimates. Finally, MSA data has been compared to SEVIRI surface albedo estimates from the Land Surface Analysis Satellite Application Facility that contain four months of overlapping data.

This product provides high value to climate studies because of its high temporal stability. This validation also revealed few weaknesses: cloud screening, anisotropy effects in surface albedo, and performance under snow conditions, among other things.

1.2 Document Structure

Section	*Contents*
Section 1	This introduction
Section 2	A brief technical explanation of Meteosat surface albedo product
Section 3	Data used for the validation, including the availability
Section 4	Evaluation of the MSA dataset
Section 5	Summary and conclusions
Section 6	Annex

1.3 Applicable Documents

Number	*Document Name*	*EUMETSAT Reference Number*
AD1	Climate Monitoring Implementation Plan	EUM/C/77/12/DOC/41 REV1

1.4 Reference Documents

Number	*Document Name*	*EUMETSAT Reference Number*
RD1	Meteosat Surface Albedo Retrieval Algorithm Theoretical Basis Document	EUM/OPS/SPE/12/3367

1.5 User Requirements

Table 1 presents a selected list of important requirements for satellite-based climate monitoring systems in general, and surface albedo in particular. These requirements are defined by the Global Climate Observing System (GCOS) and the World Meteorological Organization (WM) on satellite based climate monitoring systems.

ID	*Requirement*	*Source*
GCMP-SAT_01	Consistent sampling within diurnal cycle	GCOS-154
GCMP-SAT_02	Overlap period for old and new satellite systems	GCOS-154
GCMP-SAT_03	Continuity of satellite measurements	GCOS-154
GCMP-SAT_04	Rigorous pre-launch instrument calibration and characterization	GCOS-154
GCMP-SAT_05	On-board calibration adequate for climate system observations	GCOS-154
GCMP-SAT_06	Sustained operational production of priority climate products	GCOS-154
GCMP-SAT_07	Data systems to facilitate user access	GCOS-154
GCMP-SAT_08	Use of functioning baseline instrument meeting calibration and stability requirements	GCOS-154
GCMP-SAT_09	Complementary in situ baseline observations	GCOS-154
GCMP-SAT_10	Identification of random errors and time dependent biases	GCOS-154
GCOS-HRES	Horizontal resolution (1 km)	GCOS-154
GCOS-TRES	Temporal resolution (1-7 days)	GCOS-154
GCOS-ACCU	Accuracy (MAX (5%, 0.0025))	GCOS-154
GCOS-STAB	Stability (MAX (1%, 0.0001))	GCOS-154
WMO_TH_UCRT	Threshold: Uncertainty (10%)	WMO_ORDB
WMO_TH_HRES	Threshold: Horizontal resolution (10 km)	WMO_ORDB
WMO_TH_OBCY	Threshold: Observing cycle (30 d)	WMO_ORDB
WMO_TH_TIME	Threshold: Timeliness (90 d)	WMO_ORDB

Table 1: List of requirements for validation testing applicable to the MSA product.

1.6 The Evaluation Strategy

The strategy used in evaluation of the MSA data record consisted of the following major activities:

- Analysis of MSA method and characteristics of the actual product;
- Assessment of MSA data record in relation to requirements from the climate community;
- Evaluation of MSA data record practical utility;
- Recommendations for MSA product improvement.

Due to the size of an MSA pixel, a direct validation of the MSA product with ground truth measurements is only possible under very specific conditions. The MSA evaluation was therefore based on the following necessary principles:

- Internal consistency checks (i.e. quality checks entirely based on the MSA dataset, partly obtained under different viewing geometries);
- Comparison to other satellite-derived surface albedo products, considering geostationary as well as polar–orbiting instruments;
- Comparison to *in situ* data gathered in reference areas believed to be homogeneous over at least one MSA pixel.

1.7 Terminology Specific to this Validation

Table 2 provides definitions of terms and concepts used in this validation report.

Term / concept	*Definition*	*Reference*
Accuracy	Closeness of agreement between a quantity value obtained by measurement and the true value of the measurand.	ISO/IEC Guide 99:2007
Best practice	Method or technique that has consistently shown results superior to those achieved with other means, and that is used as a benchmark.	Wikipedia
Bias	Systematic error of indication of a measuring system.	ISO/IEC Guide 99:2007
Calibration	The process of quantitatively defining the system response to known controlled signal inputs.	CEOS WGCV
Consistency	Achieving a level of performance which does not vary greatly in quality over time.	Oxford Dictionaries
Error	Difference of quantity value obtained by measurement and the true value of the measurand.	ISO/IEC Guide 99:2007
Evaluation	Judgement about the amount, number, or value of something; assessment.	Oxford Dictionaries
Plausibility	Quality of seeming reasonable or probable value.	Oxford Dictionaries
Quality indicator	Indicator of performance or quality of the result of a process/activity derived from an uncertainty estimate to allow users to evaluate fitness of purpose. This can be a text descriptor, a flag, or a numeric value.	QA4EO
Stability	Ability of a measuring system to maintain its metrological characteristics constant with time.	ISO/IEC Guide 99:2007
Traceability	Establishment of an unbroken chain of comparisons to stated references each with a stated uncertainty.	NIST
Uncertainty	Dispersion of the quantity values that are being attributed to a measurand, based on the information used.	ISO/IEC Guide 99:2007
Validation	Process of assessing, by independent means, the quality of the data products derived from the system outputs.	CEOS
Verification	Process intended to check that a product, service, or system meets a set of initial design requirements, specifications, and regulations.	Wikipedia

Table 2: Terminology used in this report.

2 METEOSAT SURFACE ALBEDO TECHNICAL DESCRIPTION

2.1 The Meteosat Surface Albedo (MSA) Product

A complete description of the MSA product retrieval will be found in [RD1] and [RD2]. Some important criteria for evaluating the validation are presented in this section.

2.1.1 The Meteosat Visible and Infrared Imager (MVIRI)

Meteosat's primary instrument is the Meteosat Visible and InfraRed Imager (MVIRI), flown on all Meteosat First Generation (MFG) satellites since Meteosat-2 was launched in 1981. MVIRI acquires radiance data from the full earth disc every half hour. MVIRI operates in three spectral bands, chosen in accordance with Meteosat's primary task of mapping the distribution of clouds and water vapour. The MVIRI Visible (VIS) band extends from 0.45 µm to 1.0 µm with a central wavelength at 0.70 µm. Atmospheric gases are fairly transparent to incoming and outgoing (reflected) solar radiation in this spectral range. The VIS band is used for imaging during daylight and provides the input data to the Meteosat Surface Albedo (MSA) product.

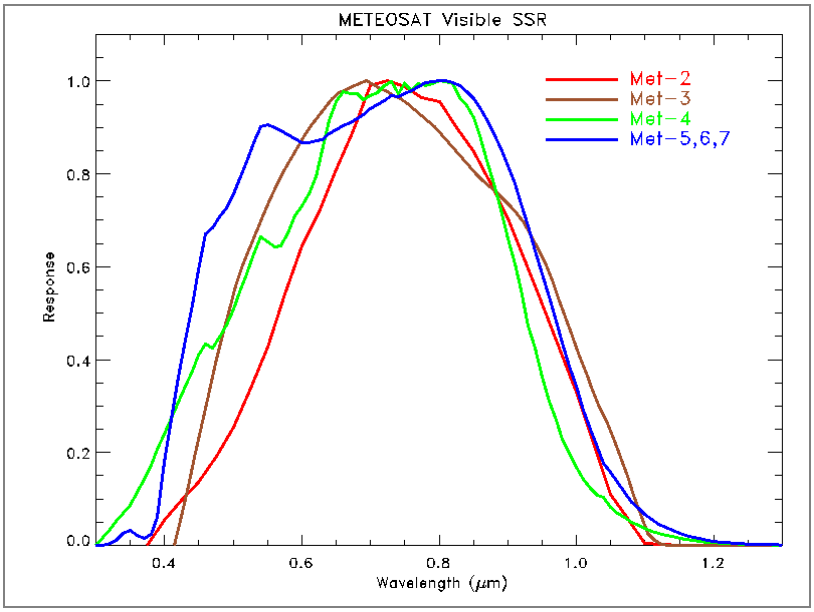


Figure 1: Sensor spectral response of the MVIRI VIS band for all Meteosat First Generation satellites.

2.1.2 Nominal coverage areas and periods

The main mission of the MFG satellites was to provide data for the 0 degree (0DEG) service area that covers most of Europe, Africa, the Middle East, and the Eastern parts of South America. Consequently, all MFG satellites were first positioned in a geostationary orbit with a nominal sub-satellite point above the equator at 0° longitude.

To bridge a gap in the availability of GOES (Geostationary Operational Environmental Satellite, US) data from the western Atlantic Ocean between 1991 and 1995, Meteosat-3 was moved to the west, first to 50° W and later to 75° W early in 1993. These temporary services, called Atlantic Data Coverage (ADC) and Extended-ADC (XADC) respectively, had the primary purpose of supporting the monitoring of severe weather events such as hurricanes.

To increase data availability above the Indian Ocean, Meteosat-5 was moved in 1997 to a sub-satellite point above the Indian Ocean at 63° E. MVIRI data acquired at this position are available from mid-1998 well into 2007. Meteosat-7 has been positioned at 57.5° E from where it has acquired data since November 2006 to the present. . Meteosat-6 was also positioned above the Indian Ocean at 67.5° between January 2007 and April 2011 as a back-up satellite, but was taken out of orbit in April 2011.Table 3 provides an overview of the resulting coverage of MVIRI observations in standard operation mode.

Coverage	*SSP*	*Satellite*	*Start Date*	*End Date*
0 Degrees	0°E	MET2	16/08/1981	11/08/1988
		MET3	11/08/1988	25/01/1991
		MET4	19/06/1989	04/02/1994
		MET5	02/05/1991	13/02/1997
		MET6	21/10/1996	20/01/2000
		MET7	03/06/1998	19/07/2006
IODC_63	63°E	MET5	01/07/1998	16/04/2007
IODC_57	57°E	MET7	01/11/2006	Ongoing
ADC	50°W	MET3	01/08/1991	27/01/1993
XADC	75°W	MET3	21/02/1993	31/05/1995

Table 3: Overview of MVIRI observations in standard operation mode. The coverage acronyms refer to Indian Ocean Data Coverage (IODC) and [Extended] Atlantic data coverage ([X]ADC). The corresponding sub-satellite points (SSP) are also indicated.

Table 3 shows the spatial coverage corresponding to the five different Meteosat orbits. These plots indicate the maximum possible coverage area. Large zenith angles, cloud contamination, and other adverse effects lead to a reduced practical coverage. See section 4.1.

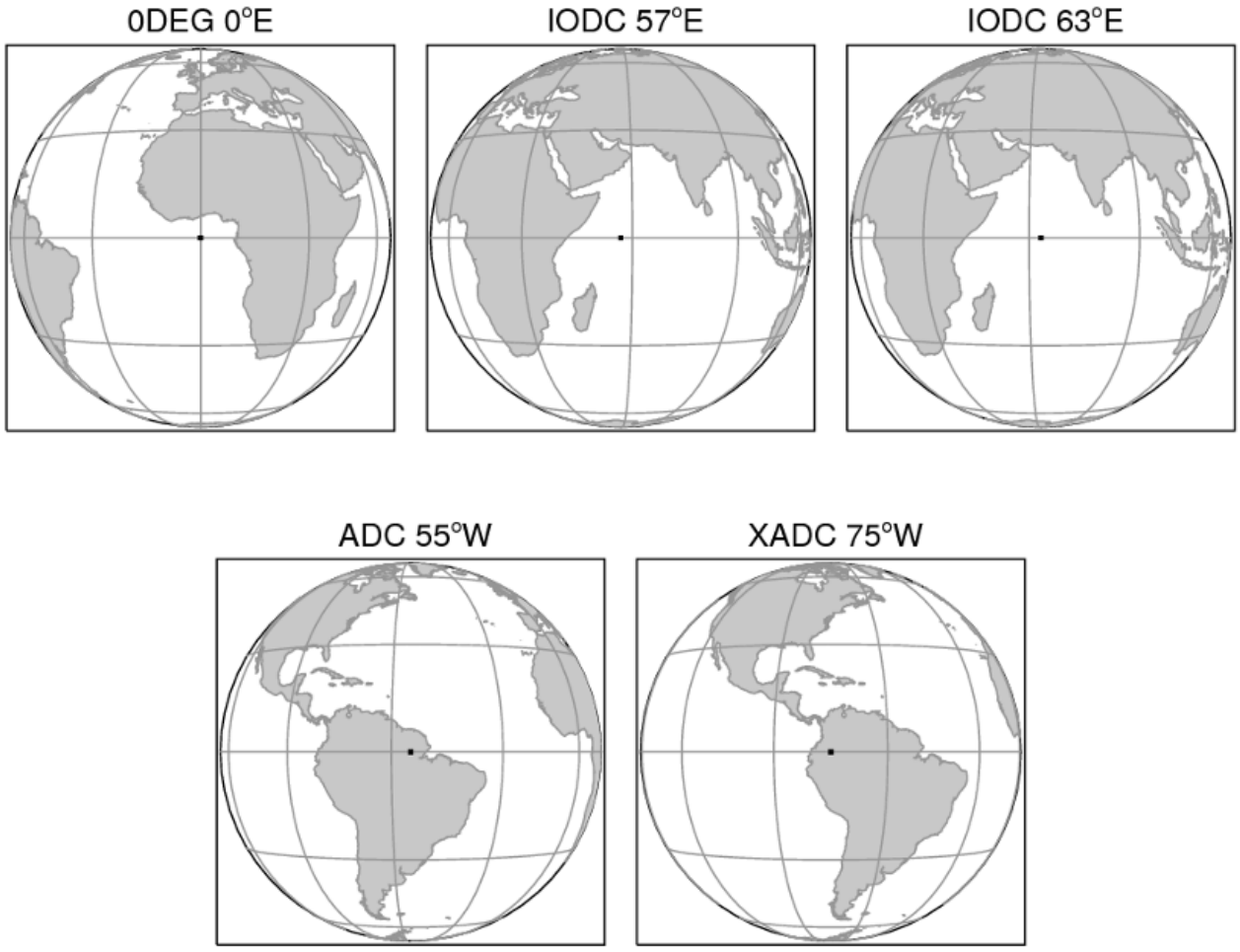


Figure 2: The five different coverage areas in native MSA projection. The respective sub-satellite points are shown as a black dot in the centre of each panel.

2.1.3 The MSA Scientific Approach

The Meteosat Surface Albedo (MSA) algorithm has been developed jointly at EUMETSAT and the Joint Research Centre (JRC) based on the method proposed by Pinty et al. [2000-A, 2000-B]. It accumulates MVIRI VIS observations during one day to form a measurement vector for each pixel (see Figure 3). The surface albedo and other parameters are then concomitantly retrieved by inverting a radiative transfer model.

The MSA surface albedo retrieval is based on the following major assumptions:

- Surface and atmospheric scattering properties are assumed constant along the day;
- Aerosol scattering can be approximated by a single continental aerosol type;
- Surface anisotropy can be represented with the simple Bidirectional Reflectance Factor (BRF) model proposed by Rahman et al. [1993] (further on referred to as RPV);
- The reciprocity principle– the assumption that the BRDF is unchanged when incident and observation angles are reversed–is valid over terrestrial surfaces at a spatial resolution of a few kilometres [Lattanzio et al., 2006].

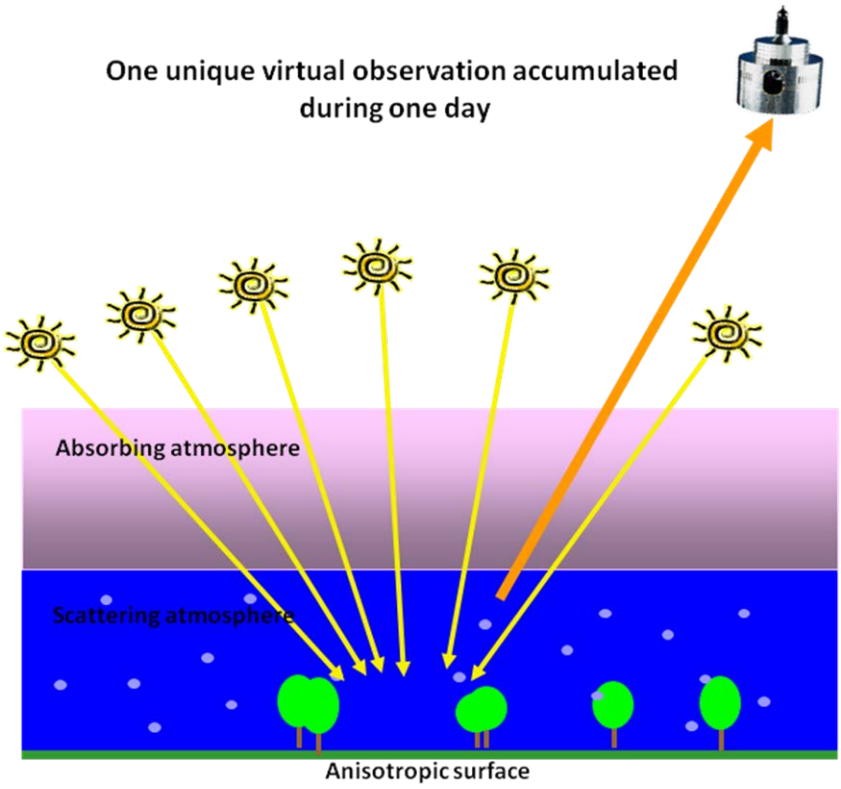


Figure 3: MSA retrieval scheme. Observations accumulated during the day are used as an angular sampling of the surface.

The radiative state of the observed medium, the atmosphere and the underlying surface, is described by a set of six state variables:

τ	equivalent aerosol optical thickness (EAOT) at 550 nm
$\rho 0$	amplitude of surface BRF
Θ	asymmetry of surface BRF
k	bowl shape of surface BRF
U_{H2O}	total column water vapour
U_{O3}	total column ozone

Due to the limited information content of the measurement in only one channel, it is not possible to retrieve all six variables that characterise the radiative state of the observed medium. To reduce the number of free parameters, the total column water vapour is taken from ECMWF re-analyses and the total column ozone from Total Ozone Mapping Spectrometer (TOMS) observations [McPeters, 1996].

The values of the other four state variables (τ, $\rho 0$, Θ, k) are concomitantly retrieved through the inversion of (forward) radiative transfer calculations against the measurement vector, minimising the differences between observations and simulations, normalised by the respective observation error [Govaerts and Lattanzio, 2007]. A probability is assigned to each solution that specifically depends upon the number of degrees of freedom and the value of a cost function. The estimation of the retrieved parameter uncertainty relies on a statistical analysis of the solution ensemble. A 10-day temporal compositing technique is applied to maximise the spatial coverage of cloud free pixels. Finally the retrieved surface state variables ($\rho 0$, Θ, k) are applied to the RPV model to derive the Directional Hemispherical Reflectance (DHR_{30}) for a reference solar zenith angle of 30° together with its respective error as well as BHR_{ISO}.

The blue-sky albedo is not derived within the MSA, but may be estimated in an additional step as a linear combination of DHR_{30} and BHR_{ISO}, using weighting factors representing the estimated ratio between diffuse and direct downwelling atmospheric radiation which itself may be deduced from the aerosol optical depth [Pinty et al., 2005].

2.1.4 MSA implementation overview

The MSA algorithm is implemented in four sequential steps:

1. Data consistency procedure (DCP)
   This module attempts to screen out cloud-affected pixels by identifying measurements that deviate from the course of the diurnal BRF at TOA [Pinty et al., 2000-B];
2. Atmospheric scattering module (ASM)
   This module first corrects for the absorption by atmospheric gases and then inverts a radiative transfer model representing the atmosphere-surface system to provide all possible solutions to a measurement vector;
3. Data interpretation module (DIM)
   This module chooses the most likely solution among all possible solutions retrieved in the previous step;

4. Time-averaging module (TAM)
   Steps 1 to 3 are applied on a daily basis. In this last module, the best solution for the 10-day period is selected.

   Note: The (historic) term "averaging" is somewhat misleading here since averaging is taking place only for AOD and not taking place for DHR_{30} and BHR_{ISO}.

To speed up model inversion, the 6S radiative transfer code [Vermote et al., 1997] has been used to calculate look-up-tables of an ancillary function for every combination of the discrete values shown in Table 4.

Parameters	*Values*
k	0.4, 0.5, 0.6, 0.7, 0.8, 0.9, 1.0
ɵ	-0.30, -0.25, -0.20, -0.15, -0.10, -0.05, 0.00
τ	0.1, 0.2, 0.3, 0.4, 0.6, 0.8, 1.0

Table 4: Discretisation values used for MSA forward modelling.

2.1.5 MSA Implementation Details

Five separate aspects of the MSA implementation are explained in this section: improving data consistency, atmospheric effects, directional-effects, temporal compositing, and broadband conversion.

2.1.5.1 Improving data consistency

Clouds and cloud shadows are screened out in the first processing step (DCP) by analysing the daily cycle of the bi-directional reflectance factor (BRF). Note that in the present version, MSA neither uses the MVIRI IR channels as additional information source for cloud identification nor rely on externally-generated cloud masks.

A threshold value of 0.6 is applied on the TOA BRF measurements to reject obviously cloudy conditions [Pinty et al., 2000-B].

Note: This threshold value will also lead to the rejection of cloud-free pixels of snow-covered surfaces.

To further eliminate pixels affected by undetected clouds, topography shadows, errors in the data geo-rectification process, and/or significant diurnal variations in aerosol load and type, the screened TOA BRF values are additionally checked against a modified version of the RPV model [Engelsen et al. 1996]: An iterative process eliminates the observed BRF value that exhibits the largest absolute deviation with respect to the model prediction (see Figure 4). A pixel is further processed only if it contains at least six valid daily observations. The cloud detection method occasionally fails when the cloud cover remains stable during an entire day.

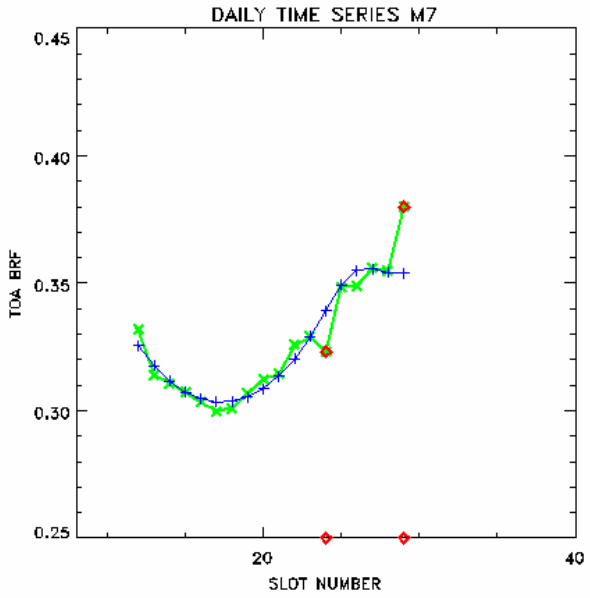


Figure 4: Example of the data consistency procedure (DCP) for MVIRI-7. Green: BRF from MVIRI measurements. Blue: Best-fit. The red squares represent rejected values likely affected by clouds (above fit) or cloud shadows (below fit) (figure by courtesy of EUMETSAT).

The result of the fit between the modelled TOA BRF and the valid observations provides an estimation of the filtering process cost, accounting for an uncertainty σ_{DCP} between data and model.

2.1.5.2 Atmospheric effects

The MSA algorithm decouples atmospheric gaseous absorption from scattering by subdividing the atmosphere into two distinct layers: the lower layer accounts for the scattering processes and the upper layer accounts for gaseous absorption.

The atmospheric effects have been calculated for a US-62 standard atmosphere like the example here: http://modelweb.gsfc.nasa.gov/atmos/us_standard.html, additionally implementing a continental aerosol model, which includes a mixture of dust-like, water-soluble, and soot components (see Vermote et al. [1997]). Two gaseous absorbers are taken into account: the total column water vapour is taken from ECMWF re-analyses and the total column ozone from the Total Ozone Mapping Spectrometer (TOMS) observations [McPeters, 1996].

2.1.5.3 Directional-effects

As previously mentioned, the MSA retrieval is based on these assumptions:

- surface anisotropy can be represented with the simple BRF model proposed by Rahman et al. [1993], and
- the reciprocity principle is valid over terrestrial surfaces at a spatial resolution of a few kilometres [Lattanzio et al., 2006].

While the former assumption is drawn from the need to apply a simple BRDF model to account for the limited information content of MVIRI observations, the latter assumptions accounts for the fact that MVIRI, being on a geostationary orbit, always observes a specific pixel under the same viewing

angle, meaning that the only variation in the observation geometry comes from the different solar illumination geometries during the course of a day. The RPV model (see also Pinty et al. [2000-A,-B]), describes the angular distribution of the surface BRF by this equation:

$$\rho_s\left(z_0,\Omega_s,\Omega_v;\rho 0,\Theta,k\right)=\rho_0\,\rho'_s\left(z_0,\Omega_s,\Omega_v;\Theta,k\right) \qquad \textit{Equation 1}$$

where:

Ω_s and Ω_v	are the illumination and viewing direction
z_0	denotes the bottom of the atmosphere

The reflective properties of the surface are described by the parameters ρ_0, Θ and k where ρ_0 specifies the amplitude, Θ the asymmetry and k the bowl shape of the surface BRF in the RPV model.

While the reciprocity principle is generally assumed valid, the rather simple BRF model will necessarily lead to an error when attempting to retrieve the albedo from MVIRI measurements. For example, Rahman et al. [1993] observed relative root mean square errors (RMSE) above 20% for optimally-fitted asymmetry parameters when comparing modelled to measured bidirectional reflectances, like for soybean fields, coniferous forest or pasture land.

2.1.5.4 Temporal compositing

The objective of the temporal compositing is to maximise the number of clear-sky processed pixels during a 10-day period. This compositing relies on the selection of the single most representative solution over the accumulation period. The most obvious way is to select the solution with the best fit accounting for the actual number of degrees of freedom. Hence, the most representative solution within a 10-day period is the one with the highest probability.

As clouds tend to increase the signal received at satellite level, selecting the solution with the smallest ρ_0 will tend to minimise the impact of undetected clouds. Thus, if two or more solutions have the same probability, the one with the lowest ρ_0 is selected.

2.1.5.5 Broadband conversion

A third order polynomial is applied [Govaerts et al., 2006] to transform the directional hemispherical reflectance DHR_{VIS} which represents the spectral range 0.45 µm – 1.0 µm derived from MVIRI VIS measurements, into the shortwave broadband albedo DHR_{BB} (0.3 µm – 3.0 µm)

$$DHR_{BB}=a+b\times DHR_{VIS}+c\times\left(DHR_{VIS}\right)^2+d\times\left(DHR_{VIS}\right)^3 \qquad \textit{Equation 2}$$

The coefficients a to d as well as a measure of uncertainty are specified in the product user manual for the MVIRI-2 to MVIRI-7. Use of the original coefficients led to systematic deviations and temporal inconsistencies in the MSA dataset. Recently, Loew and Govaerts [2010] empirically derived correction factors leading to a significantly improved product consistency. Those are reported in the product user manual as well and should be used to obtain best results.

3 DATA USED FOR THE VALIDATION

Three different types of reference data have been used within the course of this validation exercise to assess the quality of the MSA dataset:

- *In situ* measurements of the surface albedo;
- Satellite-derived values of the surface albedo;
- Ancillary information on land cover and atmospheric aerosol.

3.1 Surface Albedo Using *in situ* Data

3.1.1 Availability

During the initial stages of the validation, the availability of surface albedo *in situ* data was analysed. Considering these facts

- the importance of the surface albedo as essential climate variable;
- the availability of relatively inexpensive and robust standard instrumentation, and
- the fact that surface albedo measurements have been routinely done for several decades,

we expected to find relevant information readily available on the internet. However, this is not the case, especially for the pre-EOS era. On the other hand, a lot of information on surface albedo measurements can be found in the scientific and "grey" literature. However, this information is scattered and not readily available in digital data formats. The published results also represent only a limited fraction of all measurements made. See section 3.1.3.

Surface reference data optimally suited for validating satellite-based surface albedo retrievals should fulfil the following requirements:

- Sites should be located in areas with homogeneous land cover;
- Measurement should be taken at sufficient height above reference surface to integrate over small-scale heterogeneity;
- Sites should include a sufficiently broad range of different land cover types [loc. cit.].

Originally, the Base Surface Radiation Network, at http://www.bsrn.awi.de/en/home/ fromBSRN [Ohmura et al., 1998] was seen as a usable reference dataset given its frequent use for climate studies [Wild et al., 2001]. However, only a few of the roughly 20 BSRN stations located in the MVIRI field-of-view do actually provide surface albedo measurements and are often located in rather heterogeneous landscapes.

Figure 5 shows an example for the BSRN site in Toravere (Estonia) clearly demonstrating that this site is not suitable for validating satellite-derived surface albedo for pixels at MODIS or even MVIRI size due to highly heterogeneous land cover and the resulting misrepresentation of the surface albedo derived from ground-based instruments.

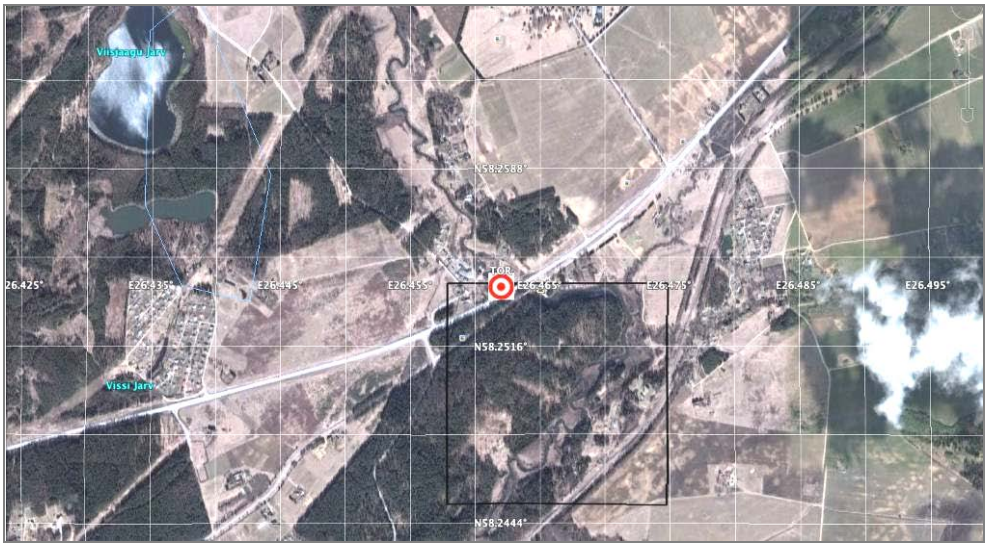


Figure 5. Aerial image of the area around the BSRN site (red-white symbol) at Toravere, Estonia The typical extension of a MODIS pixel is shown by the black square. An MSA pixel would roughly cover the whole area shown [Image source: Google Earth].

An alternative set of tower albedo measurements have recently become available as a result of a significant effort by the JRC on behalf of the FLUXNET consortium. See the web page http://daac.ornl.gov/FLUXNET/fluxnet.shtml for details on this consortium and their data.

Cescatti et al. [2012] showed the application of some 53 sites meeting certain surface homogeneity requirements to an assessment of MODIS-derived albedo data for the year 2005 (Figure 6). However, FLUXNET measurements are also not optimally suited for MSA validation purposes as they are concentrated in Europe and the US and are limited to vegetated surface types classified into plant functional types (PFTs).

Surface albedo ground truth data considered for this validation study are taken from FLUXNET (19 sites), Safari 2000 (2 sites), and the Baseline Surface Radiation Network (BSRN, 2 sites), as well as from a selection of data originating from individual measurement campaigns in Sudan in 1988 and 1989 (see section 0 for more details). The comparison of these *in situ* data with the corresponding MSA values is shown in section 4.8.

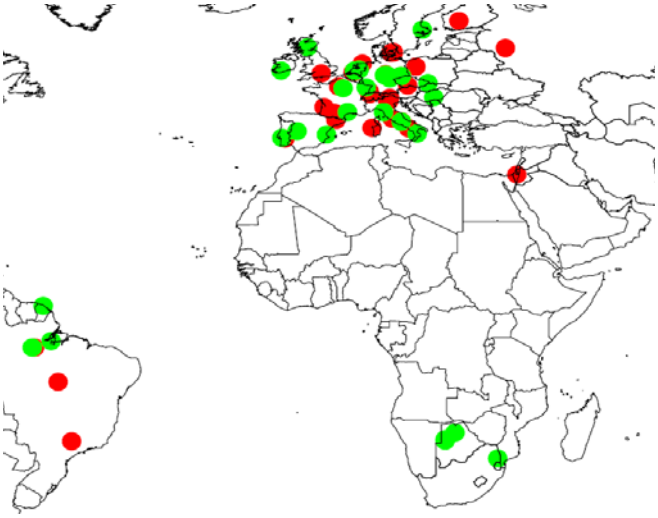


Figure 6. FLUXNET sites within the MVIRI 0DEG field-of-view taking albedo measurements. Green dots represent sites with sufficient plant cover homogeneity at a 1 km² scale. Source: Cescatti et al. [2012].

3.1.2 Scaling Up to MSA Pixel Size

A number of approaches exist to relate ground-based surface albedo measurements (representing areas of typically 100 to 1,000 m²) to the space-based albedo retrievals, which represent about 250,000 m² for MODIS at 500 m resolution or 6,250,000 m² for MVIRI-VIS.

The direct approach is to use only the surface reference data that represents the average land cover of the full satellite pixel for validation. To quantify the homogeneity of the land cover within the pixel, higher resolution imagery can be applied, either for visual inspection or for deriving statistical homogeneity metrics. Only pixels above a certain homogeneity threshold would then be used for further analysis. Obviously, the number of suitable reference sites decreases with increasing pixel size, especially when considering the geo-location uncertainty–1-2 pixels for MVIRI). This is the approach pursued in this validation report. See section 3.4.2 for more details.

An indirect approach assigns standard BRDFs to the individual classes of a high-resolution land cover dataset like CORINE6, see http://sia.eionet.europa.eu/CLC2006/) and to then integrate this small-scale information to the required pixel size. For details, see Fang et al. [2004]. This approach could not be pursued.

3.2 Satellite-derived Surface Albedo Values

Due to the lack of ground-truth data suitable for a direct validation of satellite-derived surface albedo products, the method most applied to assess the quality of such products consists of *"internal"* and *"external"* product plausibility and consistency checks. The internal plausibility and consistency of a satellite-derived product can be assessed by looking at time series over stable surface targets, or by looking at a reference surface under different observation geometries but otherwise similar conditions. Such internal quality checks play an important role in the assessment of the MSA and are described in more detail in sections 4.1, 0, 4.5, and 4.7.

Quality aspect	*MSA characteristics*	*Better suited (examples)*
Temporal resolution	30 minutes	SEVIRI (15 minutes)
Spatial resolution	2.5 km at nadir	MODIS (0.5 km) MISR (0.375 km) MERIS (0.3 km)
Spectral resolution	1 VIS/NIR channel	SEVIRI (3 VIS/NIR channels) MISR (4 VIS/NIR channels) MODIS (5 VIS/NIR channels at 0.5 km) MERIS (15 VIS/NIR channels)
Surface anisotropy	Change in observation geometry only through changing solar position	MODIS, MERIS (single-angle polar orbiting) MISR, POLDER (multi-angle polar orbiting)

Table 5: Selected MVIRI characteristics with relevance to MSA retrieval as compared to other space-borne instruments

In the context of this validation, external plausibility relates to the comparison of the MSA data with equivalent values from other space-borne sensors. Due to more appropriate measurement approaches, certain space-borne instruments should, in principle, provide more accurate surface albedo values than does MSA product.

For example, an instrument with higher spectral resolution in the VIS/NIR should provide a higher accuracy of the broadband albedo than an instrument that just measures in one spectral channel not fully covering the relevant (0.3 µm – 3.0 µm) portion of the spectrum. Another example would be polar-orbiting instruments with multi-angular observation capabilities being better suited to correct for surface anisotropy effects than single-angle or geostationary instruments.

See section 4.6 for more information on the external MSA quality checks performed during this validation.

3.3 Other relevant datasets

The following auxiliary datasets have been used to assess the impact of the atmospheric aerosol load on the quality of the MSA retrieval:

- Aerosol optical depth (AOD) at 550 nm provided by MACC-II (Monitoring Atmospheric Composition and Climate – II) re-analysis project. This dataset provides daily global AOD values and is available for the period 2003 to 2010 with a spatial resolution of 125 km [Benedetti et al., 2011]; See http://www.gmes-atmosphere.eu/data/
- AOD at 550 nm derived from Aerosol RObotic NETwork (AERONET) data. AERONET is a federation of ground-based networks that provide a long-term public domain database of aerosol optical, microphysical and radiative properties.
- The International Geosphere-Biosphere Programme (IGBP) ecosystem categories [Belward, 1996] have been used as a reference land-cover classification.

As the existence of residual cloud contamination in the MSA product is to some degree detectable by statistical means (see section 4.7), external cloud products were not used in the context of this study. However, cloud masks provided by other sensors like MODIS may become important to test the quality of an improved MSA product. In this context, re-analysis datasets such as ERA-Int [Dee et al., 2011] may be useful to identify geographical regions and seasons that are more likely to be affected by cloud contamination.

3.4 Reference sites

3.4.1 Site selection

To compare MSA values with other satellite-derived products, a number of suitable reference sites targeting specific potential quality issues have been identified:

- Navigational accuracy: coastlines with meridional and zonal orientation;
- Cloud contamination: dark surfaces;
- Temporal stability: arid surfaces assumed stable over time;
- Atmospheric impact: AERONET sites located in both 0DEG and IODC areas;
- Angular effects: reference surfaces located in both 0DEG and IODC areas;
- Sat-sat comparisons: "highly homogeneous" land cover over 5 × 5 MSA pixels, see section 3.4.2 for a definition of the applied homogeneity measures);
- Satellite versus *in situ* comparisons: "*highly homogeneous*" land cover over 5 × 5 MSA pixels with concomitant availability of *in situ* data).

The identification of large homogeneous reference sites was done partly by visual interpretation of Google Earth satellite images, and partly by using sites suggested in the context other activities, like BELMANIP. See http://calvalportal.ceos.org/cvp/web/olive/site-description.

In total, a list of 87 reference surface targets has been established. This list is in a separate Excel spreadsheet: ALB_Reference_Areas.xls. Of this 87, 50 have been used for this study and 17 have been explicitly mentioned in this report. See Table 12.

3.4.2 Surface characterisation

Surface land cover and homogeneity of all potential surface reference targets have been analysed using USGS' Global Land Cover Characteristics (GLCC) Data Base in Version 2.0 in combination with the IGBP land cover legend. The GLCC dataset has been derived from AVHRR data spanning a 12-month period: 04/1992 and 03/1993. Its spatial resolution is 30 arc seconds, equivalent to a meridional resolution of about 1 km. The reason for choosing GLCC and the IGBP land cover legend is because this data set is globally available, well tested and documented, and frequently used in climatic applications. The following surface characterisation parameters have been derived for each surface:

Land cover type at centre of the reference surface and position of *in situ* measurement;		
Fraction of dominant LC type within a 2.5' × 2.5' area	25 GLCC pixels	~5 × 5 km
Fraction of dominant LC type within 12.5' × 12.5'	625 GLCC pixels	~25 × 25 km

The degree of homogeneity of a reference surface target has been assigned according to the following rules:

Average the land cover type at the centre pixel is equivalent to the dominant land cover type within a 2.5' × 2.5' area around the centre covering more than 75% of the area

High the land cover type at the centre pixel is additionally equivalent to the dominant land cover type within a 12.5' × 12.5' area around the centre covering more than 75% of the area

Low (or heterogeneous) Any other combination of these limitations.

Of the 87 surface reference targets identified for this study, 34 have been classified as being of low homogenity, 20 as being of average homogenity, and 33 as being of high homogeneity.
While it is not always possible to limit the assessment to homogeneous or very homogeneous surface targets, the homogeneity characterisation of the surface targets may help to explain observed discrepancies.

4 EVALUATION OF THE MSA DATASET

4.1 Product availability

Since the start of standard operational mode of Meteosat-3 in August 1988 until July 2006, MVIRI data have been continuously available for the 0DEG coverage. In July 2006, Meteosat-7 was replaced by MSG-2. Availability for the 0DEG coverage dates further back to August 1981, with only a few gaps in coverage. MVIRI data covering the IODC for the 63°E SSP are available for any time between July 1998 and April 2007 and since November 2006 for the 57°E SSP. Figure 7 shows the temporal coverage of MVIRI-2 to MVIRI-7 for the 0DEG and IODC areas.

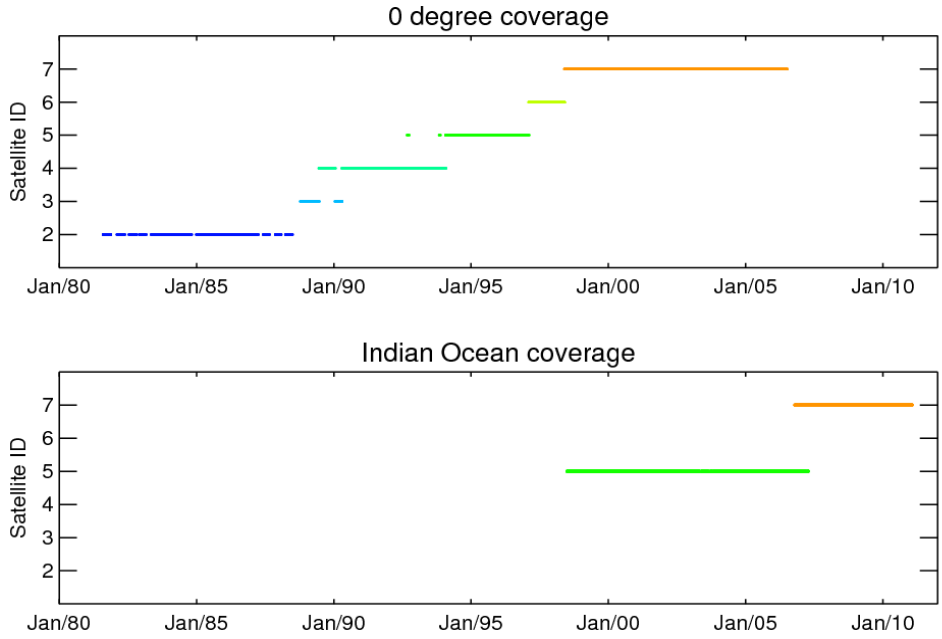


Figure 7: MSA temporal coverage for 0DEG and IODC. Note that Meteosat-5 was positioned at 57°E over the IODC whereas Meteosat-7 is located at 63°E.

Depending on geographical position and season, the number of valid MSA data points will be reduced due to external factors such as cloud cover and low solar elevation. . Figure 8 shows the practical MSA availability for the 0DEG, IODC_57 and IODC_63 areas. The availability is given in per cent for each grid cell and indicates the number of valid MSA values relative to all available 10-day periods.

While the MSA availability is near 100% for many desert areas, it is significantly reduced for others. For example, availability is on the order of 30% over northern Europe; this is caused by low solar zenith angles in winter and frequent cloud cover throughout the year. Low availability is also observed over the Congo basin due to frequent cloud cover.

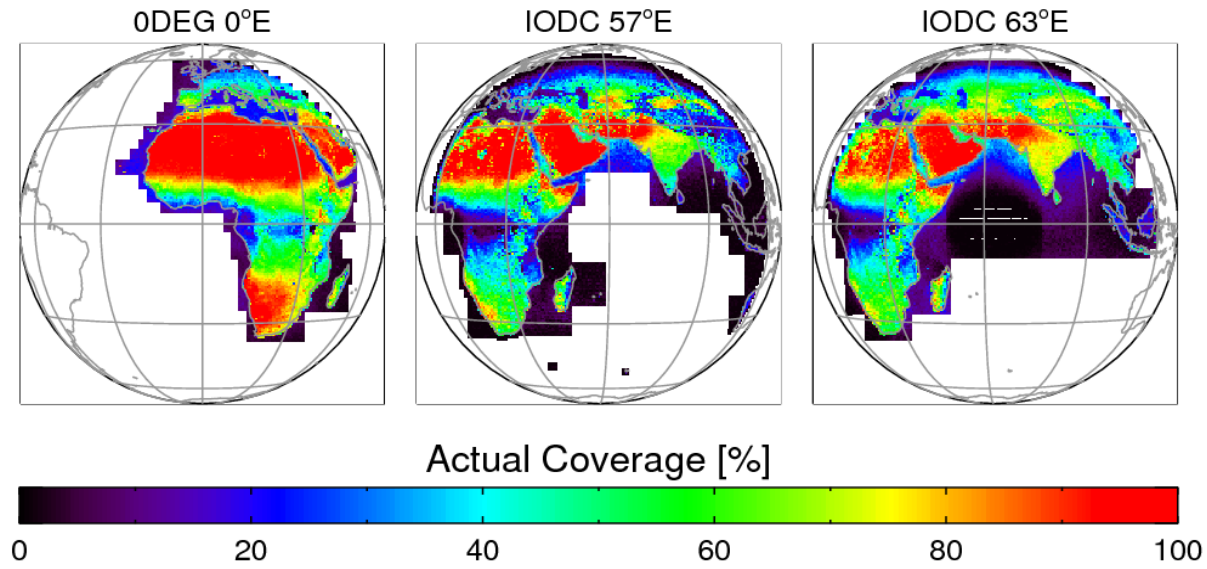


Figure 8: Practical MSA availability for 0DEG, IODC_57 and IODC_63. White areas do not supply any data. Black areas can provide MSA data occasionally.

4.2 Pixel navigation

4.2.1 Results overview

Little information is found in the available technical documentation about MVIRI's spatial resolution and sampling accuracy. The MFG Handbook [EUMETSAT, 2011-A] does not discuss resolution, only sampling. A GSICS MVIRI-IASI inter-calibration study [EUMETSAT, 2011-B] reports a navigation uncertainty of about 1.5 pixels. This is consistent with the findings of this study, which can be summarised as follows. Sections 4.2.2 to 4.2.5 have more detailed information.:

- With the exception of MVIRI-3, the navigation accuracy of the MVIRIs with respect to each other is approximately one pixel vertically and about 1.5 pixels horizontally;
- MVIRI-3 appears to be consistently shifted to the top by about 1.5 to 2 lines;
- The earlier MVIRIs show additional long-term navigational drifts and oscillations typically within the 1 pixel range;
- The scene-to-scene vertical navigation uncertainty is estimated at about 1.5 pixels. The horizontal navigation uncertainty could not be assessed with sufficient accuracy but is probably confined to a similar range.

This analysis has been done in MSA image co-ordinates; we therefore use the terms *horizontal* and *vertical* as well as *top*, *bottom*, *left* and *right* to describe positional uncertainties.

A more detailed analysis of navigation uncertainties would have to resort to Level-0 or Level-1 data. This would be especially important if reprocessing of MVIRI raw data and derived products is planned. Studying navigation accuracy was hampered by lacking information on MVIRI pixel resolution as well as lacking technical details of the geo-location routines. While EUMETSAT User Help Desk proved very responsive and helpful when trying to obtain relevant information, documentation on some of the older geo-referencing routines used in the MVIRI processing were just not available.

4.2.2 Scene selection

Six coastline scenes consisting of 11 × 11 MSA pixels were identified in order to study the MVIRI pixel navigation (see Table 12). Reference targets and MVIRI "transects" are shown in Figure 9.

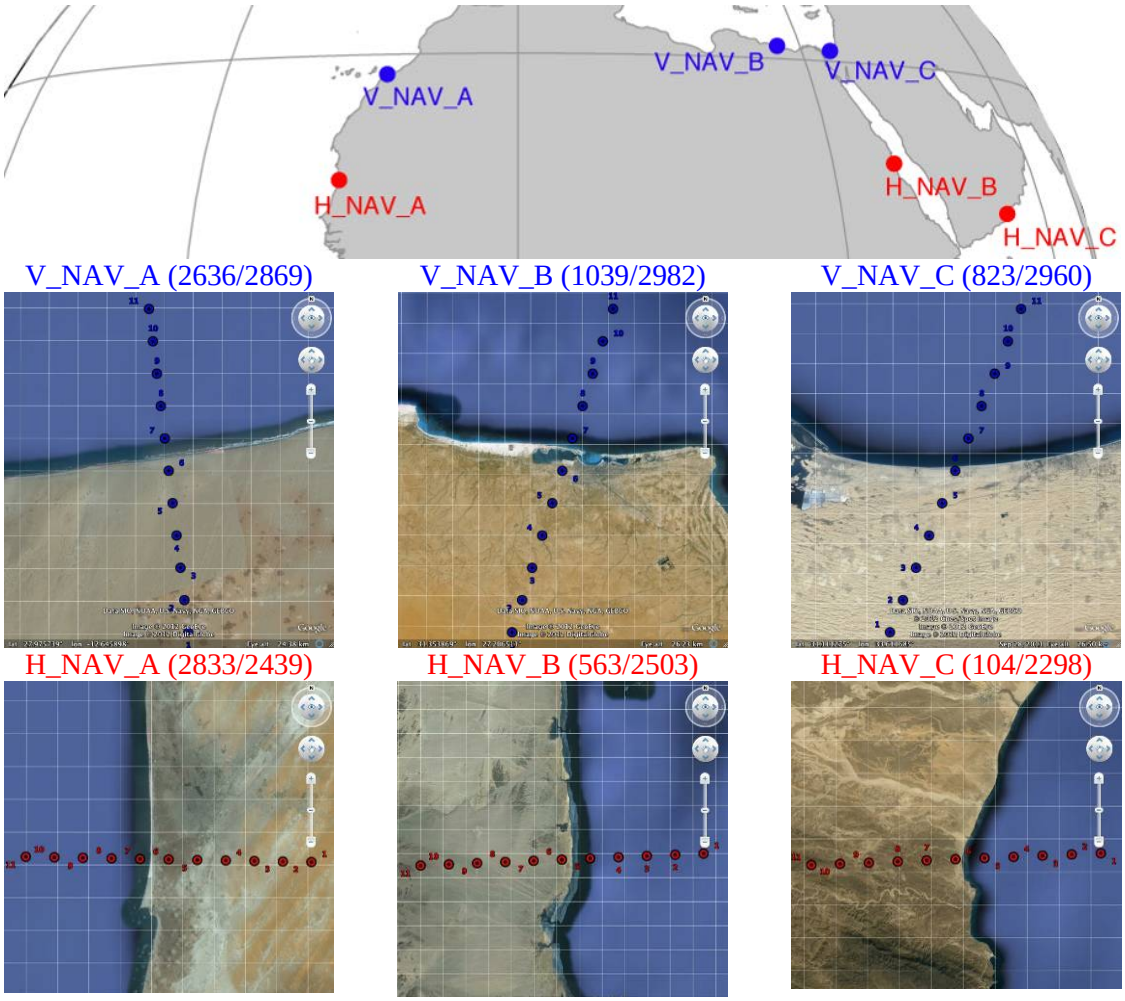


Figure 9: Reference coastlines used for studying MSA geo-location stability and accuracy. The MSA column/row position of the corresponding centre pixels is given in brackets in the header of each image. The blue resp. red dots mark the nominal centre positions of 11 adjacent MSA pixels within a column resp. row crossing the coastline.

The top panel in Figure 9 shows the location of the 11 × 11 reference areas on the 0DEG disk. The six images underneath provide a detailed view of each of these areas. This is high resolution imagery from Google Maps, the white grid shown does not represent the MSA grid. The coastlines have been chosen to be approximately parallel in orientation to the rows and columns of the MSA product. In addition, the surface targets are located in desert areas to maximise the contrast between bright land surfaces and the dark ocean.

4.2.3 Evaluation methods

Time series of BHR_{ISO} were generated for each pixel of each transect for each satellite. Figure 10 shows an example of such a time series for three selected pixels out of transect V_NAV_C. One can easily identify the "coastal" pixel by its much larger temporal variability as compared to "pure" land and ocean pixels.

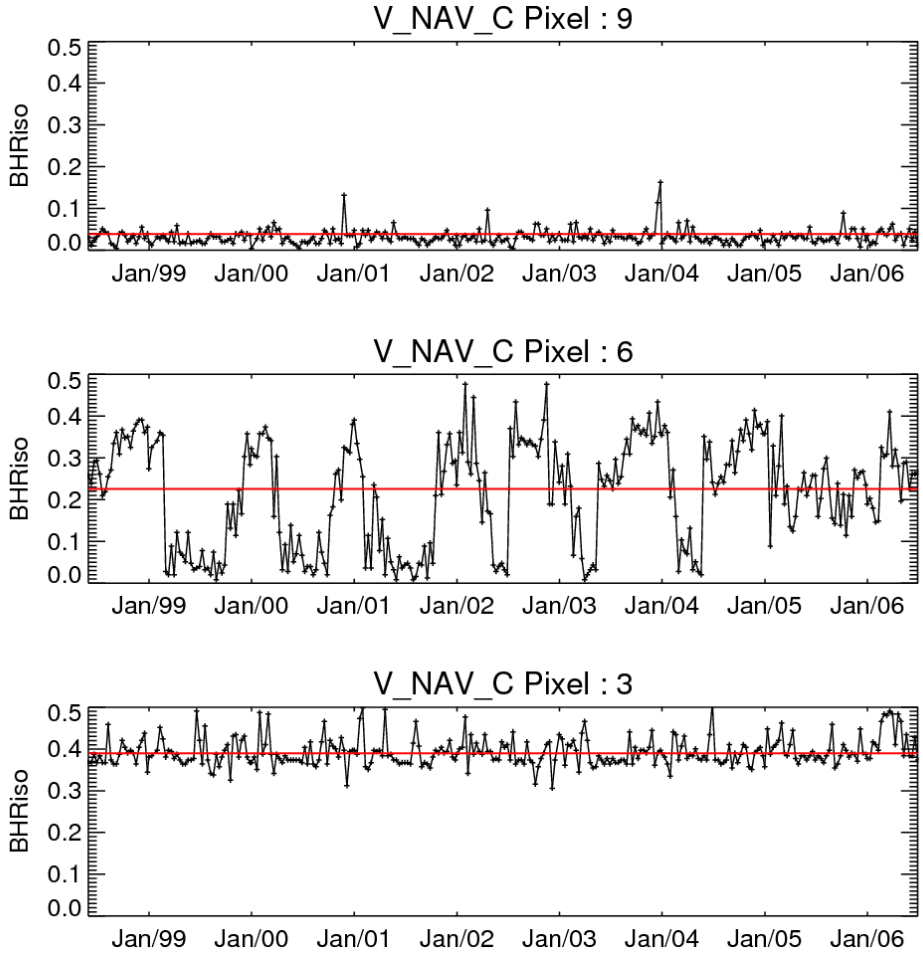


Figure 10: Example of MVIRI-7 time series of BHR_{ISO} for pixel 9 (ocean), 6 (coastline) and 3 (land) for test area V_NAV_C. The red solid line gives the long-term average for each pixel.

In a next step, the data was normalized using the following formula:

$$y(t,i) = \left(BHR(t,i) - BHR(t,1)\right) / \left(\langle BHR(t,11)\rangle - \langle BHR(t,1)\rangle\right) \qquad \textit{Equation 3}$$

Where $i \in \{1, \ldots, 11\}$ is the respective pixel position and the brackets <…> indicate the temporal average. This will serve to first-order normalize y to the range between 0 and 1, where a value of 1 would represent surface coverage identical to pixel 11 (entirely water) and a value of 0 would represent surface coverage identical to pixel 1 (entirely land). Coastal pixels adopt values in between these two extremes. This normalization makes the results of the different locations comparable.

Using long-term averages of y, the navigation of the different satellites relative to each other can be studied, as in Section 4.2.4. Looking at the variance of y as a function of pixel position allows a study of the navigation uncertainty within a satellite's time series, see Section 4.2.5.

4.2.4 Average Navigation Offsets between Different satellites

Long-term averages of *y* as a function of the pixel position are shown in Figure 11 for all satellites and transects. This shows inter-satellite navigation differences. The coloured points on the x-axis give the best estimate for the location of the coastline in the transects for each satellite.

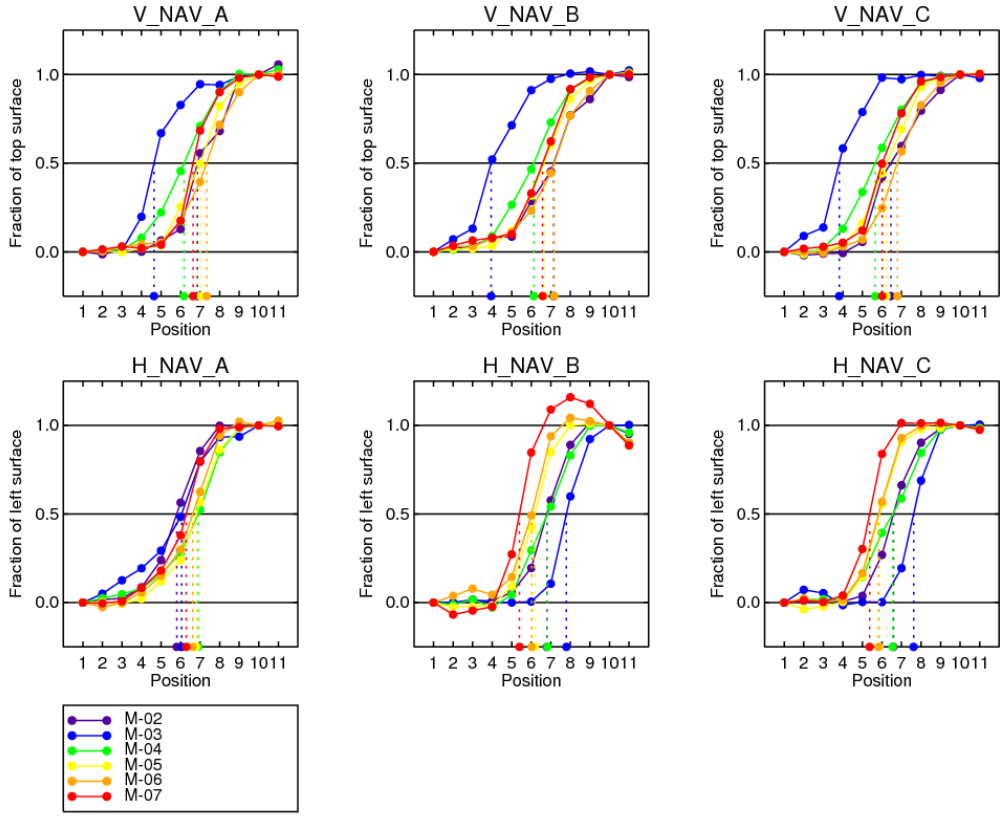


Figure 11: Long-term temporal averages of the function y (t,i) as defined in Equation (3) for all transects and satellites. The dots on the x-axis give the position corresponding to a value of <y(t,i)>=0.5, i.e. a pixel position directly on the coastline.

The following conclusions about inter-satellite navigation accuracy can be drawn:

- With the exception of MVIRI-3, the navigation accuracy of the MVIRIs with respect to each other is approximately one pixel vertically and about 1.5 pixels horizontally;
- MVIRI-3 appears to be shifted consistently to the north by about 1.5 – 2 lines as shown in Figure 11, top row. For example, in reference area V_NAV_B, pixel 4 would be located directly above the coastline for MVIRI-3; it is nominally located between pixels 6 and 7.

4.2.5 Variations for individual satellites

As can be seen in the middle panel of Figure 10 , the pixel nominally positioned above the coastline exhibits a low-frequency (~once per year) variability caused by variations in the actual pixel position relative to the coastline. Superimposed to this systematic variation are random effects dominating the time series of pure ocean or land pixels.

The approach, deriving the navigation uncertainty from this variance, is outlined below. Assuming a linear mixing of water and land surfaces, the variance within each time series caused by geo-location errors can be estimated by solving the following equation for σ_{GEO}:

$$\sigma^2(i) = (1 - f(i))\sigma^2(1) + f(i)\sigma^2(11) + \sigma^2_{GEO}(i) \qquad \textit{Equation 4}$$

where $\sigma^2(i)$ represents the total variance in $y(i,t)$ observed for the i-th pixel. This simple model assumes a linear mixing of noise caused by the surface of pixel 1 (the pixel farthest inland in V_NAV_A) and the surface of pixel 11 (the pixel farthest offshore in V_NAV_A), where $f(i)$ is the average fraction of surface 2 within the pixel and the variability of f is captured in the additional term σ_{GEO}. Except for σ_{GEO} all other quantities can be readily derived from the individual time series, yielding the following expression for σ_{GEO}:

$$\sigma_{GEO}(i) = \sqrt{\sigma^2(i) - (1 - f(i))\sigma^2(1) - f(i)\sigma^2(11)} \qquad \textit{Equation 5}$$

Note: By virtue of the definition of the normalized fractions, σ_{GEO} can be interpreted as the standard deviation in pixel navigation in units of fractions of pixels. For theoretical reasons, $0 \leq \sigma_{GEO} \leq 0.5$, because $y(i,t)$ is normalized between 0 and 1.

For a sequence of N equidistant pixels with identical spatial resolution crossing a coastline, σ_{GEO} is a function of $y(i,t)$ only, as all three lengths scales involved can be expressed as function of just the sampling distance between two pixels. The three lengths scales are as follows:

(1) sampling distance between two pixels,

(2) spatial resolution of the pixels, and

(3) the navigation uncertainty.

If the spatial resolution of the pixels is known, the navigation uncertainty can be derived from the form of the curve σ_{GEO} (i). The general idea is outlined in Figure 12 for a simple numerical experiment. As the navigation uncertainty gets larger, more pixels become affected by the coast (the curve gets wider) and the variance for the pixels near the coast increases. For very large navigation uncertainties, the variance does not reach zero anymore for pixels 1 and 11 as they also are partially affected by seeing the coastline.

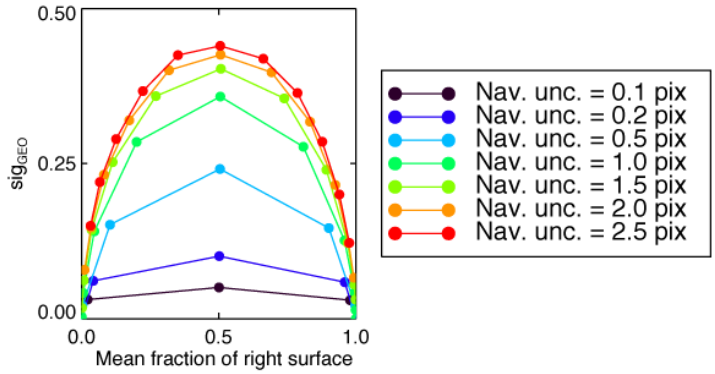


Figure 12: σ_{GEO} as function of the mean fraction of right surface observed in each pixel and as navigation uncertainty derived from a simple numerical experiment over an idealized coastline. The instrument resolution was assumed to be two pixels. The colours indicate different navigation uncertainties.

The same type of plot is shown for the actual MSA observations in Figure 13. Comparing the results obtained for each MVIRI for the vertical cases (V_NAV) to the theoretical curves allows for an estimation of the average navigation uncertainty. The resulting numbers are given in Table 6.

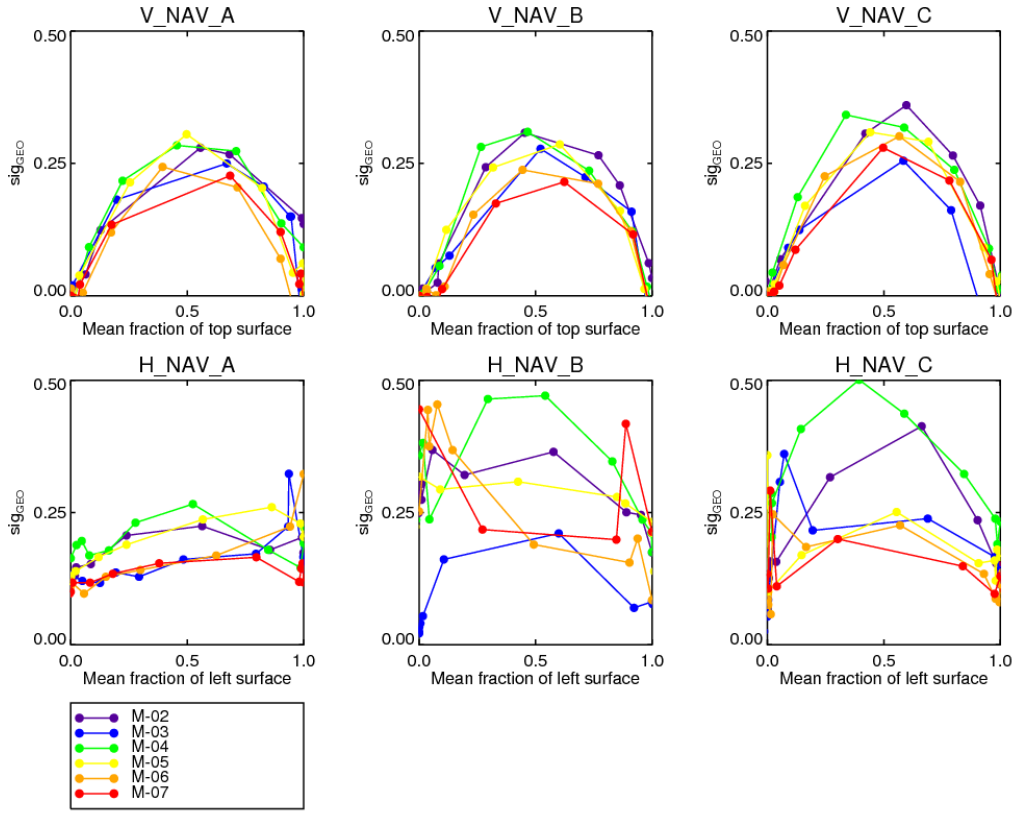


Figure 13: Similar to Figure 12 but for standard deviations from actual MSA observations for all test areas. The colours indicate the different Meteosat satellites.

Due to stronger noise, the same analysis was not possible for the horizontal cases (H_NAV). An in-depth analysis of individual scenes showed that residual cloud contamination is responsible for the difficulties encountered. Considering the scope of the study, it was decided to not analyse the horizontal navigational uncertainty any further.

Instrument	*V_NAV*	*H_NAV*
MVIRI-2	1.7	-
MVIRI-3	1.6	-
MVIRI-4	1.8	-
MVIRI-5	1.6	-
MVIRI-6	1.4	-
MVIRI-7	1.2	-

Table 6: Vertical navigation uncertainty in units of MVIRI VIS pixels. The horizontal navigation uncertainty could not be assessed due to residual cloud contamination.

4.3 MVIRI Stability and Consistency

4.3.1 Site selection

Four desert targets were selected as sites to assess the long-term stability of the MSA data record. Table 12 in Appendix A.1.4 gives extensive details on the sites chosen. . In addition to constant surface properties, these sites are also characterised by limited residual cloud contamination:

Location	*Description*	*Comment*
Murzuq Desert	Homogeneous and very bright surface	
Libya	Homogeneous and bright surface previously used for vicarious calibration	[Rao et al., 1999];
Egypt One	Homogeneous and bright surface previously used for vicarious calibration	[Knuteson and Revercomb, 2004];
Omani Desert	Homogeneous and rather bright surface, excellent overlap by both 0DEG and IODC areas.	

4.3.2 Time Series for Selected Sites

Time series of DHR_{30} for the four different sites are shown in Figure 14. Time series of BHR_{ISO} and the position of the sites in the 0DEG, IODC_57 and IODC_63 disks are additionally shown in the annex (Figure 38 to Figure 41). Narrow-band to broadband conversion was performed using the empirical coefficients provided by Loew and Govaerts [2010]. The following is apparent from the plots:

- The individual time series of both 0DEG and IODC are very homogeneous, as already outlined by Loew and Govaerts [2010];
- Systematic and occasionally significant differences between the 0DEG and IODC areas exist. These differences are analysed in more detail in Section 4.5.

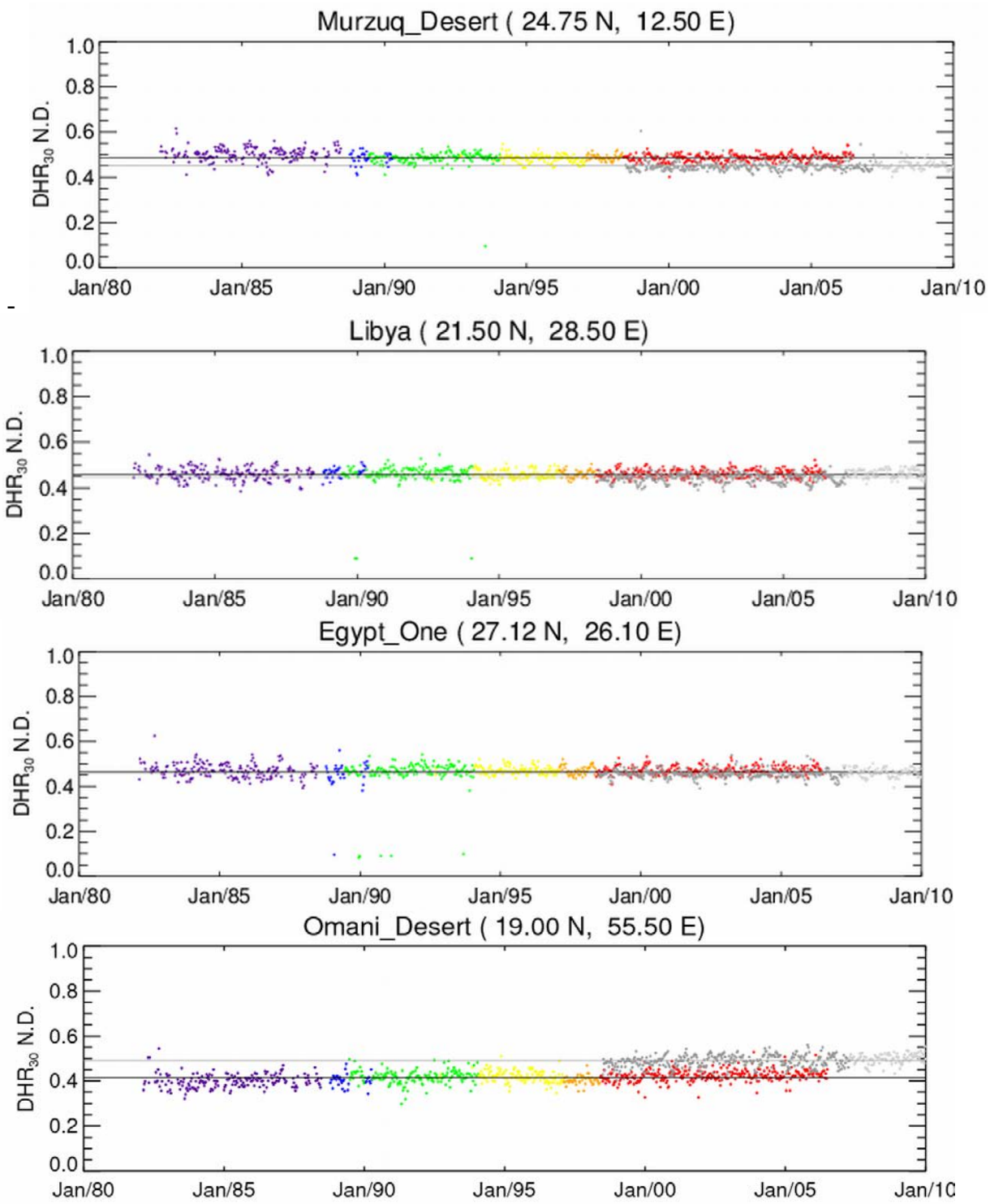


Figure 14: DHR_{30} time series for four desert sites. The colours represent the different MVIRIs on the 0DEG disk from MVIRI-2 (violet) to MVIRI-7 (orange). Dark grey represents MVIRI-5 and light grey MVIRI-7 data covering the IODC.

Notably, the central Saharan vicarious calibration sites “Libya” [Rao et al., 1999] and “Egypt One” [Knuteson and Revercomb, 2004] and, to a slightly lesser degree also “Murzuq Desert” appear to be temporally extremely stable, as shown in Table 7. Similar stability is observed for further sites in both arid and non-arid areas. See Annex C, Figure 43 to Figure 46.
Note: The apparent negative trend for DHR30 under 0DEG at the “Murzuq desert” site is caused by the higher MVIRI-2 values. If these data are removed from the regression analysis, the long term trend is significantly reduced.

One exception is the Omani Desert site, where a trend towards increasing surface albedo is found, especially in IODc observations. It is unclear yet whether these trends are spurious or if they reflect real land cover changes.

Based on the results of the regression analysis presented in Table 7 as well as on the findings of Loew and Govaerts, [2010], the temporal stability of the MSA dataset is assumed to be less than ±0.01 per decade.

Name	***0DEG***		***IODC***	
	BHR [1/decade]	DHR [1/decade]	BHR [1/decade]	DHR [1/decade]
Murzuq desert	-0.0084	**-0.0325**	0.0102	0.0099
Libya desert	0.0037	-0.0085	-0.0011	-0.0011
Egypt One	0.0083	0.0071	-0.0006	-0.0006
Omani desert	**0.0170**	**0.0133**	**0.0437**	**0.0421**

Table 7: Regression slopes of the datasets shown in Figure 38 to Figure 41. IODC data are restricted to the 63° coverage (MVIRI-5) to avoid potential effects caused by the different observation angles of IODC_63 and IODC_57. Regression slopes exceeding ±0.01/decade in bold.

4.4 Aerosol effects

This section aims to assess how far atmospheric effects are correctly considered in the MSA method:

- In the first step, the overall accuracy of the MSA retrieved aerosol optical depth (AOD) was evaluated using the AERONET data as reference;
- In the second step, the MSA-retrieved AOD was spatially analysed against the MACC-II re-analysis.

4.4.1 Aerosol optical thickness against AERONET

To perform a homogenized analysis for the 0DEG and IODC disks, only AERONET stations that are part of both coverages were considered. Furthermore, only stations with a temporal coverage of five years or longer were evaluated. Eighteen AERONET stations were retained for further analysis. The location of these sites is plotted in Figure 15. A list of stations follows Figure 15.

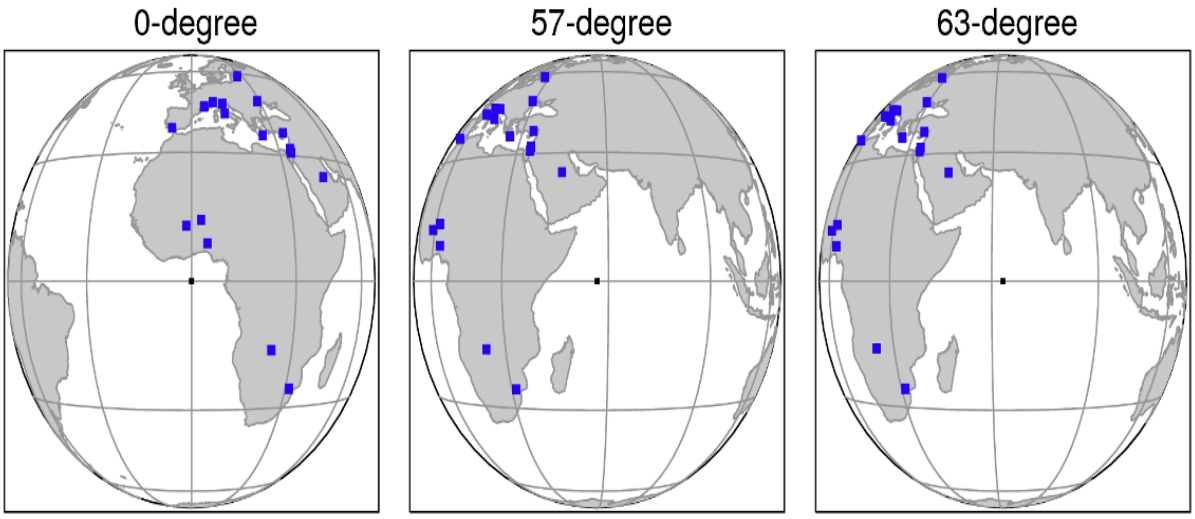


Figure 15: Location of the 18 AERONET sites used in this study.

AERONET stations used: Avignon, Banizoumbou, Carpentras, El_Arenosillo, FORTH_CRETE, IMS_METU_ERDEMLI, Ilorin, Ispra, Moldova, Mongu, Nes_Ziona, Ouagadougou, Rome_Tor_Vergata, SEDE_BOKER, Skukuza, Solar_Village, Toravere, Venise.

To make the MSA and AERONET products compatible, two pre-processing steps were required:

- The AERONET AOD, which is specified for 675 nm, was referenced to 550 nm (reference wavelength of the MSA AOD) by using the Angstrom coefficient derived from concurrent observations at 870 nm;
- AERONET data were averaged to match the 10-day MSA periods. In contrast to DHR30 and BHRISO, the AOD values provided by MSA are averages of the considered 10-day periods.

A set of 1025 collocated MSA-AERONET AOD data pairs was derived using this processing. See scatter plots in Figure 16.The processing leadto the following observations:

- In general, there is a good agreement between MSA and AERONET AOD, even though MSA is based on a continental aerosol model only.
- MSA will inevitably overestimate the AOD for any values less than 0.1. This is due to the fact that the MSA retrieval is bound to discrete AOD values in the range between 0.1 and 1.0. See Table 4.
- MSA seems to slightly underestimate AOD for higher values. However, this statement is based on a limited number of observations as there exist only very few data points with AOD being greater than 0.5.
- Statistically, the AODs from IODC and 0DEG show a very similar performance against AERONET.

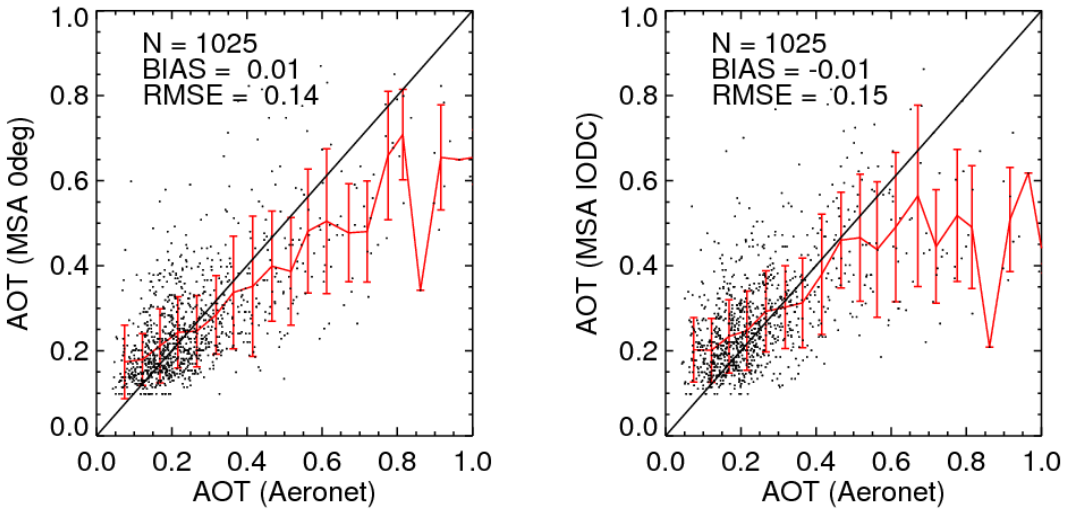


Figure 16: Comparison of AERONET and MSA aerosol optical depth (AOD). Left: 0DEG coverage, right: IODC_57 and IODC_63.

4.4.2 Spatial analysis using MACC-II

The analysis of black-sky (DHR_{30}) and white-sky (BHR_{ISO}) albedo over stable targets obtained under high and low aerosol loads provides an independent indication of the accuracy of the atmospheric correction performed by the MSA. The identification of high and low aerosol loads is based on the MACC-II re-analyses found in Section 3.3: MSA observation were sorted into two classes representing high respective low aerosol loads if the corresponding MACC-II AOD was at least half standard deviation above respective below the pixel average over the whole MACC-II reanalysis period (2003-2006).

Figure 17 presents composite fields of DHR_{30} obtained from MVIRI-7 for the high and low aerosol cases defined above. Only albedo values with a probability of fit of at least 90% were considered for the composite mean. The following analysis concerns the Sahara and the Arabian Peninsula, where albedo values are not expected to change significantly over the long term. In contrast, the differences observed over the Sahel region correspond to seasonal changes in vegetation cover, meaning they are associated with a seasonal signal over a non-stable target.

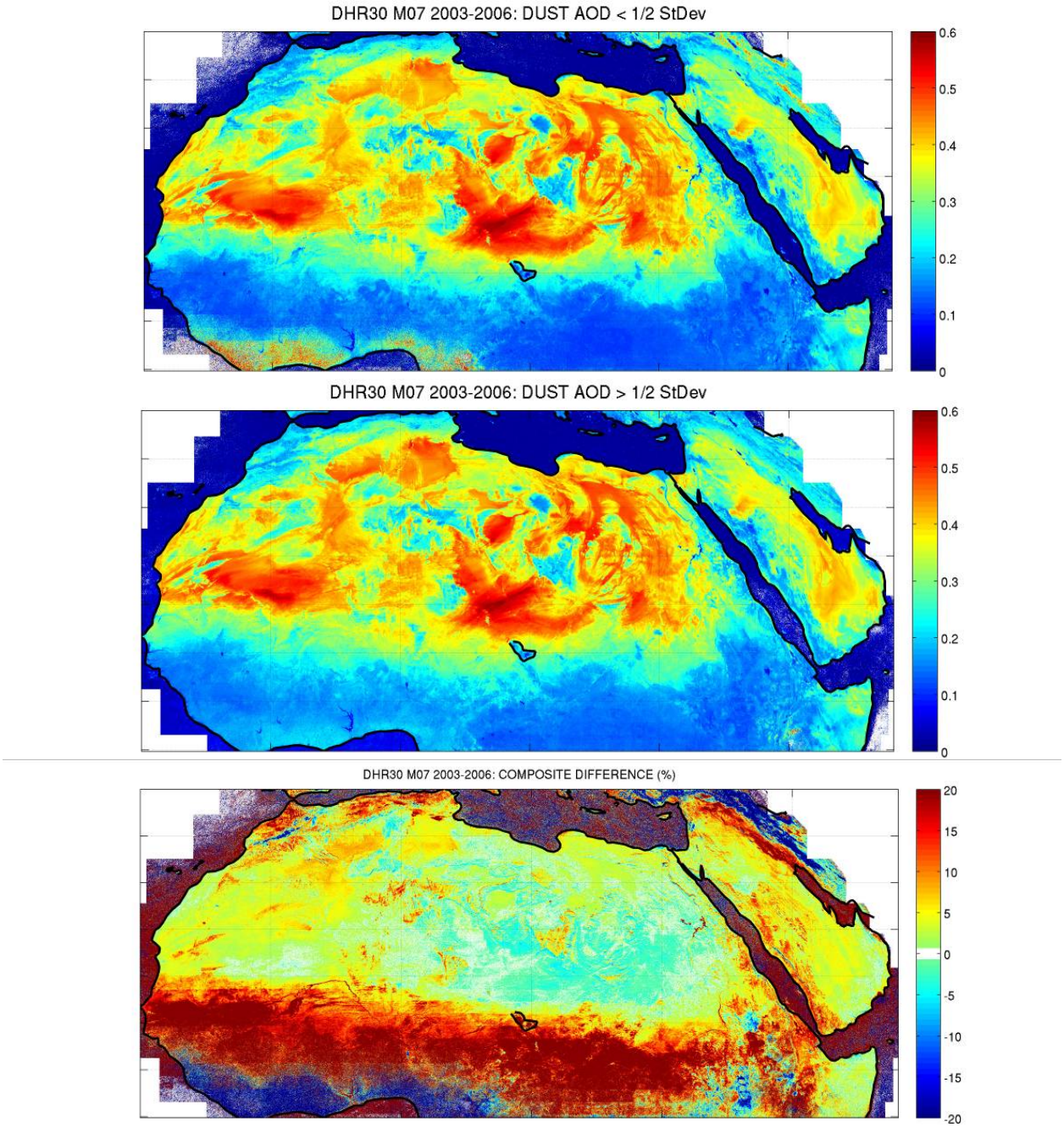


Figure 17: Average of DHR_{30} estimates for the period 2003 to 2006 for cases where dust AOD is higher, (top) resp. lower (middle) than its climatology by at least half a standard deviation;. Bottom panel shows the relative difference between high and low AOD retrievals with respect to the low AOD case.

The overall patterns shown in the top panel of Figure 17 and the middle panel as well as the range of observed values appear similar. However, the relative differences between the high and low aerosol load cases reveal DHR_{30} discrepancies between –5% and over +15%. The contrast seems to be particularly pronounced over the Eastern Sahara (Chad, Sudan), where DHR_{30} estimates over dark surfaces tend to be higher for high AOD (these are the positive differences in Figure 17), while bright surfaces appear to be darker under the same circumstances (negative differences).

As shown in Figure 18, these discrepancies are even more pronounced for BHR_{ISO}. Moreover, the differences seem to be more pronounced towards the eastern part of the domain, towards larger viewing angles. This suggests that the viewing geometry also plays a role in the performance of MSA See Section 4.5.

The results indicate the existence of conditional biases in MSA retrievals that depend on the aerosol load. Relative differences between clear and turbid AOD conditions, based on composite averages shown above, may reach values of + 10% to – 20%. This, in turn, may introduce significant deviations in derived quantities like the short-wave radiation budget at the surface.

A relative error δA in the surface albedo A leads to a relative error δSRB in the surface radiation budget (SRB) of $\delta SRB = -\delta A \times A/(1-A)$:

- Assuming a bright surface of A=0.45 and an albedo retrieval error of δA = +10% (a retrieved surface albedo of A = 0.495), the corresponding relative error of the SRB amounts to δSRB = –8.2%. This represents an absolute error as follows:
  $\Delta SRB = -0.082 \times 550\ W/m^2 = -45\ W/m^2$ for an incoming solar radiation of 1,000 W/m².
- Assuming a dark surface of A = 0.15 and an albedo retrieval error of δA = –20%, the corresponding relative error of the surface radiation budget amounts to δSRB = +3.5%, representing an absolute error as follows:

  $\Delta SRB = +0.035 \times 850\ W/m^2 = \pm 30\ W/m^2$ for an incoming solar radiation of 1,000 W/m².

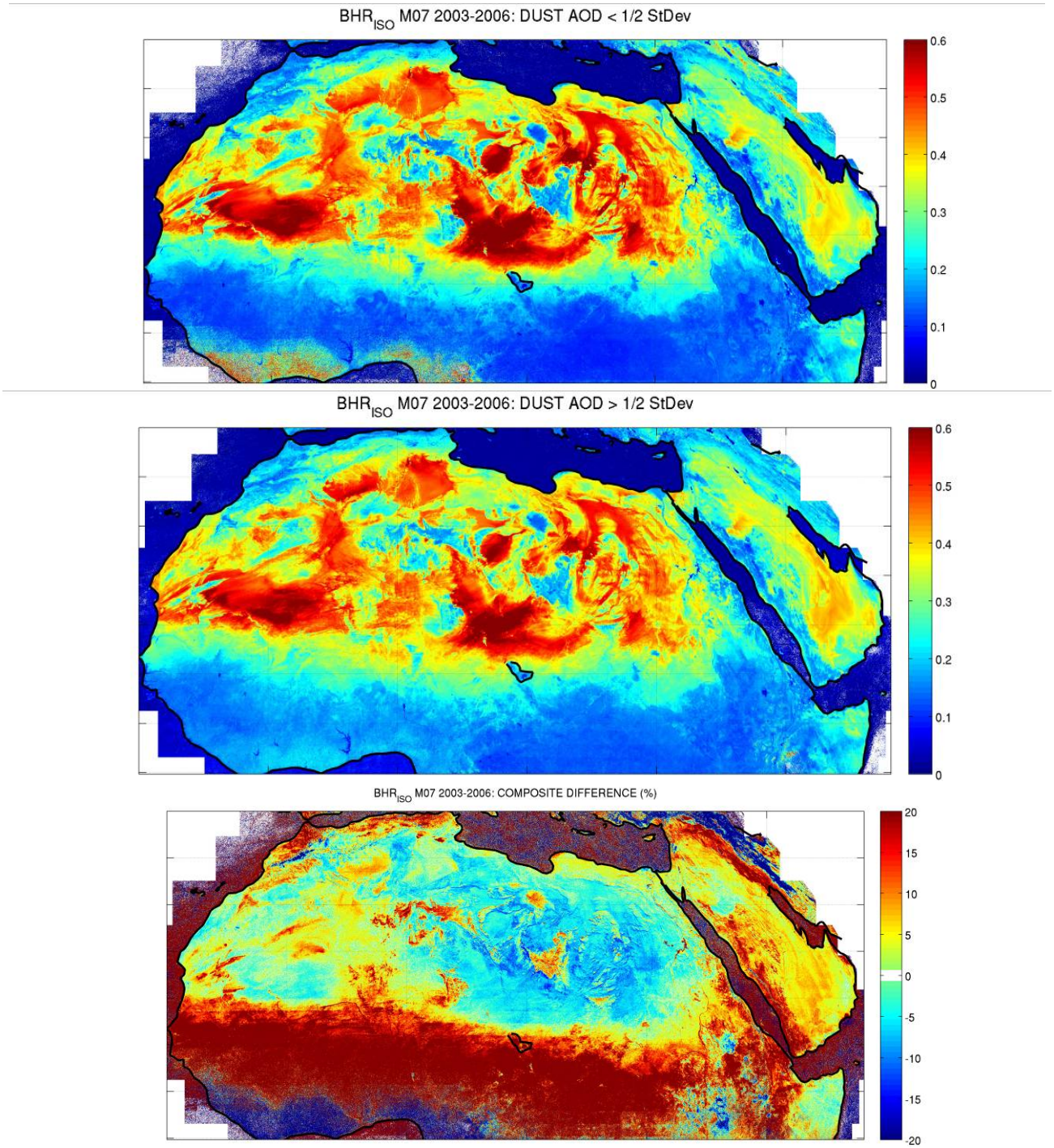


Figure 18: Average of BHR_{ISO} estimates for the period 2003 to 2006 for cases where dust AOD is higher, (top) resp. lower (middle) than its climatology by at least half a standard deviation;. Bottom panel shows the relative difference between high and low AOD retrievals with respect to the low AOD case

4.4.3 Analysis using AERONET data

AERONET data of the "Solar Village" site to the north-east of Ryad, Saudi Arabia have been used to perform an analysis similar to the one shown above. Solar Village is the only AERONET site on the Meteosat disk where the surface albedo can be assumed to be stable over time. Figure 19 shows the results of this analysis: both DHR_{30} and BHR_{ISO} show deviations from their long-term averages correlated with the actual AOD, confirming the existence of biases in MSA surface albedo retrievals depending on aerosol load. The observed deviations for this specific site are mostly confined to a ±10% relative error range of ± 10% and agree well with the results from the spatial analysis shown in section 4.4.2. Following the error estimate presented under 4.4.2 and assuming a surface albedo of A=0.30, this translates into an absolute error of $\Delta SRB = \pm 0.043 \times 700\ W/m^2 = \pm 30\ W/m^2$ for an incoming solar radiation of 1,000 W/m².

The differences between DHR_{30} and BHR_{ISO} and between 0DEG and IODC appear small, which seems to indicate that angular effects do not play a significant role at this specific site. There also appears to be a positive correlation between AOD and deviation from the average. As Solar Village is located in an area characterised by a relatively dark surface (at least for an arid surface), this positive correlation is consistent with previous findings.

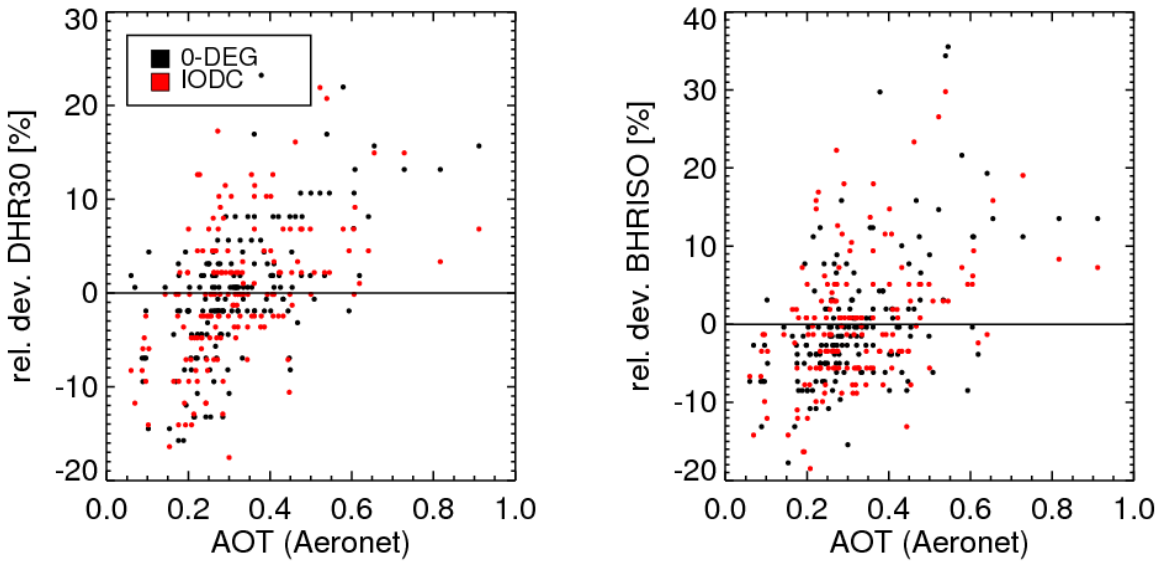


Figure 19: Relative deviation of DHR_{30} (left panel) and BHR_{ISO} (right panel) from their long-term averages as function of the AOD for the AERONET station Solar Village. Relative deviations were calculated as 100.0 (X-⟨X⟩)/⟨X⟩, where X is the time series of either DHR_{30} or BHR_{ISO} and ⟨…⟩ indicates the arithmetic mean.*

4.5 Angular Effects

Comparisons of the surface albedo of one specific area observed under different geometries are possible for concomitant MVIRI observations under different viewing geometries. The most comprehensive dataset in this respect consists of MSA values derived from MVIRI-7 (0DEG) versus MSA values derived from MVIRI_5 (IODC_57) and covers more than five years of concomitant observations. Figure 20 shows the viewing angles of both satellites within the 0DEG-IODC_57 overlap region.

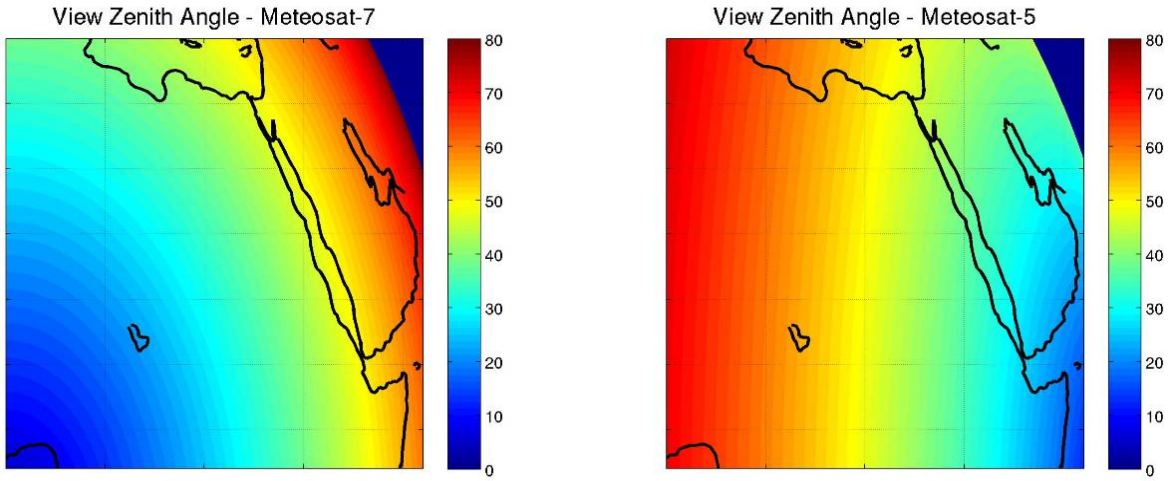


Figure 20: Viewing angle for the MVIRI-7 (0DEG, left) and MVIRI-5 (IODC_57, right) overlapping region in Northern Africa and the Middle East.

A comparison between MSA estimates in the 0DEG and IODC_57 overlapping area suggests the existence of retrieval biases associated with viewing geometry. Figure 21 shows a striking example for the Omani desert surface target, where DHR_{30} resp. BHR_{ISO} is about 0.08 respectively 0.15 higher for the IODC_57 than it is for the 0DEG observation geometry.

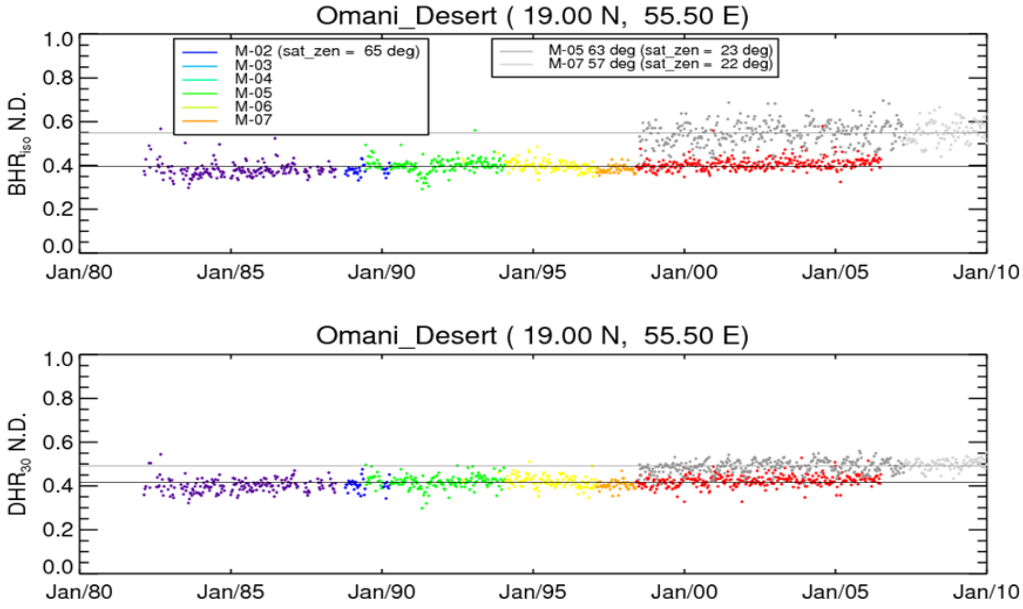


Figure 21: DHR_{30} and BHR_{ISO} time series for a test site in the Omani desert. Large systematic differences are observed for 0DEG (coloured dots) and IODC (grey dots) observations.

4.5.1 Spatial Analysis

Figure 22 shows the DHR_{30} differences between the 0DEG (MVIRI-7) and the IODC_57 (MVIRI-5) observation geometries for the compositing period 1-10 Jan 2006 and for all pixels classified as "barren" according to the IGBP land cover classification. These are grouped by classes of viewing angle difference intervals.

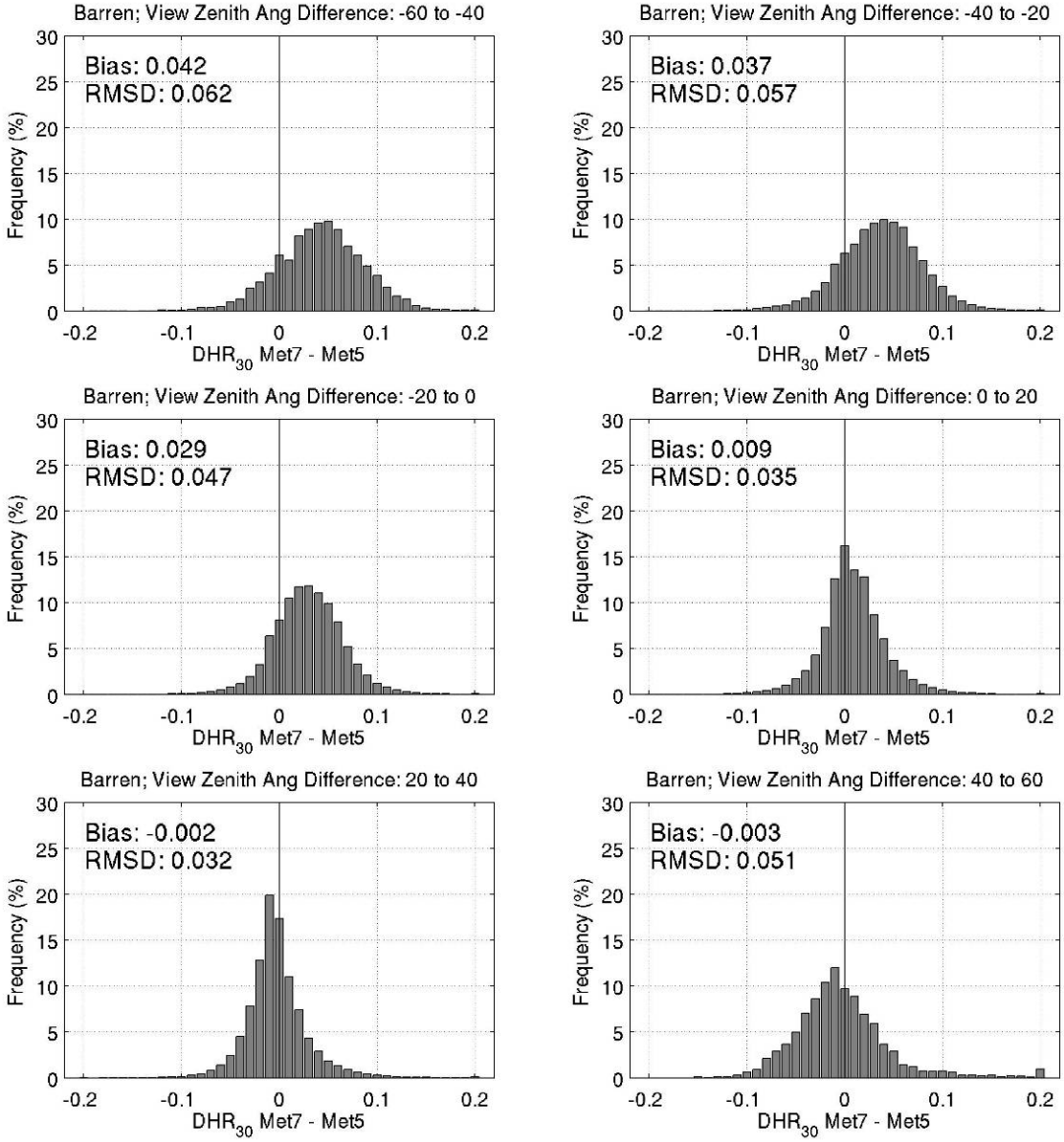


Figure 22: Differences between collocated 0DEG (MVIRI-7) and IODC_57 (MVIRI-5) estimates of DHR_{30} over "barren" pixels within the overlapping region (see Figure 20) for the 1-10 Jan. 2006 compositing period, grouped into viewing angle difference intervals.

Positive differences are where 0DEG are larger than IODC_57 values. The largest positive differences are observed for the largest negative viewing angle differences where 0DEG observation angles are close to nadir, or IODC_57 values are highly slanted (Figure 22, top left panel). The DHR_{30} differences then decrease as absolute viewing angle differences increase.

These decrease from –60/–40 to –40/–20 to –20/0, …. This implies that albedo retrievals tend to be lower for larger viewing angles. This pattern is observed for other periods of the year as well, but these are not shown.

The effect is illustrated as a function of viewing angle difference for DHR_{30}) over barren (desert) surfaces. See the upper panel in Figure 23 . Again, it is even more pronounced for BHR_{ISO} as shown in the lower panel of Figure 23. . Similar behaviour is observed for other land cover types, such as open shrubs and woody savannah. See also Figure 23. The largest differences between averaged MVIRI-7 and MVIRI-5 MSA retrievals are of the order of 0.04 for DHR_{30} and 0.08 for BHR_{ISO}, and are obtained for barren surfaces. Such differences are significant and may lead to significant errors when calculating related quantities such as the SRB. See, for example, the error estimates given at the end Section 4.4.2. In addition to the observed biases, the standard deviation of the differences also tends to be smaller when the viewing angles of the two instruments are close.

It is important to note that the shifts in the distribution are not symmetric: the number of cases where 0DEG (MVIRI-7) retrievals have larger values than those obtained from IODC_57 (MVIRI-5) is higher for all land cover types considered as shown in Figure 22. This is probably a consequence of the uneven distribution of viewing angles in the overlapping region, which is closer to the Meteosat-7 sub-satellite point (Figure 14).

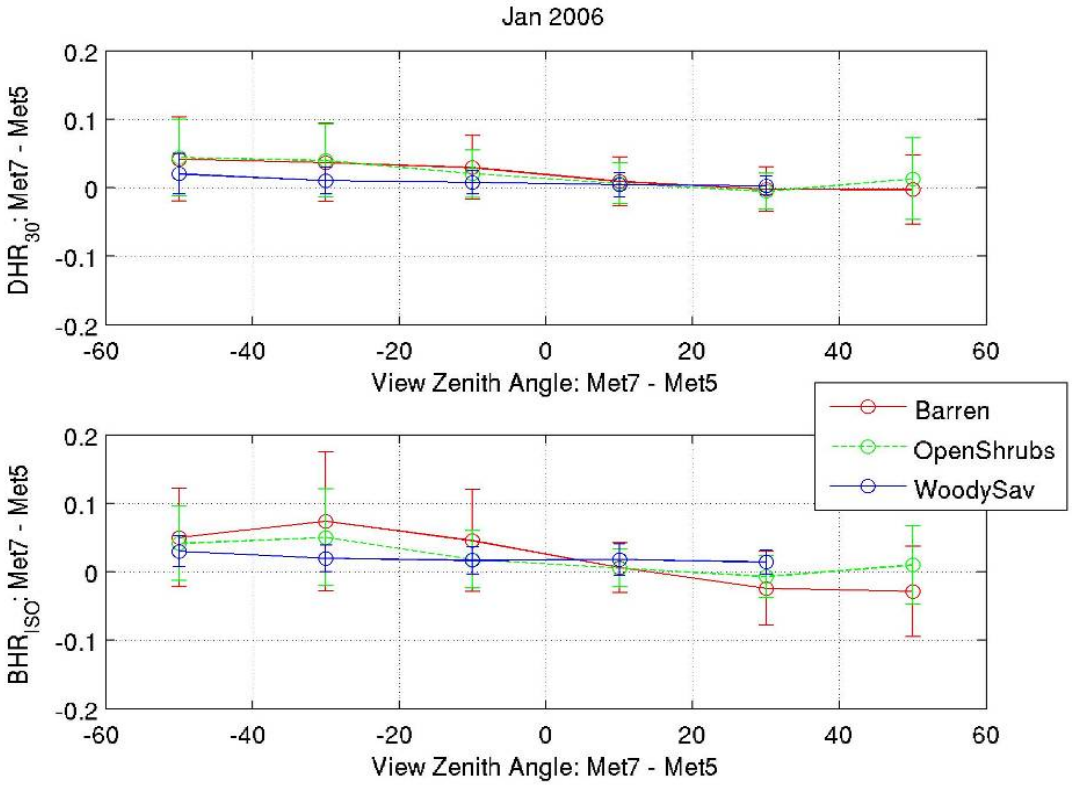


Figure 23: Average (circles) and standard deviation (vertical bars) of the difference between 0DEG (MVIRI-7) and IODC_57 (MVIRI-5) retrievals of DHR_{30} (upper panel) as well as BHR_{ISO} (lower panel) for different land cover types as function of the viewing angle difference.

4.5.2 Temporal Analysis

The agreement between concomitantly-retrieved MSA values for the 0DEG and IODC areas was also studied for the entire overlap period for nine selected sites, this included five desert sites, two high-latitude sites in Europe, and two savannah sites in southern Africa. Names and coordinates of the different sites are given in Table 8. The corresponding time series are shown in Annex C (Figure 38 to Figure 46).

NAME	Latitude	Longitude	Zenith Angle		
			0 deg	57 deg	63 deg
Murzuq_Desert	24.75	12.50	32	56	62
Libya	21.50	28.50	40	40	46
Egypt_One	27.12	26.10	42	46	51
Omani_Desert	19.00	55.50	65	22	23
Solar_Village	24.91	46.40	58	31	34
Toravere	58.25	26.46	70	71	73
Moldova	47.00	28.82	60	60	63
Mongu	-15.44	23.25	32	42	48
Skukuza	-25.02	31.48	45	40	45

Table 8: Specific sites used to study angular effects on the MSA. Also listed are the corresponding satellite zenith angles for the 0DEG, IODC_57 and IODC_63 areas.

Long-term mean values for DHR_{30} and BHR_{ISO} for all considered sites considered are listed in Table 9. The information provided in Table 8 and Table 9 is combined in Figure 24 to show the BHR_{ISO} differences between the 0DEG and IODC areas as a function of the corresponding viewing angle difference. There are systematic deviations, especially for desert sites: whichever instrument observes the scene at a larger zenith angle will, on average, have a lower surface albedo as shown in Figure 24, left panel. This confirms the results from the spatial analysis shown above.

NAME	BHRISO [%]			DHR30 [%]			RANGE of STDV
	0 deg	57 deg	63 deg	0 deg	57 deg	63 deg	[%]
Murzuq_Desert	55.5	46.3	44.4	48.8	45.4	45.0	±1-6
Libya	48.7	50.2	44.6	46.1	46.7	44.1	±1-6
Egypt_One	51.3	48.7	46.1	46.7	46.1	45.5	±1-7
Omani_Desert	39.6	56.1	54.4	41.6	50.2	48.7	±2-6
Solar_Village	29.6	32.4	31.4	31.2	33.6	32.9	±2-4
Toravere	23.8	20.1	20.9	24.7	20.8	21.6	±8-15
Moldova	19.2	14.1	16.3	19.2	14.8	17.1	±6-14
Mongu	16.1	16.7	17.0	17.4	17.8	18.0	±6-9
Skukuza	15.3	14.8	16.1	16.3	15.8	17.1	±4-11

Table 9: Mean broadband values of BHRISO and DHR30 for all sites listed in Table 8, the spectral-to-broadband conversion was performed using the coefficients of Loew and Govaerts [2010]. A rough indication of the standard deviation is also given for each time series.

For the non-desert sites, such a relation is not as obvious as shown in Figure 24, right panel. This does not necessarily mean that vegetated surfaces do not show a similar dependence on the viewing angle. The dependence may just not be visible in the sample data, which cover only a comparably small range of viewing angle differences. In addition, residual cloud contamination is more likely for the vegetated sites potentially adding noise which might hide the signal.

A comparison of the two sites "Omani Desert" (Figure 41) and "Solar Village" (Figure 46) points to possible causes for the observed deviations: Both sites are located in relative vicinity to each other, and differences in their respective observation geometries are comparably small. In contrast, the observed differences in MSA retrieval are large. While Omani Desert shows a systematic deviation of ~0.15 between BHR_{ISO} values for 0DEG and IODC, the corresponding difference for Solar Village is only ~0.02. This indicates that the correction for anisotropy effects has been inconsistent for the Omani Desert surface type and points to the general problem of MSA retrieval errors induced by surface anisotropy.

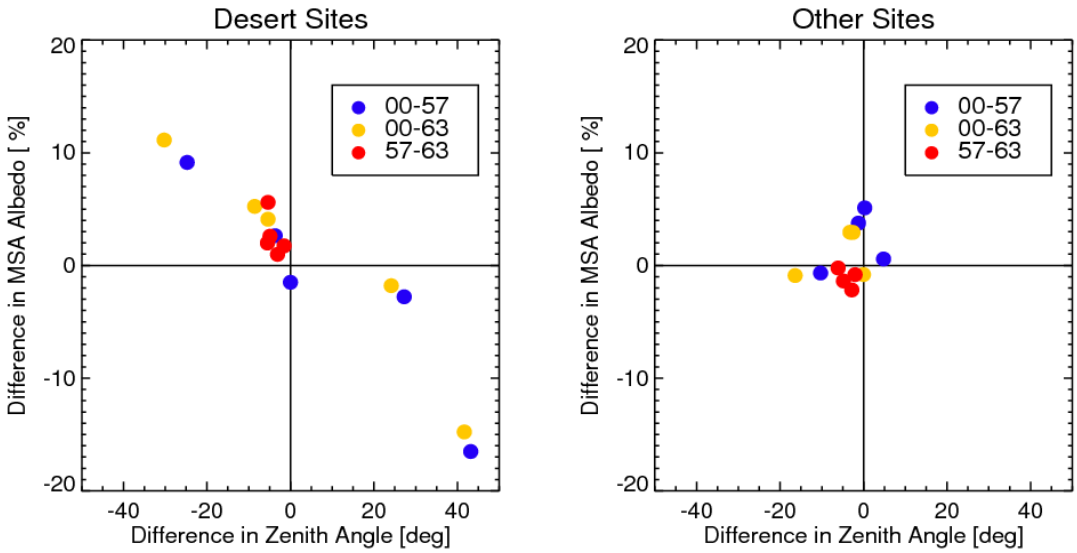


Figure 24: BHR_{ISO} differences as function of satellite viewing angle difference. The left panel shows the five desert sites (rows 1 to 5 in Table 8). The right panel shows the results for the four non-desert sites (rows 6 to 9 in Table 8).

4.5.3 Conclusions on angular effects

As shown above, the observation geometry has a significant impact on the MSA retrieval:

- Non-negligible biases exist between surface albedo estimates for the 0DEG and IODC areas in the overlap region;
- Differences in the observation geometry may lead to systematic deviations in MSA retrievals that can reach values of up to 0.15 for BHR_{ISO};
- Deviations are generally larger for BHR_{ISO} than for $DHR_{30;}$ the reason for this is unknown;
- The angular effects have been confirmed for arid surfaces and possibly exist also for vegetated surfaces. Further study would be required to confirm this assumption.

In the frame of this study, it was not possible to analyse the causes of the observed angular effects in full detail. We presume that insufficient treatment of the surface anisotropy is one of the main reasons for the observed effects, possibly complemented by aerosol-related effects.

4.6 Satellite-to-Satellite Data Comparisons

4.6.1 Comparing MSA with Geostationary Products

MSA estimates from MVIRI-7 were compared with LSA SAF surface albedo retrievals from MSG/SEVIRI by Trigo et al. [2011] for the temporal overlapping period in 2006.

Note: After 2006-07-19, Meteosat-7 was moved to an orbital position over the Indian Ocean (IODC_57). For this purpose, MSG/SEVIRI albedo retrievals were re-projected to MVIRI-7 pixels using the "nearest neighbour" approach.

The LSA SAF albedo products are based on the inversion of a linear kernel-driven BRF model [Roujean et al., 1992; Geiger et al., 2008], using clear sky surface reflectances for the three SEVIRI short-wave channels centred at 0.6, 0.8, and 1.8 μm. The LSA SAF provides daily retrievals of black-sky and white-sky albedo, making use of albedo estimates from previous days as *a priori* information in order to reduce the sensitivity to outliers or to missing data due to cloud cover. The assumed confidence in the *a priori* estimates decreases exponentially with time [Geiger et al., 2008]. The impact of cloud contamination is likely to be significantly lower for the SEVIRI surface albedo retrieval based on these factors:

- The SEVIRI cloud screening takes advantage of the instrument's better spectral resolution;
- The SEVIRI 15-minute temporal frequency increases the chances of gathering clear sky observation;
- Using *a priori* information will tend to reduce the impact of outliers on the final product.

Figure 25 presents albedo estimates from MVIRI-7 and SEVIRI obtained for the 1-10 Jan 2006 compositing period. Following the recommendations stated in the Product User Manual, only MSA retrievals with a probability of fit higher than 90% were considered in the analysis. The observed differences in surface albedo are unevenly distributed. While the bright arid surfaces in the Sahara and Arabian Peninsula present mostly higher values obtained with MSG, the opposite scenario appears over vegetated surfaces not only in central and southern Africa and the Iberian Peninsula, but also over dark arid surfaces in the central Sahara. The circular artefacts observed in the BHRISO difference image in the image at bottom right probably result from mapping the MSG/SEVIRI albedo on the MVIRI grid.

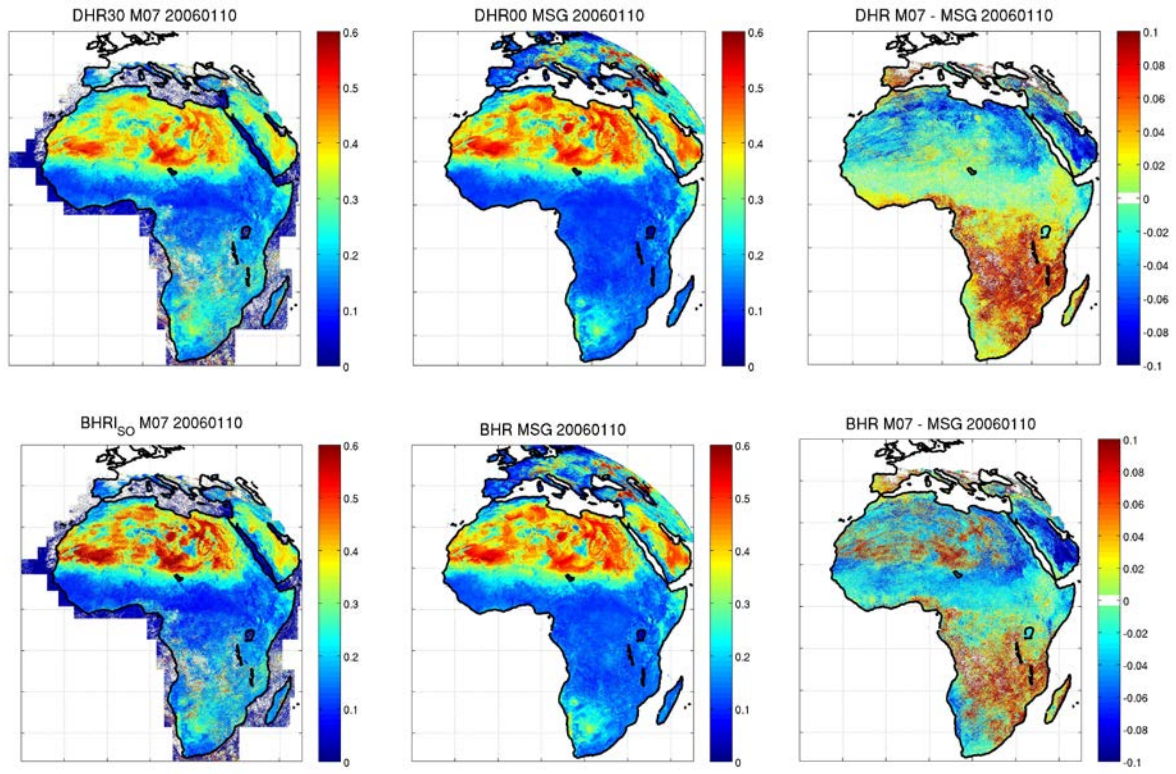


Figure 25. Upper panel: MSA DHR_{30} for the 1-10 Jan 2006 compositing period (left); average of daily values of SEVIRI black sky albedo obtained for the same period (central panel) and the difference [MVIRI-7– SEVIRI] (right). Lower panel: As above, but for white sky albedo (BHR_{ISO}).

These findings support the previously-stated assumption that the atmospheric correction part of the MSA algorithm seems to cause, on average, underestimation of the retrieved surface albedo above bright surfaces and overestimation above dark surfaces. In addition, the effects of residual cloud contamination are clearly visible, especially along the Gulf of Guinea coastline and large parts of central Africa.

Figure 26 and Figure 27 provide insight on the joint distribution of MVIRI-7 and SEVIRI estimates for barren surfaces, as discriminated by the viewing angle. Several aspects are worth mentioning:

- Black-sky albedo (DHR) generally presents better agreement and less scatter than white-sky albedo (BHR), even taking into account that the LSA SAF algorithm estimated DHR using local noon as reference, while MSA refers to the 30º solar zenith angle.
- In both cases, (DHR and BHR, discrepancies increase with the viewing angle: MSA estimates appear to become systematically lower with respect to SEVIRI retrievals as the angle increases. Analysing the uncertainty of MSA products for larger viewing angles might provide further insight into the reasons for the observed differences.
- MSA BHR values are systematically higher by 0.1 and more than their SEVIRI counterparts above MSG BHR values of about 0.45. This might be associated with an inadequate fitting of the narrow-to-broad band conversion due to the limited number of observations for very bright surfaces [see also Govaerts et al., 2006; Loew and Govaerts, 2010].

These results are very similar for the remaining compositing periods of 2006.

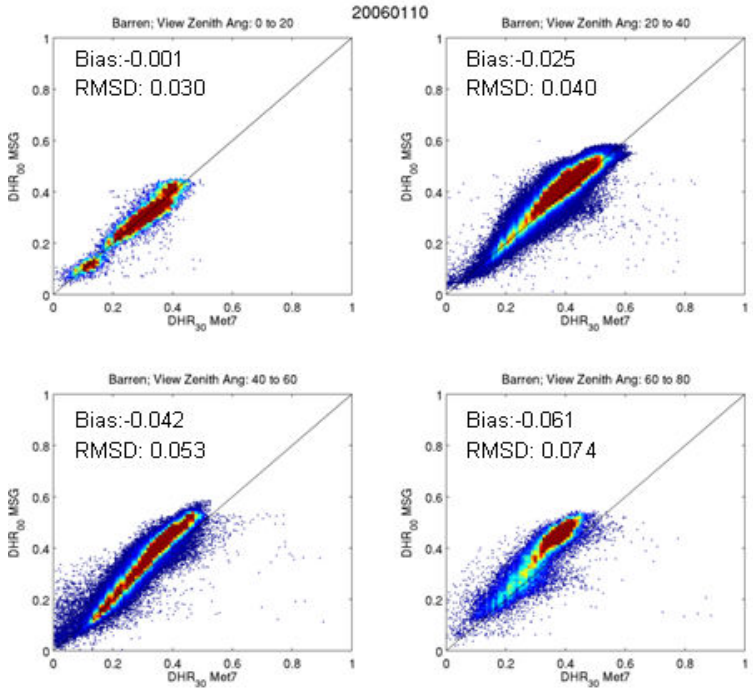


Figure 26: Scatterplots of MSA DHR_{30} (x-axis) vs. SEVIRI black-sky albedo (y-axis) for pixels classified as "Barren" for the 0DEG coverage for the 1-10 Jan. 2006 compositing period. Pixels are grouped according to MSA viewing angle ranges indicated in the top of each panel. Average (bias) and RMS differences within each angular range are also shown.

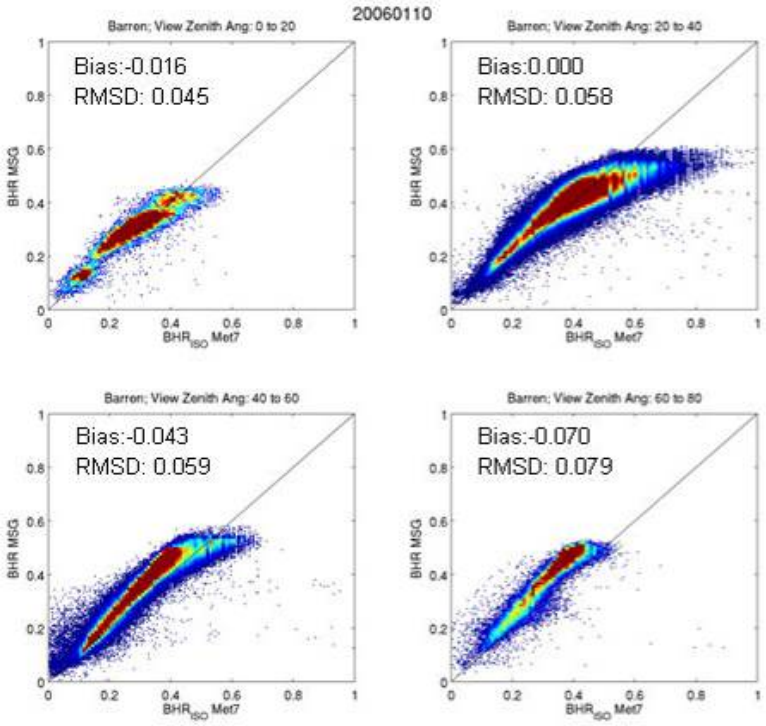


Figure 27: Scatter plots of MSA BHR_{ISO} versus SEVIRI white-sky albedo (y-axis) for pixels classified as "barren" for the 0DEG coverage for the 1-10 Jan. 2006 compositing period. Pixels are grouped according to MSA viewing angle ranges indicated in the top of each panel. Average (bias) and RMS differences within each angular range are also shown.

The scatter plots in Figure 26 and Figure 27 show a number of MVIRI-7 retrievals with very high values, which is typical of estimates from cloud-contaminated observations. Residual MSA cloud contamination is a much larger problem over dark, vegetated areas due to higher cloud occurrence and the larger retrieval errors caused. Figure 28 shows a comparison of MSA vs. LSA SAF albedo retrievals for pixels classified as evergreen broadleaf forest, dominant in tropical Africa. The long horizontal "tails" shown in the scatter plots represent MSA retrievals from observations assumed valid but nevertheless obviously cloud contaminated. As a consequence of the meridional shifting of the intertropical convergence zone (ITCZ), the occurrence of spurious albedo estimations in each view zenith angle range changes throughout the year, but this is not shown in these plots.

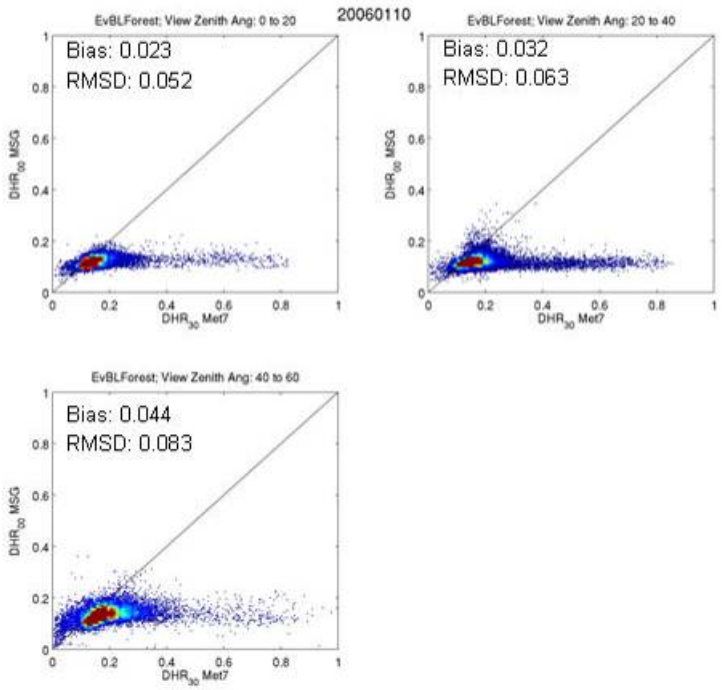


Figure 28 Scatterplots of MSA DHR_{30} (x-axis) vs. SEVIRI black-sky albedo (y-axis) for pixels classified as "evergreen broadleaf forest" for the 0DEG coverage for the 1-10 Jan. 2006 compositing period. Pixels are grouped according to MSA viewing angle ranges indicated in the top of each panel. Average (bias) and RMS differences within each angular range are also shown.

4.6.2 MSA with Polar-orbiting Products

MSA values have also been compared to a number of albedo products derived from polar-orbiting instruments. In a preparatory step, MSA values from MVIRI-5 and MVIRI -7, as well as the surface albedo products from GlobAlbedo, MODIS Collection 5 and MISR obtained for the year 2005 were projected into a latitude-longitude grid at 0.05º and 0.5º resolution.

Individual comparisons between the MSA and the corresponding MODIS and respective MISR surface albedo products encompassing globally all matches for the year 2005 are shown in Figure 29. There is generally good agreement for albedo values up to about 0.25. For brighter surfaces, MSA estimates are systematically larger than those of the two other products. The lower almost horizontal branch in both panels is likely due to residual cloud contamination in the MSA product, similar to Figure 28. Qualitatively, these results are similar to those obtained when comparing MSA to the SEVIRI albedo product.

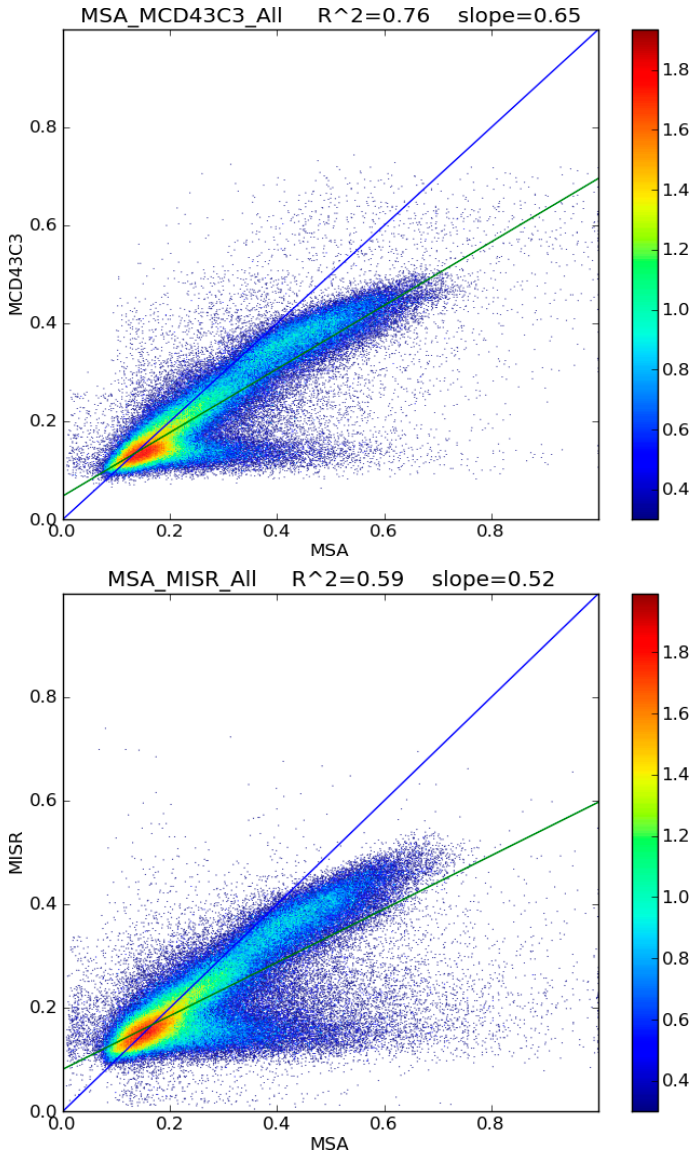


Figure 29: Scatterplots of MSA vs. MODIS Collection 5 (top panel) and MISR (bottom panel) surface albedo products.

4.7 Cloud Screening

In this section, we explore possible criteria used to filter out cloud-contaminated MSA retrievals by examining two quality indicators distributed with the MSA product: *probability of fit* and *retrieval uncertainty*. As mentioned before, MSA retrievals with a probability of fit lower than 90% were excluded from further analysis. However, this criterion does not seem to be sufficient to eliminate problematic estimates.

Figure 30 shows histograms of estimated MSA retrieval errors for "evergreen broadleaf forest" pixels, exhibiting highly skewed distributions. It is worth noting that the cloudiest amongst the four periods shown (Jan. 2006) is also the one presenting the largest uncertainties. This indicates that the uncertainty values provided as part of the MSA contains information on product quality which may be used for attempts to reduce the number of cloud-contaminated pixels.

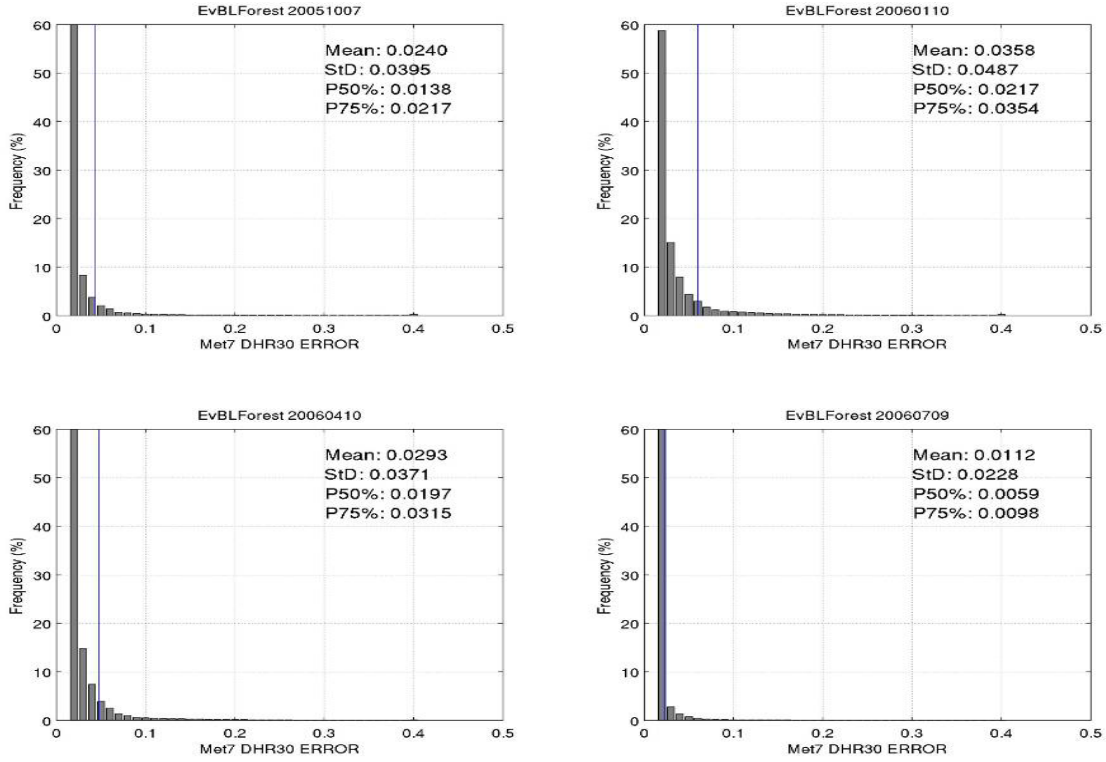


Figure 30: Distribution of MSA estimated retrieval uncertainty for "evergreen broadleaf forest" pixels, for the 4 compositing periods: 28 Sep.-7 Oct. 2005; 1-10 Jan. 2006; 1-10 Apr. 2006 and 30 Jun. -9 Jul. 2006. The blue vertical line indicates the mean uncertainty plus half standard deviation, which is the proposed threshold used to eliminate residual cloud contaminated pixels.

One way to eliminate clearly misclassified pixels is to discard (for a given land cover type) all estimates with uncertainty exceeding the average by more than a given threshold. Figure 31 shows the scatter plots from Figure 28 after cases with errors exceeding the average retrieval error by more than half standard deviation have been eliminated. This is the blue line plotted in Figure 30. This seems to be a fairly effective criterion for desert sites. Tropical forests, however, undergo long periods with frequent cloud cover, which makes it very difficult to disentangle "good retrievals" from cloud-contaminated retrievals. As an alternative, users could also apply a fixed threshold on the retrieval uncertainty (0.05) for all land cover types; such a threshold would allow the elimination of problematic retrievals, with the exception of areas with nearly permanent cloud cover.

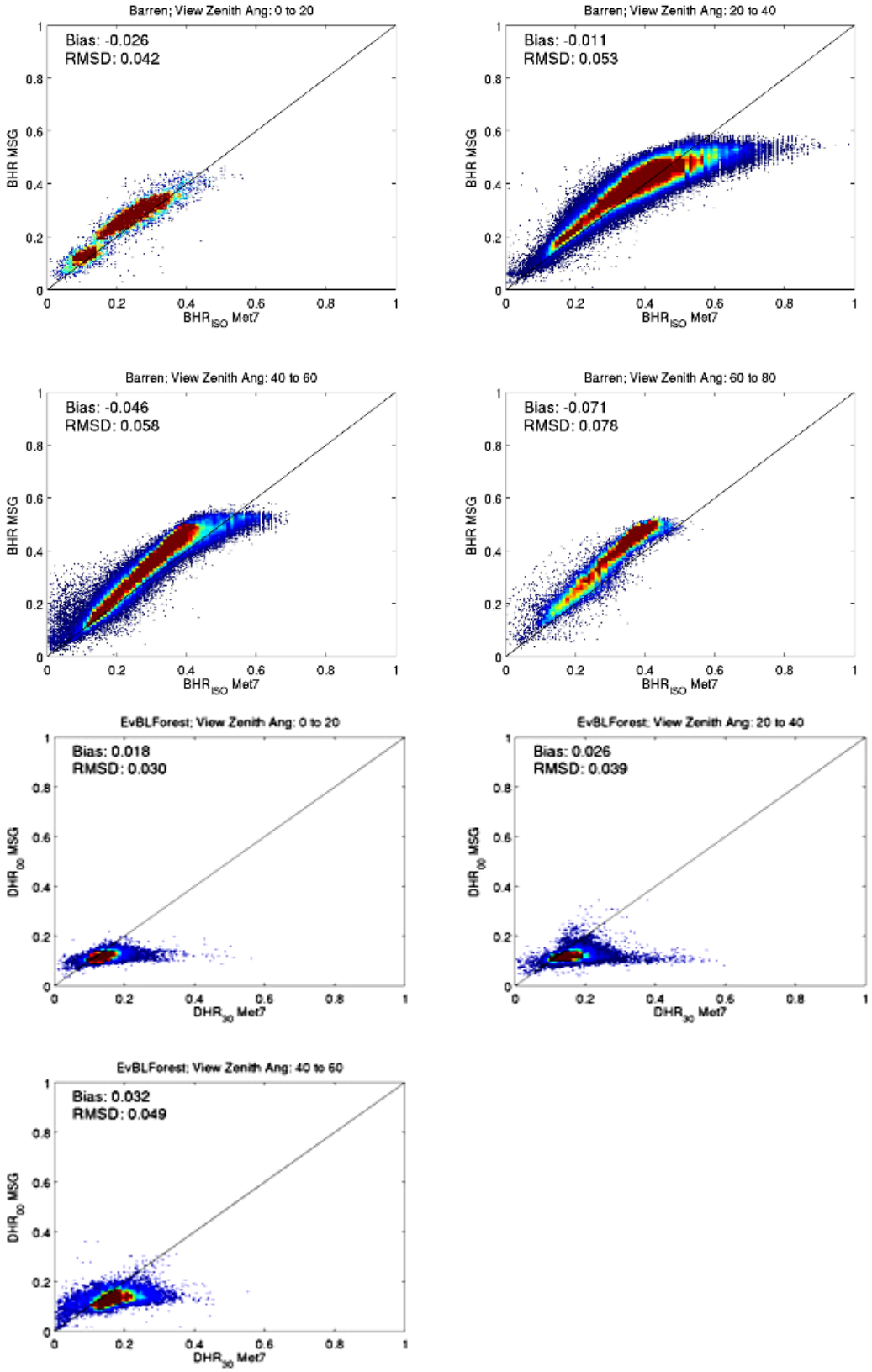


Figure 31: As shown in Figure 27 and Figure 28, but with retrieval errors additionally fulfilling this condition: retrieval error is less than mean retrieval error + 0.5 standard deviation for surface types "barren" (upper four left panels) and "evergreen broadleaf forest" (lower three panels).*

Other techniques for eliminating outliers within the albedo estimates, such as disregarding all DHR_{30} retrievals higher than their average by more than 3 standard deviations were also attempted. However, this criterion creates artificial cuts in the distribution of the product without effectively masking out all cloud-contaminated pixels.

4.8 Comparison with Surface Reference Sites: MODIS Era

For all FLUXNET reference sites where tower albedometer data was available, Aerosol Optical Depth (AOD) values or direct-to-diffuse irradiation measurements made on-site were used to calculate a blue-sky albedo with each EO-derived DHR/BHR. This process is discussed in Eq. 1 in Liu et al. [2009]. Making the assumption that the tower footprint could be linearly scaled up to the EO pixel size, time series were derived for the investigated FLUXNET sites for all of 2005.

Surface albedo values derived from satellites are compared to the corresponding blue-sky albedo gathered at 19 FLUXNET sites in

Figure 32. From this figure, it becomes obvious that many FLUXNET sites are probably not well-suited for the validation of space-borne surface albedo retrievals, especially for pixels the size of MSA.

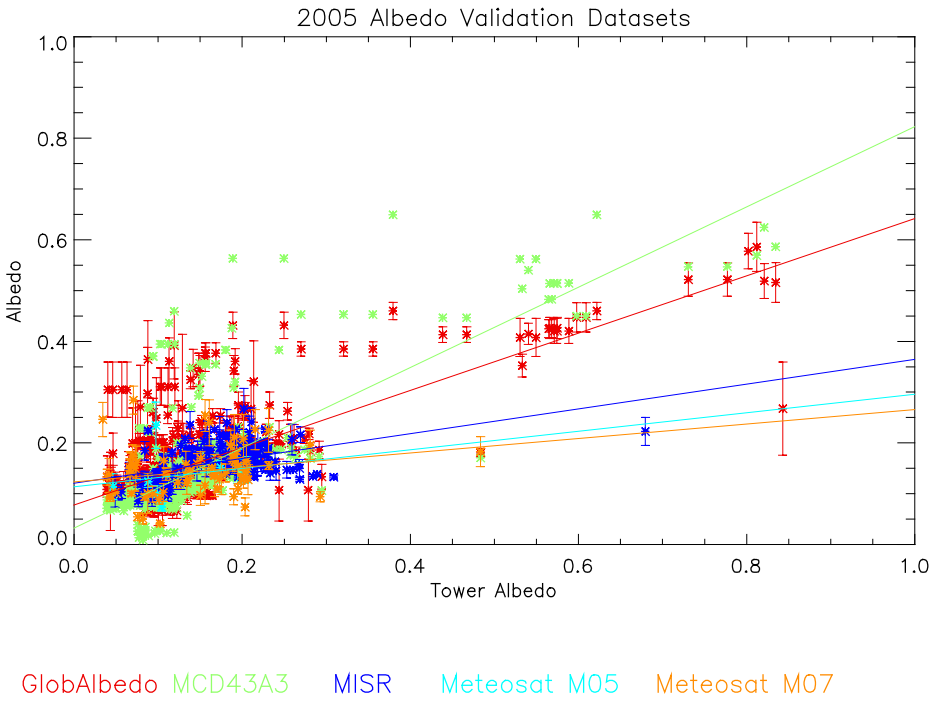


Figure 32: Scatter plot for 19 FLUXNET sites within the MSA geographical coverage.

Looking at individual sites, the reasons for the limited correlation of FLUXNET and satellite-derived surface albedo become clearer: In both cases shown in
Figure 33, the satellite-derived albedo products agree quite well among themselves (with the exception of occasional outliers) but some deviate systematically from the FLUXNET data. Here are some examples:

- The FLUXNET-observed surface albedo increase in DE_HAI between April and June 2005 is not fully represented in the satellite derived data. However, later in summer and autumn the agreement is very good;

- Larger systematic differences are observed for the FLUXNET site HU_BUG. Here, the satellite-derived albedo values agree well and are rather constant for most of the year with a shallow minimum around DOY 240. Ground truth data at this site are systematically higher with deviations increasing from about 0.03 in March 2005 to about 0.08, which is about 50% above the satellite-derived values, in late October and early November 2005.

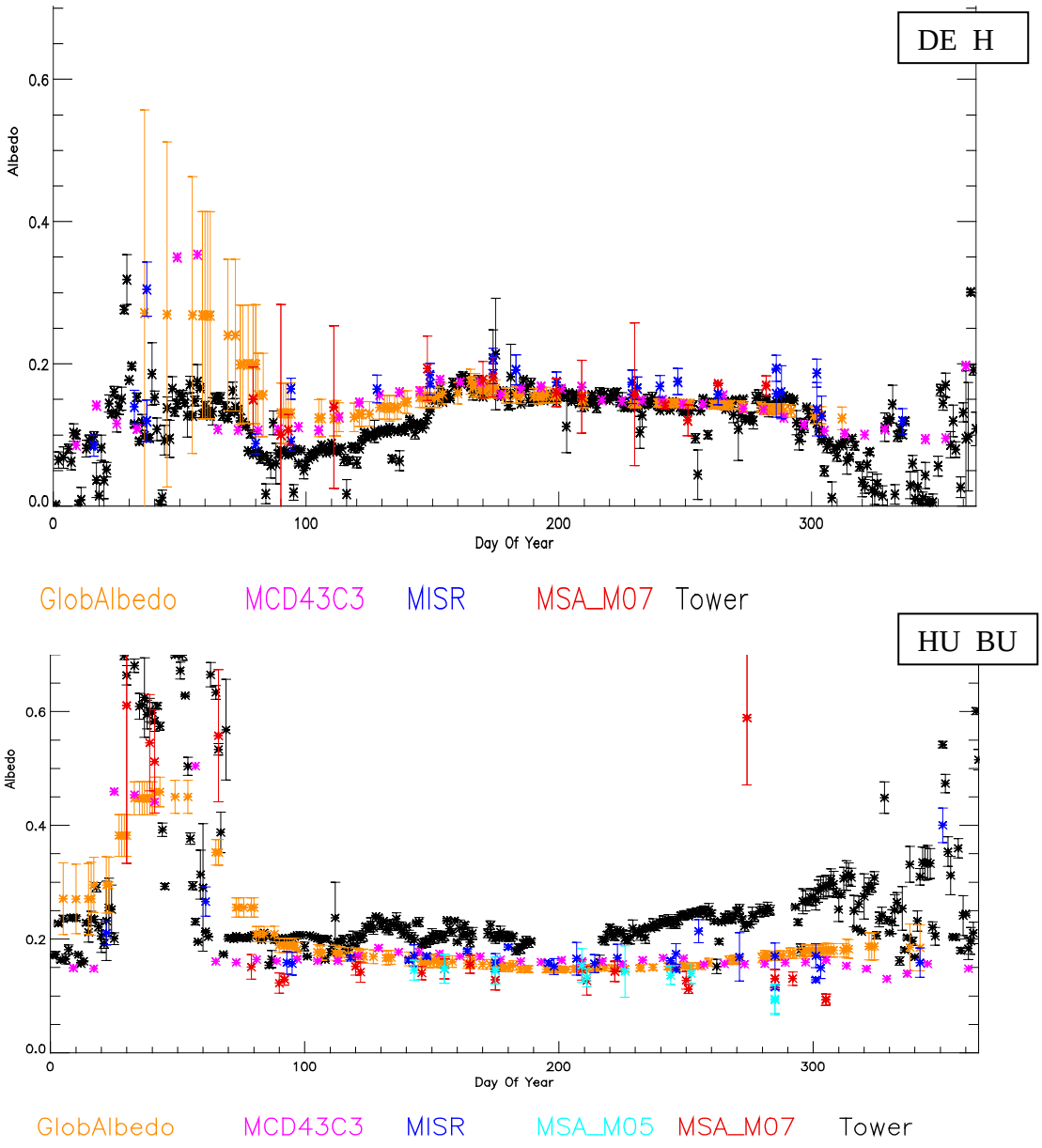


Figure 33: Comparison of FLUXNET ground truth data ("Tower") against surface albedo products from GlobAlbedo, MODIS ("MCD43C3"), MISR, MSA on MVIRI_5 (IODC) and MVIRI_7 (0DEG) for one site in Germany (DE_HAI, IGBP: deciduous broadleaf forest) and one site in Hungary (HU_BUG, IGBP: cropland).

In both cases, it appears that the FLUXNET data is not fully representative of the average land cover within a satellite pixel and, as such a FLUXNET footprint cannot be linearly scaled up to MVIRI-size pixels.

Box-and -whiskers plots that provide a statistical overview on the albedo retrieval from the different sources are shown in Figure 34 for the two FLUXNET sites: DE_HAI and HU_BUG. The horizontal line in the box represents the mean. In some cases, an additional thin line represents the median. The box itself covers the percentile range of 25% – 75% and the whiskers mark the percentile range of 12.5% – 87.5%.

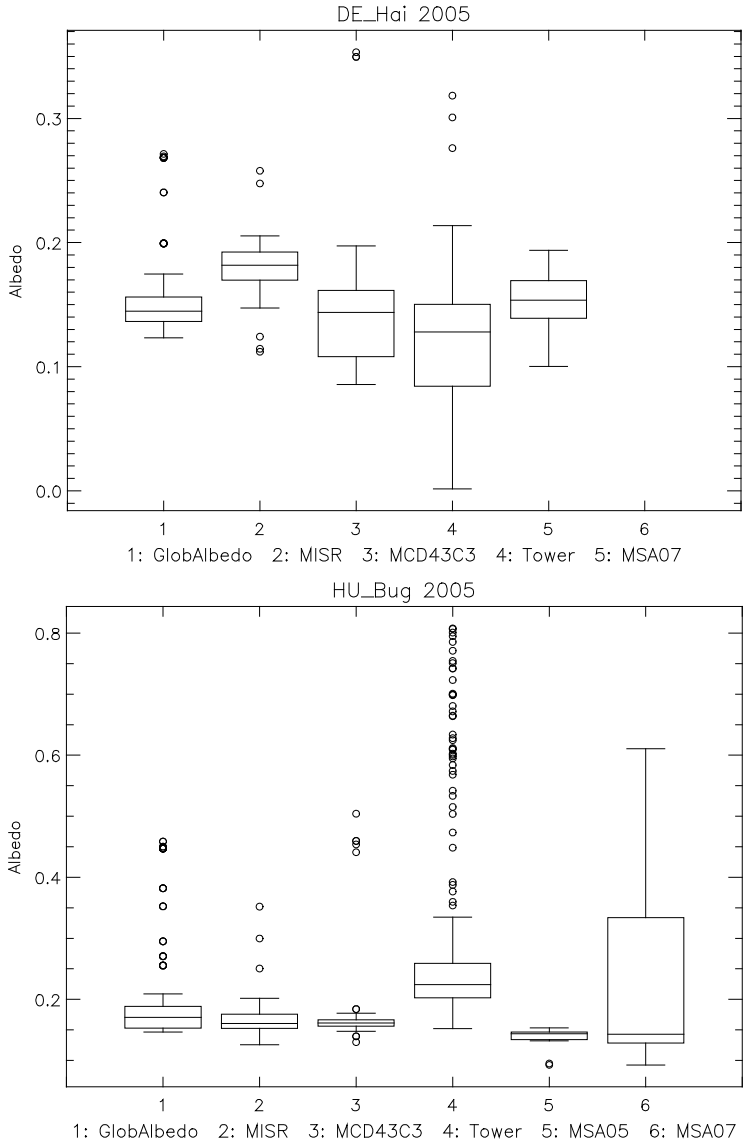


Figure 34: Box-whiskers plots comparing satellite-derived vs. ground-based measurements of the surface albedo at two FLUXNET sites. All satellite retrievals are in their original spatial resolution. The 90% probability criterion has been applied to MSA data. Values outside the 12.5 – 87.5 percentile range are shown as small circles.

These plots indicate that there are surface-dependent systematic biases between some of the EO data-sets. See for example between GlobAlbedo and MISR on DE_HAI. On average, the satellite-derived surface albedo values are slightly above the ground truth measurements. MSA fits well into the albedo range provided by the other sensors. A different picture is observed for HU_BUG: satellite-derived values systematically underestimate the values measured on ground, with MSA showing the largest deviations. This is a strong indication that the *in situ* measurement is only usable when in the vicinity of the measurement tower.

4.9 Comparison with Surface Reference Sites: Pre-MODIS Era

The following datasets provide *in situ* albedo observations and were used for validation purposes with a special emphasis on the pre-MODIS era: BSRN, Safari-2000, and a series of albedo measurements taken during measurement campaigns in Sudan in 1989. The datasets and their characteristics are listed in Annex A.

The location of the different observation sites on the Meteosat disks is shown in Figure 35. The datasets were quality-controlled and reformatted to facilitate comparing surface albedo estimates with MSA estimates. This format is described in Section 4.9.1. In Section 4.10, the datasets are compared to MSA-retrieved surface albedo.

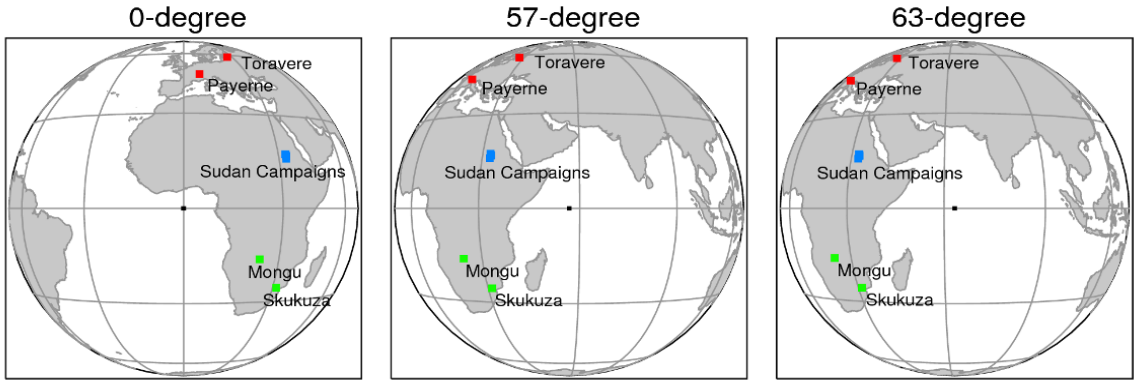


Figure 35: Location of the different validation sites with surface albedo observations predating the MODIS era.

4.9.1 Validation Summary Files

Validation summary files for subsequent use within the validation report have been produced from original data from the BSRN, Safari-2000, and the Sudan Campaigns. These files hold statistical information on *in situ* surface albedo measurements for the 10-day MSA time periods. Table 10 summarizes the information provided. The validation files are available either as NetCDF or IDL.sav files.

Name	***Type***	***Description***
JUL	Double	Julian Day (IDL JULDAY-Function Format)
DOY	Integer	Day of Year (1 … 361)
MONTH	Integer	Month
DAY	Integer	Day
YEAR	Integer	Year
MEDIAN	Float	Median value of valid in situ albedo observations within 10-day period
MEAN	Float	Mean value of valid in situ albedo observations within 10-day period
MIN	Float	Minimum value of valid in situ albedo observations within-10 day period
MAX	Float	Maximum value of valid in situ albedo observations within-10 day period
Q25	Float	25% Quartile of valid in situ albedo observations within 10-day period
Q75	Float	75% Quartile of valid in situ albedo observations within 10-day period
IQR	Float	Interquartile range of valid in situ albedo observations within 10-day period
SDEV	Float	Standard deviation of valid in situ albedo observations within 10-day period
N	Long	Number valid albedo observations within 10-day period

Table 10: Validation summary file format. Time information refers to the first day of each 10-day MSA period.

4.10 Comparison with MSA

Data from all stations was compared for individual ten-day periods both for 0DEG and IODC areas. The different combinations of sites, years, and coverage areas led in total to 47 similar annual plots for individual observation geometries and years. Figure 36 compares three consecutive years of MSA observations to surface albedo measurements taken at Mongu (Zambia) during Safari-2000. The equivalent figures for the other 44 annual plots are not shown in this final report but are distributed separately in the form of image files.

The following main conclusions can be drawn by comparing MSA to surface albedo *in situ* data:

- Residual cloud contamination is clearly identifiable in the MSA data. For example, see January 2000 in Figure 36;
- The agreement between MSA and the *in situ* data deteriorates in the winter months at higher latitudes due to variable snow cover and low sun height;
- In situations not affected by clouds and/or unfavourable illumination conditions, the agreement between *in situ* measurements in large homogeneous surfaces and MSA data is well within the temporal standard deviation of the ground-based observations in almost all cases;
- The *in situ* albedo is expected to adopt a value between the black-sky (DHR_{30}) and white-sky (BHR_{ISO}) albedos. This is not always the case, but the three albedo values often agree within their ranges of uncertainty for the ten-day periods;
- The 10-day variability of the *in situ* data–in situations not affected clouds, snow, or unfavourable illumination conditions–is typically in the range of 3% -5% for the Safari-2000 sites and about 10% for the BSRN stations Payerne and Toravere.

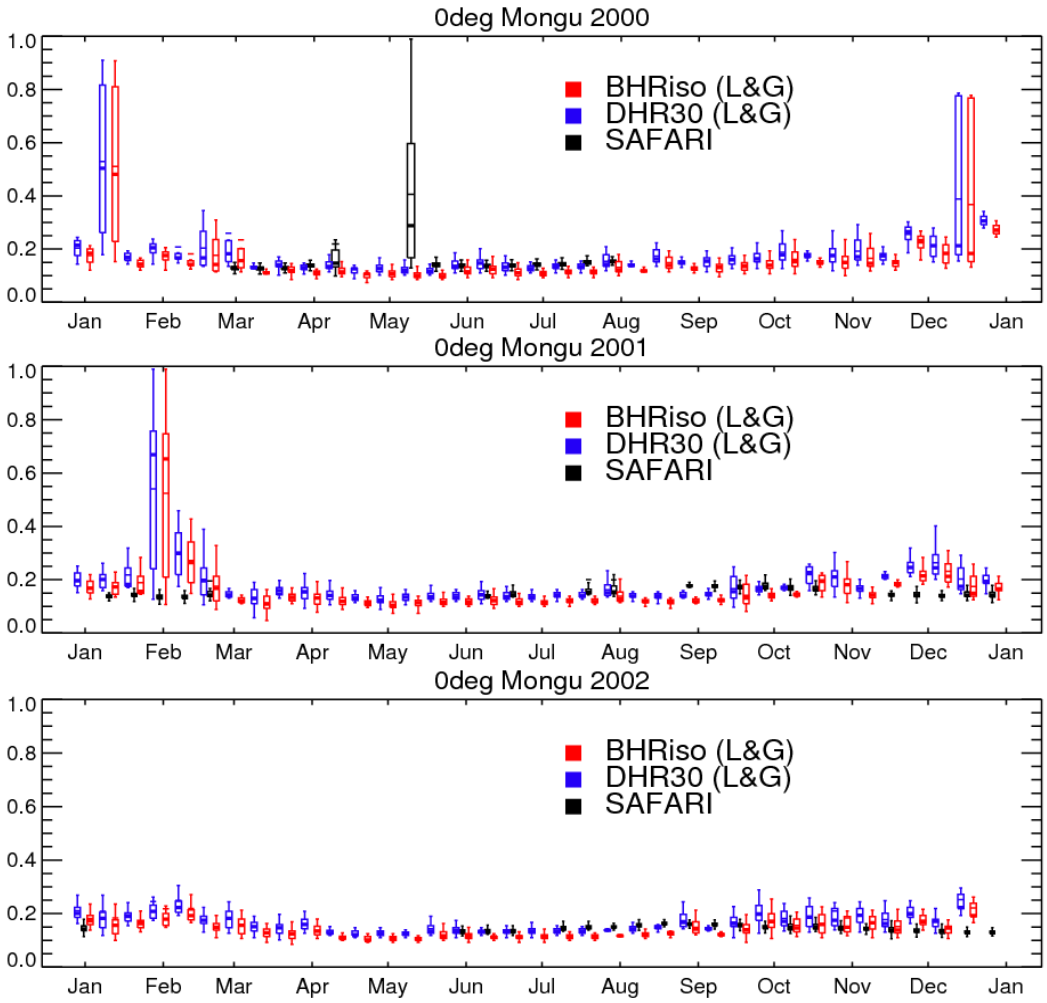


Figure 36: Comparison of MSA versus in situ albedo observations. The box-and-whisker diagrams represent the spatial variability of the MSA observations (Loew and Govaerts [2010] coefficients applied) within a 3 × 3 window centred at Mongu (Zambia). For the in situ observations (black), the diagrams represent the temporal variability within a ten-day observation period.

5 SUMMARY AND CONCLUSIONS

5.1 Summary of findings

5.1.1 General findings

- Depending on surface type and a number of external parameters, the albedo of a specific surface target may undergo significant short-term, daily and seasonal variations;
- Surface albedo retrievals from directional space-borne observations are further complicated by the need to account for atmospheric effects and surface anisotropy;
- The possibility for satellite-based surface albedo retrieval is generally reduced due to insufficient illumination at higher latitudes in the winter months and, more importantly, due to frequent cloud cover in several parts of the world, such as the mid-latitudes in winter and tropical areas in the ITCZ;
- Systematic surface albedo retrieval errors occur for complex surface types. For example, the albedo of a snowy coniferous forest is underestimated at off-nadir geometries with the instrumental field-of-view being filled by dark snow-free trees out of proportion to their number;
- A validation of the MSA product in the strictest sense was not possible since the effective reflective properties of potential reference areas sufficiently large for direct pixel-wise MSA validation are unknown;
- The MSA data record was produced using MVIRI data produced during near real-time operations. As a consequence, the MSA product encompasses a range of different image navigation and rectification procedures. These have shown to have only a minor impact on product quality.
- Different sets of product requirements on the surface albedo for climate applications have been established by GCOS and WMO:
    - The GCOS requirements on the surface albedo aim to detect a change in radiative forcing with an accuracy of 0.1 Wm^{-2}. The resulting accuracy requirement on the surface albedo (maximum 5%; 0.0025) appears difficult to achieve from space-borne observations. In contrast to this, the stability requirement (a maximum of 1%; 0.0001) is within the reach of space-borne surface albedo retrievals. See also the ***Note*** below:
    - The WMO observing requirements database distinguishes between the three requirement levels “threshold”, “breakthrough” and “goal”. All levels are within the reach of space-borne surface albedo retrievals or have already been met;

Note: The stability requirement is not entirely rational: The *relative* 1% criterion gives higher values than the *absolute* 0.0001 criterion for surfaces with albedo values greater than 0.01 (1% of 0.01 equals to 0.0001). Even the darkest surfaces on Earth are characterised by albedo values greater than 0.01. This means that the 0.0001 stability criterion never applies in practice. To make it equivalent to the accuracy requirement, the GCOS stability requirement should read “(maximum of 1%, 0.0005)”.

5.1.2 MSA Strengths

- The chosen scientific approach is simple, robust and well-documented in scientific literature;
- With only a few short gaps, MSA data are available between August 1981 and July 2006 for the 0° coverage (0DEG) and since July 1998 for the Indian Ocean data coverage (IODC);
- A wealth of additional information is provided through the MSA ancillary files allowing user-specific in-depth analysis or post-processing of the MSA product;
- Scene-to-scene as well as MVIRI-to-MVIRI geo-location accuracy is on the order of ± 1-1.5 pixels both horizontally and vertically. Only Meteosat-3 images appear systematically shifted by 1.5 to 2 scan lines at the top of the image.
- No significant artefacts are observed in satellite-to-satellite transitions when applying the new spectral-to-broadband conversion factors provided by Loew and Govaerts [2010];
- The MSA data record agrees well with corresponding values from both satellite-derived and ground-based observing systems under many observation conditions;
- MSA long-term observations are very consistent and have been shown to match the GCOS stability requirement of 1% per decade for a number of desert reference surfaces.
- For specific WMO observing requirements:
    - In its current version, MSA already meets the “threshold” requirements of the WMO observing requirements database on spatial resolution (10 km) and temporal resolution (30 d);
    - Based on plausibility requirements, we assume the “threshold” uncertainty requirement (± 0.1 ΔA) is also being met;
    - MSA has the potential to reach the “breakthrough” level for temporal resolution (3d) and probably also uncertainty (± 0.07 ΔA) if the relevant suggested improvements listed below are implemented.

5.1.2 MSA Weaknesses

- The most obvious quality issue concerns undetected clouds visible as spikes in MSA time series and also as regions of high albedo in time-animated visualisations. Undetected clouds usually result in an overestimation of the surface albedo and may thus create a systematic bias;
- Likely due to the cloud contamination issue highlighted above, MSA shows a greater spatial and temporal variance than other EO-derived albedo products (MODIS, GlobAlbedo). This accentuates the necessity for an optimised cloud screening;
- When using the recommended threshold of TOA BRF = 0.6 to eliminate potentially cloud contaminated pixels, snow-covered surfaces are also often filtered out. This affects MSA availability and representativeness for concerned areas like Siberia (IODC);
- The 90% probability threshold criterion to identify high quality values recommended in the MSA Product User Manual removes good values while letting invalid (mostly cloud-contaminated) values pass. An additional filtering step has been recommended for a better removal of invalid pixels;

- Surface desert targets shown to be temporally stable in long-term time series show short-term deviations in the MSA product between +10% and -20%, depending on aerosol load, surface brightness, and observation geometry. The observed pattern seems to indicate that the aerosol path radiance is, on average, insufficiently removed;
- Some surfaces show large MSA differences between 0DEG and IODC observation geometries. Besides aerosol-related effects, we infer that insufficiently characterised surface anisotropy is the main reason for this observed behaviour;
- Due to the size of the MSA pixels, reference targets of precisely-known surface albedo are not available. This limits the ability to evaluate MSA with absolute accuracy. Based on plausibility considerations, we assume that the GCOS accuracy requirement is not met by MSA;
- BHR_{ISO} values show a higher temporal variability and also a larger dependence on the observation geometry than do DHR_{30} values. The reasons for this unexpected behaviour are still unclear.

5.2 MSA requirement matching

ID	*Requirement*	*Source*	*Match?*
GCMP-SAT_01	Consistent sampling within diurnal cycle	GCOS-154	Y
GCMP-SAT_02	Overlap period for old and new satellite systems	GCOS-154	Y
GCMP-SAT_03	Continuity of satellite measurements	GCOS-154	Y
GCMP-SAT_04	Rigorous pre-launch instrument calibration and characterization	GCOS-154	Depends on satellite
GCMP-SAT_05	On-board calibration adequate for climate system observations	GCOS-154	N, vicarious calibration
GCMP-SAT_06	Sustained operational production of priority climate products	GCOS-154	Not applicable
GCMP-SAT_07	Data systems to facilitate user access	GCOS-154	Y
GCMP-SAT_08	Use of functioning baseline instrument meeting calibration and stability requirements	GCOS-154	Not applicable
GCMP-SAT_09	Complementary in situ baseline observations	GCOS-154	Do not exist
GCMP-SAT_10	Identification of random errors and time dependent biases	GCOS-154	Y
GCOS-HRES	Horizontal resolution (1 km)	GCOS-154	N
GCOS-TRES	Temporal resolution (1-7 days)	GCOS-154	N, but can be achieved
GCOS-ACCU	Accuracy (MAX (5%, 0.0025))	GCOS-154	N, could be considered
GCOS-STAB	Stability (MAX (1%, 0.0001))	GCOS-154	Y, for bright surfaces
WMO_TH_UCRT	Threshold: Uncertainty (10%)	WMO_ORDB	Y, for bright surfaces
WMO_TH_HRES	Threshold: Horiz. resolution (10 km)	WMO_ORDB	Y
WMO_TH_OBCY	Threshold: Observing cycle (30 d)	WMO_ORDB	Y
WMO_TH_TIME	Threshold: Timeliness (90 d)	WMO_ORDB	N, but can be achieved

Table 11: This is essentially the same table as Table 1. The last column on the right has been added to indicate if theMSA product matches a particular requirement, either Y or N or Not applicable.

Other related findings:

There are very few *in situ* measurements available that meet these specific needs for evaluating the accuracy of satellite-retrieved global surface albedo products:

- Measurements taken at sufficient height above ground ≥ 50 m;
- Reference surfaces homogeneous at the 0.5 km to 5 km level;
- Reference sites covering a variety of different land cover types, especially for dark targets.

This lack of information severely limits the ability to evaluate the absolute accuracy of most space-borne surface albedo products. A network of dedicated reference sites providing the required information in a harmonised form online would greatly facilitate this and other important task(s). FLUXNET covers a limited number of such reference sites with observations dating back to 1995. Unfortunately, the Baseline Surface Radiation Network (BSRN) which is an activity of the World Climate Research Programme (WCRP) does not provide the data required for evaluating space-based surface albedo retrievals, as most stations are located in heterogeneous terrain and albedo measurements are being taken close to the surface.

5.3 Conclusions

The MSA data record is a unique data set encompassing up to 25 years of continuous surface albedo coverage for large areas of the Earth. It is therefore of paramount importance to maintain and further improve the existing MSA data record.

The evaluation of the MSA data record has revealed a number of specific strengths and weaknesses as outlined above. While the strengths highlight the already high value of the MSA data record for climate applications, the weaknesses need to be considered for specific applications and should be addressed in the context of a product re-processing.

In combination with other geostationary satellites, both EUMETSAT and all others, the MSA method should contribute to creating harmonised surface albedo records of quasi-global coverage outside the polar zones serving climate applications and beyond. Going further, geostationary and polar-orbiting observations may be fused to provide multi-mission albedo products of higher product quality and full global coverage, capitalizing on the strengths of both approaches.

ANNEX A

A.1 Reference data

A.1.1 *In situ* Surface Albedo

Data set	Domain	Parameter	Spatial cov.	Spatial res.	Temporal cov.	Temporal res.	Terms	Comment	Utility	Effort
Baseline Surface Radiation Network (BSRN)	In situ	Up- and downwelling SW flux; surface albedo	Global, most stations situated in Europe and the US	~100 m²	Station dependent, can be long-term, can be multi-year	Minutes	Free access for non-commercial users	Only two BSRN stations (Toravere, Payerne) provide routine albedo within Meteosat disk. Albedo data maybe also available for Cabauw.	High for consistency analysis due to long time series. Limited for direct validation (small footprint, taken above heterogeneous surfaces).	Low. Data available and processing method established.
Free University Berlin - Sudan	In situ	Spectral albedo (0.5-1.6 µm)	Sudan, 15N-17N, 32E-33E	~100 m², some profiles (4-5 sites within 2-3 km)	Individual dates in 1988 and 1989	Individual measurements, diurnal courses	Free access for ALBEDOVAL	Ca. 90 measurements at ca. 40 sites, some taken in homogeneous areas covering several MSA pixels.	High. Among the sparsly available pre-EOS in situ data. Partly covering homogeneous arid surfaces.	Low to high. Limited amount of processed data available. Processing of raw data needs to be re-established.
Free University Berlin - Various	In situ	Spectral albedo (0.5-1.6 µm, broadband albedo	Germany, Spain, Italy, Niger, France	~100 m²	Individual dates and short periods from 1987 to 1992	Individual measurements, diurnal courses	Free access for ALBEDOVAL	Data and related tools not easily accessible since relevant staff has retired.	Medium. Among the sparsly available pre-EOS in situ data. Often taken above heterogeneous surfaces.	Medium to high. Some data just need to be digitized from paper, other require full reprocessing.
Safari 2000	In situ	Broadband albedo	South Africa, Zambia	~100 m²	03/00-12/02	15 minutes	Free access for non-commercial users	Only two stations to provide albedo data.	High. Time series covering almost 3 years for rather homogeneous surfaces in Africa.	Medium. Automated processing still to be developed.
FLUXNET	In situ	Broadband albedo	Global, most stations in Europe and the US, some in Africa	Depending on obs. height, up to 50,000 m²	1996-2006	11:00-13:00 local time	Certain stations adhering to "fair use" policy	Albedo taken at heights between 5 and 50 m concomitantly with CO2-flux rate masurements.	High. Long time series partly taken from high towers above homogeneous surfaces.	Low. Data available and processing method established.

A.1.2 Satellite-Derived Surface Albedo

Data set	Domain	Parameter	Spatial cov.	Spatial res.	Temporal cov.	Temporal res.	Terms	Comment	Utility	Effort
LSA-SAF Albedo	Sat	Albedo retrieval from MSG/SEVIRI based on Roujean BRDF model	Meteosat disk, centered at 0° lon	3 km at nadir	From 09/05	Daily	Free access for non-commercial users	Daily values based on 15 min. observations of 0.6, 0.8 and 1.6 µm channels. Atmospheric correction based on forecasts of TCWV and aerosol climatology (replaced by MACC forecasts in 2012).	Medium. Five months overlap with MSA.	Low. Data available and processing methods established.
AVHRR	Sat	Spectral reflectance; Broadband albedo	Europe, 27N-72N, 10W-42E	0.01°	01/89-12/09, can be extended up to now. Above 55N only summer season (04-10)	Daily	Free access for ALBEDOVAL	Data and related tools not easily accessible since relevant staff has retired.	High. Full spatial coverage since 1989, instruments well intercalibrated and navigated.	Medium to High. Data need to be retrieved from old archives and pre-processed according to study needs.
MODIS	Sat	Broadband albedo	Global	500 m and 0.05°	From 03/00	Every 8 days, represent. 16 days	Free access for non-commercial users	Collection 5 to be used, only use first two quality grades.	High. Global coverage, high spatial resolution.	Low. Automated processing methods established.
MISR	Sat	Broadband albedo	Global	1.1 km	From 03/00	Overpass every 16 days near equator, every 3 days near poles	Free access for non-commercial users	Near instantaneous measurements under nine angles.	High. Simultaneous multi-angle retrieval providing uncertainty estimate for actual sky condition.	High. Data processing laborious, data access complicated.
GlobAlbedo	Sat	Broadband albedo	Global	1 km, 0.05° as well as 0.5°	06/98-06(12)/11	Every 8 days, repres. a "halfwidth" of a few days	Free access for GlobAlbedo users	Albedo values derived using optimal estimation approach with input from MERIS, Vegetation, MODIS.	High. Provides uncertainly estimate	Low. Data available and processing methods established.

A.1.3 Ancillary Data

Data set	Domain	Parameter	Spatial cov.	Spatial res.	Temporal cov.	Temporal res.	Terms	Comment	Utility	Effort
GLCC-IGBP	Ancillary	Land cover map derived from AVHRR imagery, 17 LC classes	Global	1 km	1992-1993	does not apply	Free access for non-commercial users	Well established and tested LC map based on almost 20 years old data	High. Allows stratification of MSA data for various analyses.	Low. Data readilly available in GIS-compatible formats.
MACC-II	Ancillary	Re-analysis of AOD at 550 nm for sea salt, dust, organic matter, black carbon, sulphate	Global	1.125°	2003-2010	Daily	Free access for EU-27 non-commercial users.	Most relevant input is MODIS AOD.	High. Allows to investagate aerosol related quality aspects.	Low. Data available and processing methods established.
AERONET	Ancillary	Spectral AOD	Global, most stations in Europe and the US	Does not apply	Depending on actual station, earliest data from 1996	Minutes	Free access for non-commercial users	About 15 stations located within 0° coverage and IODC.	High. Allows to investagate aerosol related quality aspects.	Medium. Automated processing still to be developed

A.1.4 Reference Surface Targets

Name	Country	Lat	Lon	IGBP Land Cover	Homogeneity	Program
DE_Hai	Germany	51.080	10.450	Decidouous broadleaf forest	low	FLUXNET
Egypt_One	Egypt	27.120	26.100	Barren or sparsely vegetated	high	SATCAL
H_NAV_1	Morocco	15.970	52.139	Barren or sparsely vegetated	low	ALBEDOVAL
H_NAV_2	Egypt	20.094	37.206	Barren or sparsely vegetated	average	ALBEDOVAL
H_NAV_3	Egypt	18.030	-16.011	Barren or sparsely vegetated	low	ALBEDOVAL
HU_Bug	Hungary	46.690	19.600	Croplands	low	FLUXNET
Libya	Libya	21.500	28.500	Barren or sparsely vegetated	high	SATCAL
Moldova	Moldova	47.000	28.816	Cropland/natural vegetation	average	AERONET
Mongu	Sambia	-15.438	23.253	Evergreen broadleaf forest	low	SAFARI-2000, AERONET
Murzuq_Desert	Libya	24.750	12.500	Barren or sparsely vegetated	high	SATCAL
Omani_Desert	Oman	19.000	55.500	Barren or sparsely vegetated	high	SATCAL
Skukuza	South Africa	-25.020	31.483	Croplands	high	SAFARI-2000
Solar_Village	Saudi Arabia	24.907	46.397	Open shrublands	low	AERONET
Toravere	Estonia	58.254	26.462	Evergreen needleleaf forest	low	BSRN, AERONET
V_NAV_1	Mauretania	31.354	27.206	Barren or sparsely vegetated	average	ALBEDOVAL
V_NAV_2	Sudan	31.111	33.611	Water bodies	low	ALBEDOVAL
V_NAV_3	Yemen	27.976	-12.646	Barren or sparsely vegetated	average	ALBEDOVAL

Table 12: Selection of reference surface targets used for the MSA quality assessment purposes. Only targets explicitly mentioned in this report are listed. The homogeneity definition can be found in Section 3.4.2. The full list of surface targets considered for this study is available in a separate Excel spreadsheet.

ANNEX B: GCOS CLIMATE MONITORING PRINCIPLES

The GCOS Climate Monitoring Principles (GCMPs) to ensure the effectiveness of climate monitoring systems are listed in Figure 37 below [GCOS-143, 2010].

GCMP-GEN_01. The impact of new systems or changes to existing systems should be assessed prior to implementation.

GCMP-GEN_02. A suitable period of overlap for new and old observing systems is required.

GCMP-GEN_03. The details and history of local conditions, instruments, operating procedures, data processing algorithms and other factors pertinent to interpreting data (i.e., metadata) should be documented and treated with the same care as the data themselves.

GCMP-GEN_04. The quality and homogeneity of data should be regularly assessed as a part of routine operations.

GCMP-GEN_05. Consideration of the needs for environmental and climate-monitoring products and assessments, such as IPCC assessments, should be integrated into national, regional and global observing priorities.

GCMP-GEN_06. Operation of historically-uninterrupted stations and observing systems should be maintained.

GCMP-GEN_07. High priority for additional observations should be focused on data-poor regions, poorly-observed parameters, regions sensitive to change, and key measurements with inadequate temporal resolution.

GCMP-GEN_08. Long-term requirements, including appropriate sampling frequencies, should be specified to network designers, operators and instrument engineers at the outset of system design and implementation.

GCMP-GEN_09. The conversion of research observing systems to long-term operations in a carefully-planned manner should be promoted.

GCMP-GEN_10. Data management systems that facilitate access, use and interpretation of data and products should be included as essential elements of climate monitoring systems.

Figure 37: GCOS Climate Monitoring Principles (GCMPs) to ensure effective climate monitoring systems.

ANNEX C: MSA TIME SERIES AT SELECTED SITES

C.1 Murzuq Desert

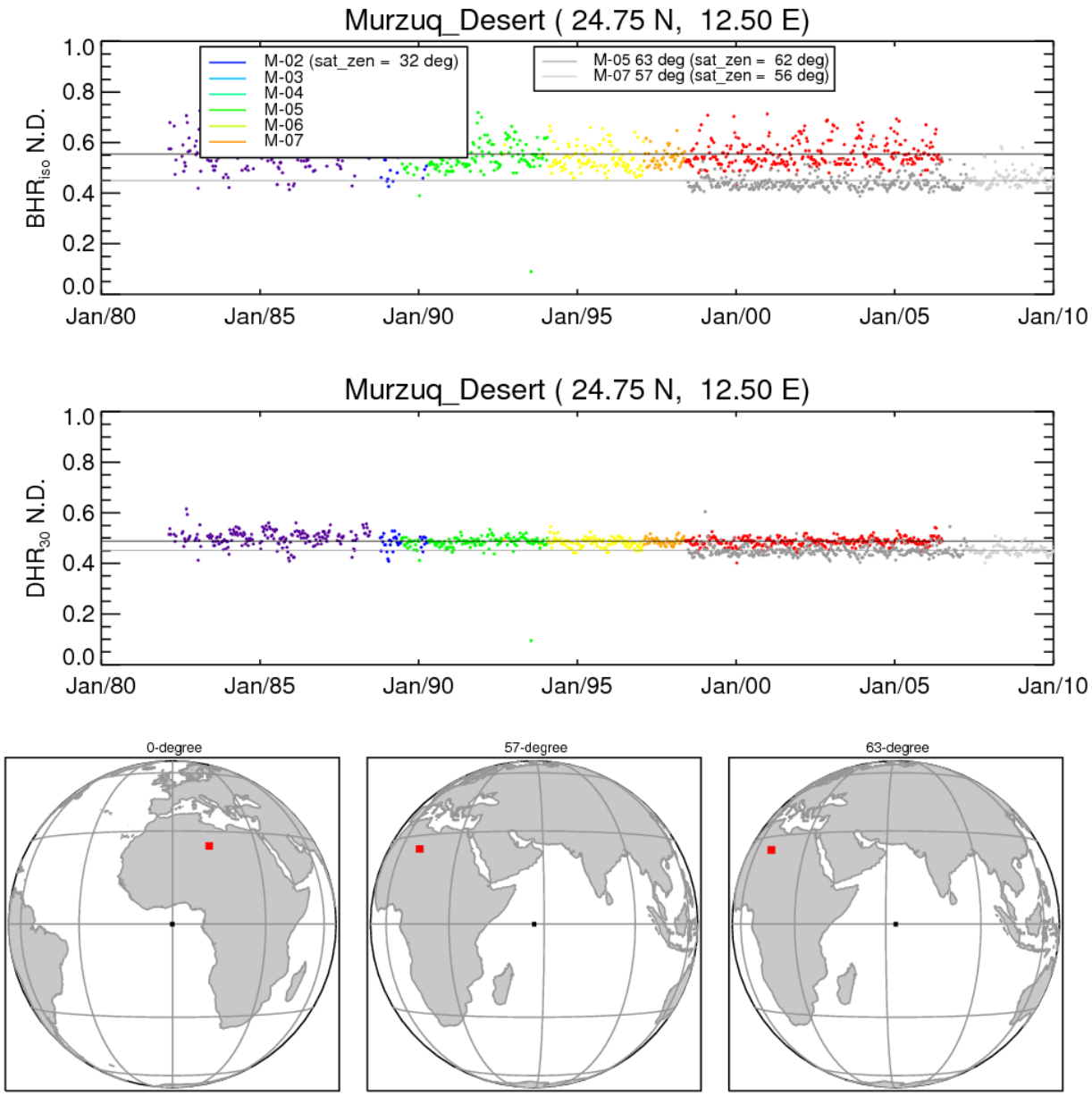


Figure 38: Long-term time series of BHR_{ISO} and DHR_{30} for the Murzuq Desert site. The lower three plots show the position of the target site on the respective 0-degree and IODC disks. The coloured dots show pentad averages for 0-degree coverage, the grey dots for IODC coverage. The dark and light-grey lines show the long-term averages for the two coverage areas.

C.2 Libya

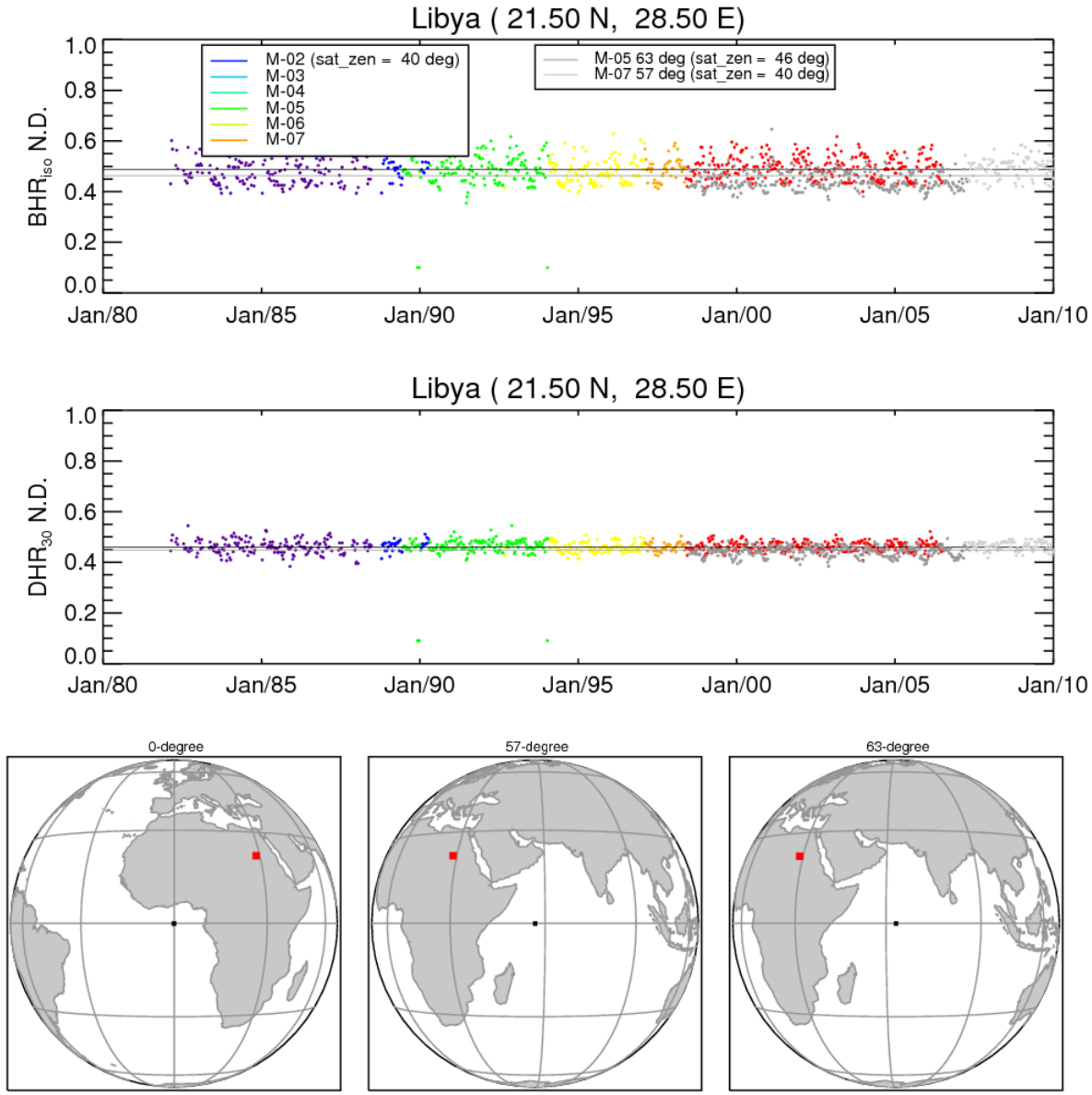


Figure 39: Long-term time series of BHR_{ISO} and DHR_{30} for the Libyan Desert site. The lower three plots show the position of the target site on the respective 0-degree and IODC disks. The coloured dots show pentad averages for 0-degree coverage, the grey dots for IODC coverage. The dark and light-grey lines show the long-term averages for the two coverage areas.

C.3 Egypt One

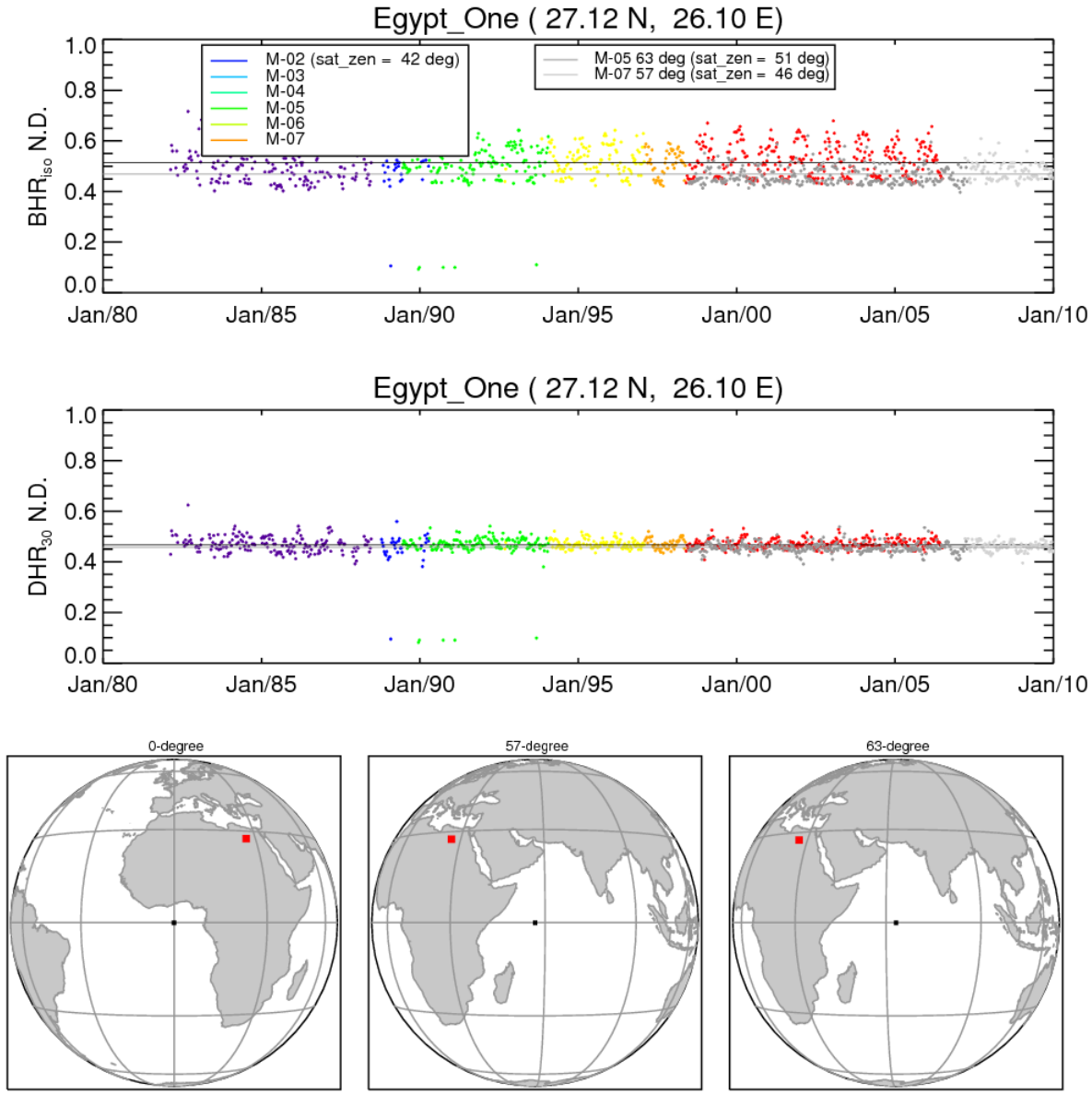


Figure 40: Long-term time series of BHR_{ISO} and DHR_{30} for the Egypt One site. The lower three plots show the position of the target site on the respective 0-degree and IODC disks. The coloured dots show pentad averages for 0-degree coverage, the grey dots for IODC coverage. The dark and light-grey lines show the long-term averages for the two coverage areas.

C.4 Omani Desert

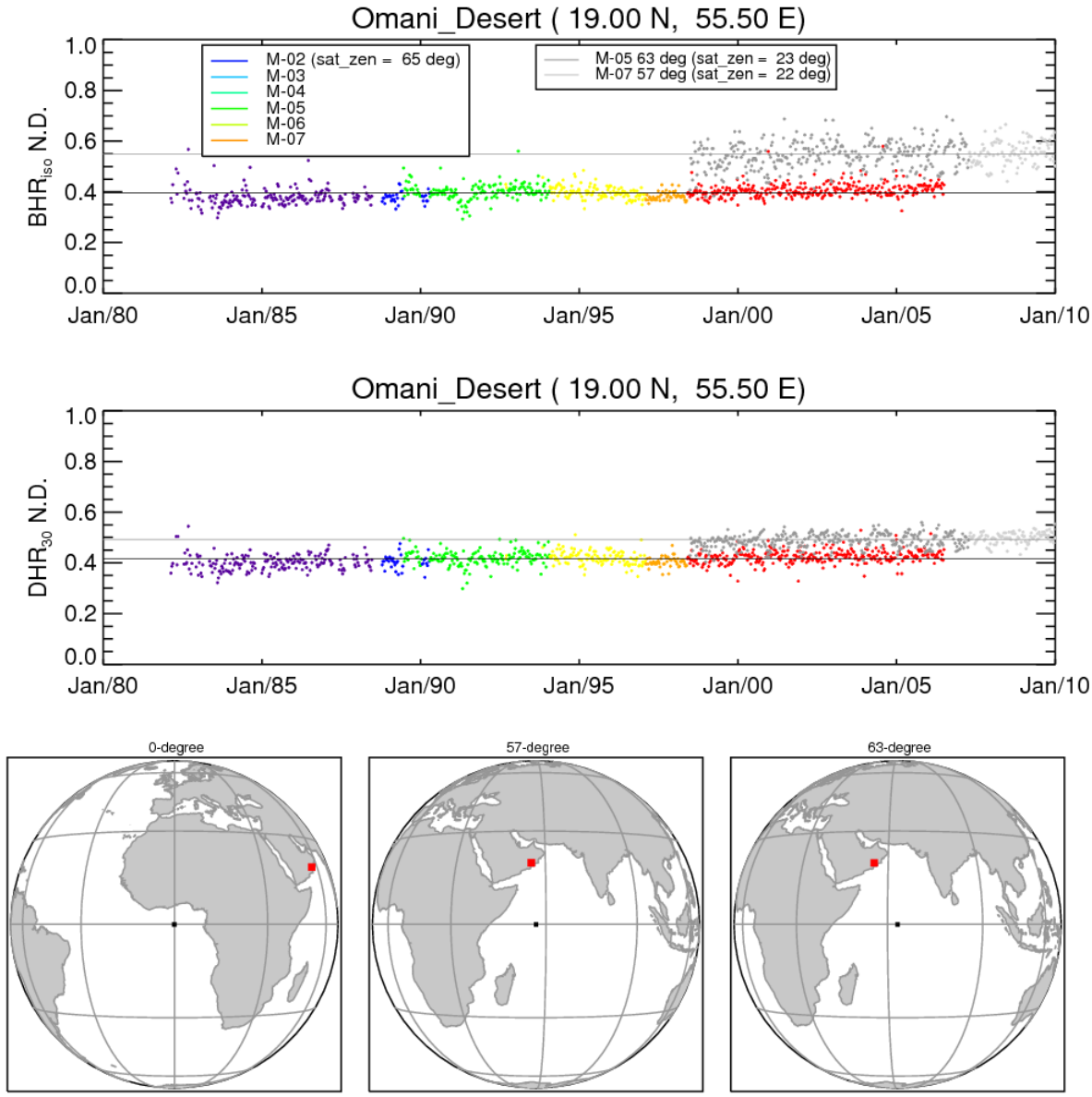


Figure 41: Long-term time series of BHRISO and DHR30 for the site Omani Desert site. The lower three plots show the position of the target site on the respective 0-degree and IODC disks. The coloured dots show pentad averages for 0-degree coverage, the grey dots for IODC coverage. The dark and light-grey lines show the long-term averages for the two coverage areas.

C.5 Toravere

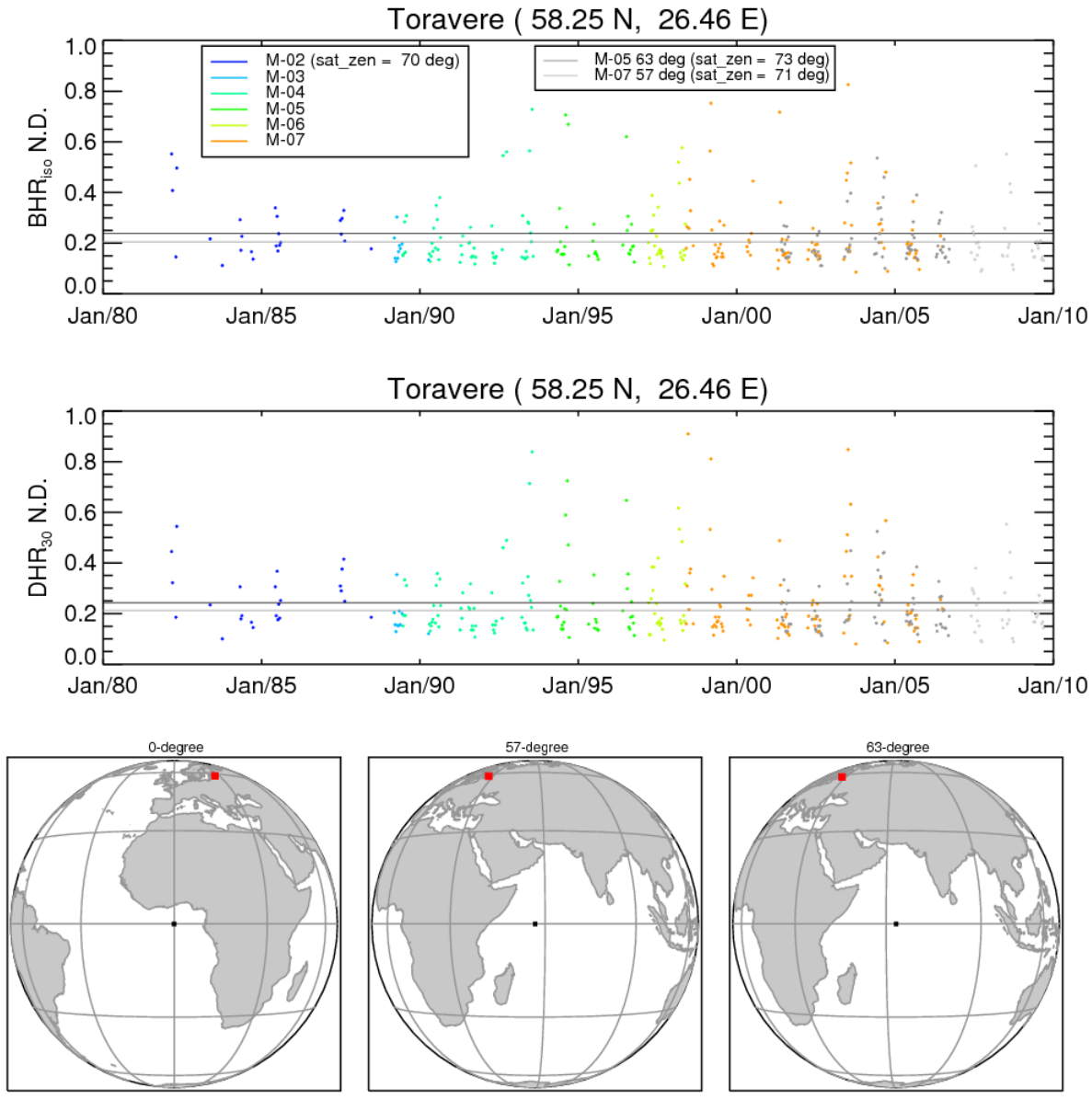


Figure 42: Long-term time series of BHRISO and DHR30 for the Toravere, Estonia site. The lower three plots show the position of the target site on the respective 0-degree and IODC disks. The coloured dots show pentad averages for 0-degree coverage, the grey dots for IODC coverage. The dark and light-grey lines show the long-term averages for the two coverage areas. Note the observation gaps in winter and residual cloud contamination.

C.6 Moldova

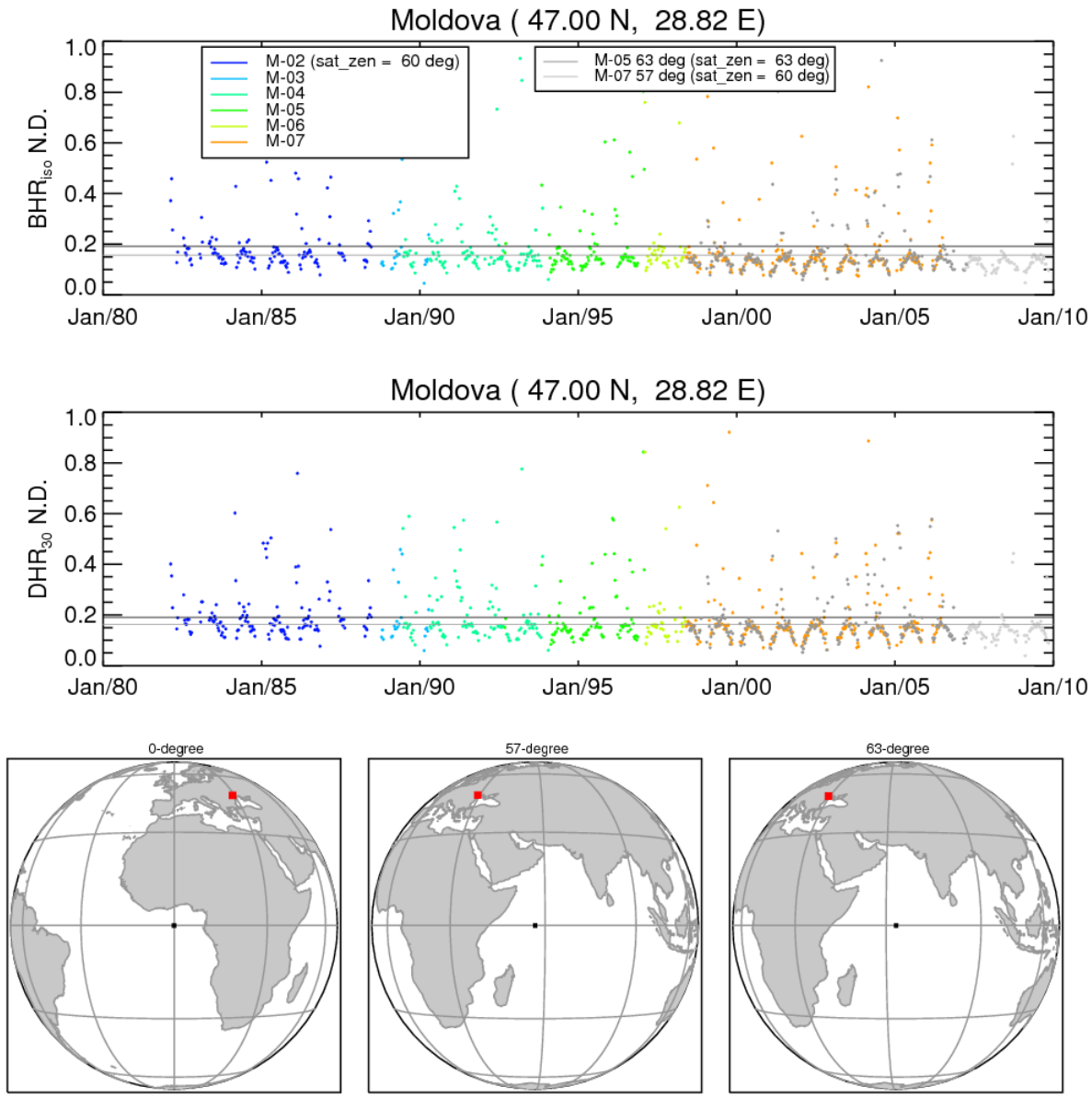


Figure 43: Long-term time series of BHRISO and DHR30 for the Moldova site. The lower three plots show the position of the target site on the respective 0-degree and IODC disks. The coloured dots show pentad averages for 0-degree coverage, the grey dots for IODC coverage. The dark and light-grey lines show the long-term averages for the two coverage areas.

C.7 Mongu

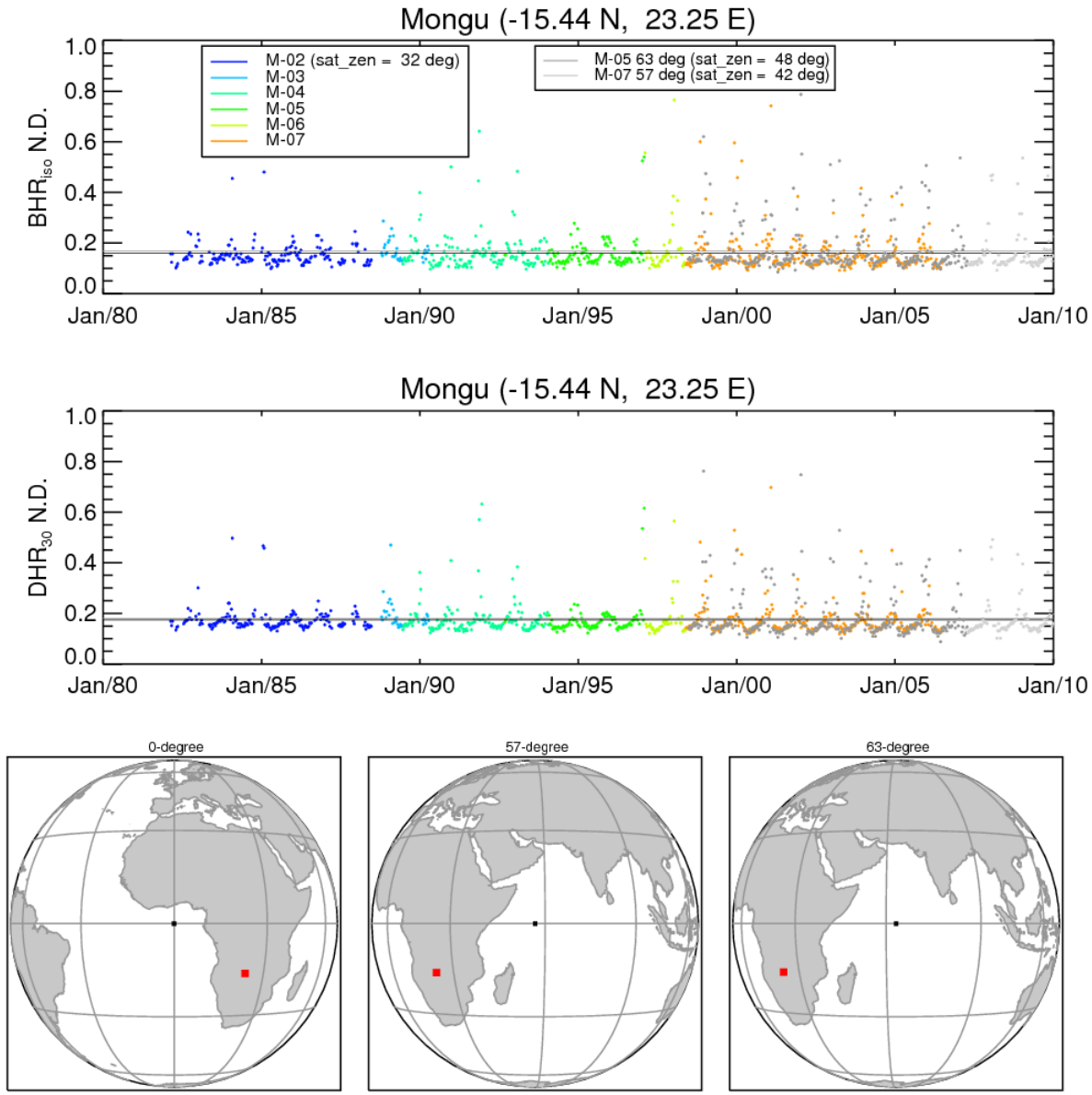


Figure 44: Long-term time series of BHRISO and DHR30 for the Mongu, Zambia site. The lower three plots show the position of the target site on the respective 0-degree and IODC disks. The coloured dots show pentad averages for 0-degree coverage, the grey dots for IODC coverage. The dark and light-grey lines show the long-term averages for the two coverage areas.

C.8 Skukuza

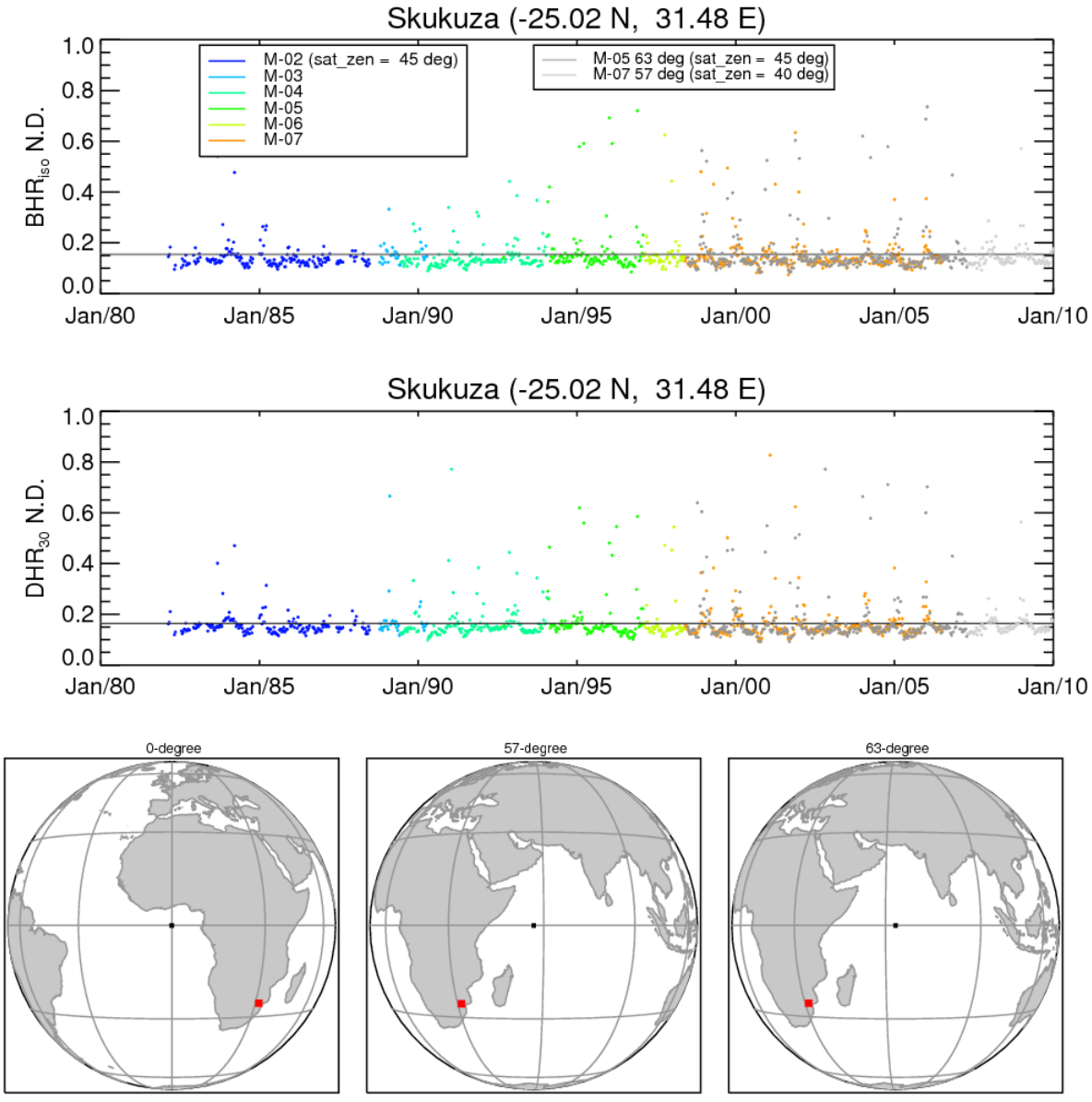


Figure 45: Long-term time series of BHRISO and DHR30 for the Skukuza, South Africa site. The lower three plots show the position of the target site on the respective 0-degree and IODC disks. The coloured dots show pentad averages for 0-degree coverage, the grey dots for IODC coverage. The dark and light-grey lines show the long-term averages for the two coverage areas.

C.3 Solar Village

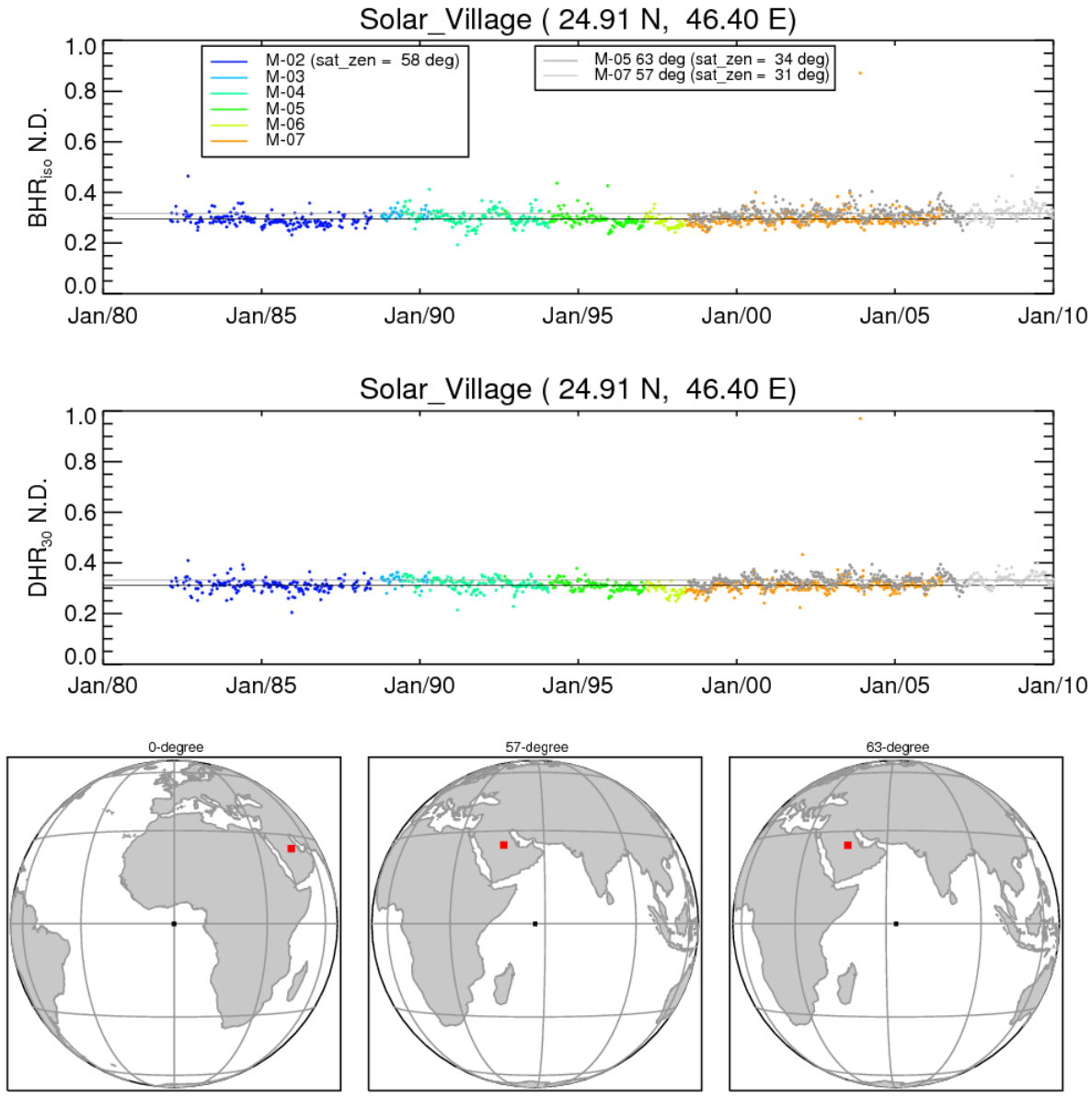


Figure 46: Long-term time series of BHRISO and DHR30 for the Solar Village, Saudi Arabia site. The lower three plots show the position of the target site on the respective 0-degree and IODC disks. The coloured dots show pentad averages for 0-degree coverage, the grey dots for IODC coverage. The dark and light-grey lines show the long-term averages for the two coverage areas.

APPENDIX D: GEOREFERENCING SOFTWARE

D.1 MPEF_georef.pro: latitude/longitude to column/row

Mapping latitude/longitude to column/row is performed using the routine `MPEF_georef.pro` using the following calling sequence:

```
IDL> flag = MPEF_georef (lat,lon,column,row,/vis)
```

Output `flag =0` indicates no error has occurred.

To access the correct pixels in the MSA data file corresponding to the chosen latitude/longitude, the column and row values for the MVIRI full disk resulting from `MPEF_georef.pro` must be converted as follows:

```
Column_MSA = column_MVIRI – startpixel
Row_MSA    = row_MVIRI    - startline
```

where the values of `startline` and `startpixel` are given in Table 13:

Coverage	*Rows*	*Columns*	*Startline (Row)*	*Startpixel (column)*
0 deg	3842	3261	919	400
IODC_57	4358	4662	470	167
IODC_63	3794	4485	941	278

Table 13: Image dimensions of the different MSG coverage areas as well as the position of the lower left corner on the full MVIRI disk.

There are three optional keywords controlling the behaviour of the `MPEF_georef.pro`:

- `/VIS`: force the “visible” resolution (default: IR)
- `/SATLON`: set longitude of satellite (default: 0°)
- `/MSG`: set parameters to match MSG (default: MFG)

D.2 MPEF_refgeo.pro: column/row to latitude/longitude

To convert a given row/column location on the MSA 3261 x 3842 (0DEG) data field into latitude/longitude, the routine `MPEF_refgeo.pro` is invoked with the following calling sequence:

```
IDL> flag = MPEF_refgeo (column + startpixel,row +
              startline,lat,lon,/vis)
```

Output flag =0 indicates no error in conversion. Note that “`startpixel`” and “`startline`” need to be added as the routine requires the position in the MVIRI 5000 × 5000 full disk.

Keywords `to MPEF_refgeo.pro` are identical to those to `MPEF_georef.pro.`

D.3 Georeferencing Example

To illustrate some issues related to geo-location and to address some apparent inconsistencies between the IDL geo-location routines and the static geo-location files, the following test was run at the example of the BSRN Toravere site (Figure 47):

Test:

A 20 × 20 km^2 "neighbourhood" was subdivided into a grid of 800 × 800 points, equivalent to a spacing of 25 meters. For each of those grid points, the corresponding MVIRI pixel was determined using the IDL routines provided by EUMETSAT. At the same time, the pixel location of Toravere was calculated using the following criteria:

1. The IDL geo-location routines provided by EUMETSAT, and
2. A "nearest neighbour" search in the static files associated with the MSA product.

Outcome:

- If a nearest neighbour search for Toravere is performed on the MSA Static files, the pixel corresponding to the yellow dot will be obtained.
- If the location of Toravere is calculated using the IDL routines, the pixel corresponding to the blue dot will be obtained.
- These results are consistent. The discrepancy is caused by the slanted observation geometry of MFG and the actual location of Toravere (red dot) in the far corner of the pixel corresponding to the blue dot.
- This study also suggests that the geo-location routines map to the centre of a pixel and not the lower left corner. See the yellow and blue dots in the centre of their respective pixel.

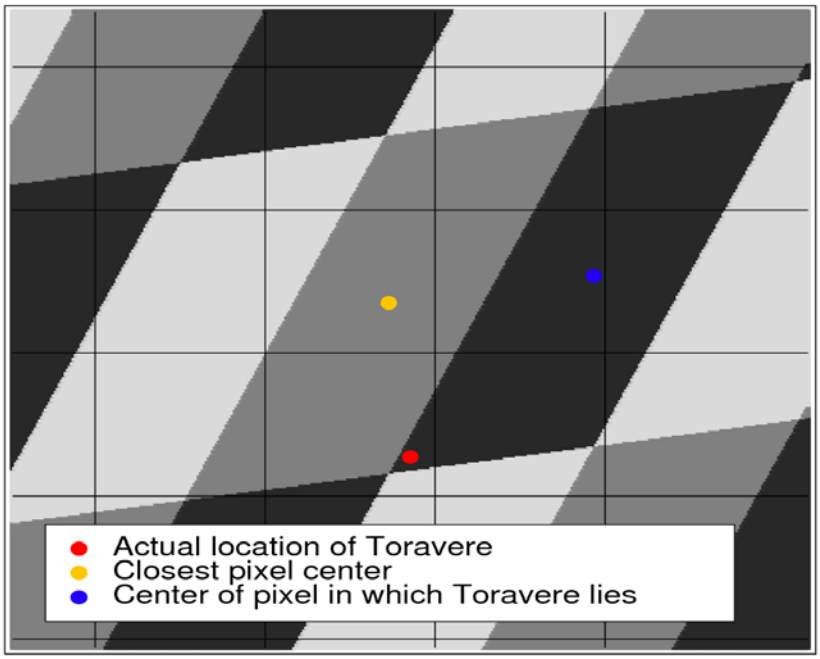


Figure 47: Location and orientation of the MVIRI pixels around the Toravere (Estonia) reference site at 58.254 N/ 26.462 E. The different grey-shaded areas represent the different MVIRI pixels. The horizontal and vertical lines are spaced at 2.5 km distance in the meridional and zonal directions. The yellow dot represents the pixel centre closest to Toravere and the blue dot indicates the centre of the pixel which contains Toravere.

APPENDIX E: SCIENTIFIC REFERENCES

Author	*Title*	*Publisher*
Belward, A. S. (1996).	*The IGBP-DIS global 1 km land cover data set (DISCover) – proposal and implementation plans.*	IGBP-DIS Office, Météo-France, Toulouse, France, 61 pp.
Benedetti, A., J.W. Kaiser and J.-J. Morcrette (2011)	*[Global Climate] Aerosols [in "State of the Climate in 2010"]*	BAMS, 92(6) pp. 65-67
Bolle, H. J., et al.	*EFEDA: European Field Experiment in a desertification-threatened area*	Ann. Geophys., 11, 173-189
Bolle, H.-J.; Eckardt, M; Koslowsky, D.; Maselli, F.; Menenti, M. ; Meliá-Miralles, J.; Olesen, F.-S.; Petkov, L.; Rasool, I.; Van de Griend, A.; Editors (2006).	*Mediterranean Land-surface Processes Assessed from Space*	Springer-Verlag Berlin Heidelberg, ISBN 9783540401513; 9783540453109
Braverman, A., and L. Di Girolamo (2002).	*MISR global data products: a new approach.*	IEEE Trans. Geosci. Remote Sens. 40, 1626-1636.
Buriez, J.C., Parol, F., Cornet, C., Doutriaux-Boucher,	*An improved derivation of the top-of-atmosphere albedo from POLDER/ADEOS-2 narrow-band albedos.*	M. (2005JGR-Atmos., 110, D05202, doi:10.1029/2004JD005243.
Camacho, F., Sanchez, J., Lacaze, R., Schaaf, C., Cescatti, A. (2012).	*Validation of GEOLAND-2 global albedo products based on SPOT/VEGETATION observations.*	Geophysical Research Abstracts 14, EGU2012-3474.
Cescatti, A., Marcolla, B., Vannan, S.K.S., Pan, J.Y., Roman, M.O., Yang, X., Ciais, P., Cook, R.B., Law, B.E., Matteucci, G., Migliavacca, M., Moors, E., Richardson, A.D., Seufert, G., Schaaf, C.B.	*Intercomparison of MODIS albedo retrievals and in situ measurements across the global FLUXNET network.*	Remote Sens. Environ. 121, 323-334.
Csiszar, I., and G. Gutman (1999).	*Mapping global land surface albedo from NOAA AVHRR.*	J. Geophys. Res., 104(D6), 6215–6228, doi:10.1029/1998JD200090.
Dee et al., 2011:	*The ERA-Interim reanalysis: configuration and performance of the data*	Quart. J. Roy. Meteorol. Soc., 137,

Author	*Title*	*Publisher*
	assimilation system.	553-597, DOI:10.1002/qj.828.
Engelsen, O., Pinty, B., Verstraete, M. M., and Martonchik, J. V., 1996,	*Parametric bidirectional reflectance factor models: Evaluation, improvements and applications.*	Report of the Joint Research Centre of the European Commission, EU 16426, Ispra, Italy.
EUMETSAT, 2010-A.	*Meteosat Surface Albedo Fact Sheet: Version 1*	EUMETSAT, Darmstadt, Germany.
EUMETSAT, 2010-B	*Meteosat Surface Albedo (MSA) Product User's Manual and Format Guide,*	24 pp, EUMETSAT, Darmstadt, Germany
EUMETSAT, 2011-A	*Meteosat First Generation User Handbook. Report,*	40 pp, EUMETSAT, Darmstadt, Germany
EUMETSAT 2011-B	*GSICS MVIRI-IASI Inter-calibration Uncertainty Evaluation. Report,*	EUMETSAT, Darmstadt, Germany.
Fell, F. (1991).	*Ein Test der aus Satellitendaten in den Spektralbereichen der AVHRR-Kanäle eins und zwei bestimmten Bodenalbedo durch vergleichende Bodenmessungen im Sudan. Diploma thesis,*	91 pp., Inst. f. Meteorologie, Freie Universität Berlin, Germany.
Fell, F., Bennartz, R., Cahill, B., Lattanzio, A., Muller, J.-P., Schulz, J., Shane, N., Trigo, I. and Watson, G. (2012).	*Evaluation of the Meteosat Surface Albedo Climate Data Record (ALBEDOVAL),*	Final Report, 119 pages.
GCOS-138 (2010).	*Implementation Plan for the Global Observing System for Climate in Support of the UNFCCC (2010 Update),*	WMO, Geneva, Switzerland.
GCOS-143 (2010).,	*Guideline for the Generation of Datasets and Products Meeting GCOS*	WMO, Geneva, Switzerland.
GCOS-154 (2011).,	*Systematic Observation Requirements for Satellite-based Products for Climate Supplemental details to the satellite-based component of the Implementation Plan for the Global Observing System for Climate in Support of the UNFCCC - 2011 Update*	WMO, Geneva, Switzerland
Geiger, B., Carrer, D., Franchisteguy, L., Roujean,	*Land Surface Albedo Derived on a Daily Basis From Meteosat Second*	Remote Sensing 46, 3841-3856

Author	*Title*	*Publisher*
J.-L., Meurey, C. (2008).	*Generation Observations. IEEE Trans. Geosci.*	
Govaerts, Y.M., Lattanzio, A., Pinty, B., Schmetz, J. (2004).	*Consistent surface albedo retrieval from two adjacent geostationary satellites.*	Geophys. Res. Lett. 31
Govaerts, Y.M., Pinty, B., Taberner, M., Lattanzio, A. (2006).	*Spectral conversion of surface albedo derived from meteosat first generation observations.*	IEEE Geoscience and Remote Sensing Letters, 3(1), 23-27.doi : 10.1109/LGRS.2005.854202
Govaerts, Y., and Lattanzio, A. (2007).	*Retrieval Error Estimation of Surface Albedo Derived from Geostationary Large Band Satellite Observations: Application to Meteosat-2 and -7 Data.*	Journal of Geophysical Research 112, doi:10.1029/2006JD007313.
Govaerts, Y.M., Lattanzio, A., Taberner, M., Pinty, B. (2008).	*Generating global surface albedo products from multiple geostationary satellites.*	Remote Sens. Environ. 112, 2804-2816.
Knuteson, R. O., and H. E. Revercomb (2004).	*Land surface temperature and emissivity from advanced sounders. 2004 EUMETSAT Meteorological Satellite Conference, Prague, Czech Republic.*	Proceedings. EUMETSAT, Darmstadt, Germany, 2004, pp.241-247. Reprint #4269.
Lattanzio, A., Y. Govaerts, et al. (2006).	*Consistency of surface anisotropy characterization with Meteosat observations.*	Advanced Space Research, doi:10.1016/j.asr.2006.02.049.
Leroy, M., Deuze, J., Breon, F., Hautecoeur, O., Herman, M., Buriez, J., Tanre, D., Bouffies, S., Chazette, P., Roujean, J. (1997).	*Retrieval of atmospheric properties and surface bidirectional reflectances over land from POLDER/ADEOS.*	JGR-Atmos. 102, 17023-17037.
Loew, A., and Y. Govaerts (2010).	*Towards multidecadal consistent Meteosat surface albedo time series,*	Remote Sensing, 2(4), 957-967.
Martonchik, J., Diner, D., Pinty, B., Verstraete, M., Myneni, R., Knyazikhin, Y., Gordon, H. (1998).	*Determination of land and ocean reflective, radiative, and biophysical properties using multiangle imaging.*	IEEE Trans. Geosci. Remote Sensing 36, 1266-1281.
McPeters, R. D., S. M. Hollandsworth, L. E. Flynn, J. R. Herman, and C. J. Seftor (1996).	*Long-term ozone trends derived from the 16-year combined Nimbus 7/Meteor 3 TOMS Version 7 record,*	Geophys. Res. Lett., 23(25), 3699–3702, doi:10.1029/96GL03540.
Muller, J.-P., López, G., Watson, G., Shane, N.S.,	*The ESA GlobAlbedo Project for mapping the Earth's land surface albedo*	IEEE Geoscience and Remote

Author	Title	Publisher
Tom Kennedy, T.E., Lewis, P., Fischer, J., Guanter, L., Domench, C., Preusker, R., North, P.R., Heckel, A., Danne, O., Krämer, U., Zühlke, Z., Brockmann, C. (2012-B).	*for 15 Years from European Sensors.,*	Sensing Symposium (IGARSS) 2012. IEEE, Munich, Germany, 22-27.7.12.
Ohmura, A., Dutton, E.G., Forgan, B., Frohlich, C., Gilgen, H., Hegner, H., Heimo, A., Konig-Langlo, G., McArthur, B., Muller, G., Philipona, R., Pinker, R., Whitlock, C.H., Dehne, K., Wild, M. (1998).	*Baseline Surface Radiation Network (BSRN/WCRP): New precision radiometry for climate research*	Amer. Meteorol. Soc. 79, 2115-2136.
Pinty, B., Roveda, F., Verstraete, M.M., Gobron, N., Govaerts, Y., Martonchik, J.V., Diner, D.J., and Kahn, R.A. (2000-A):	*Surface albedo retrieval from Meteosat: Part 1: Theory*	Journal of Geophysical Research, 105, 18099-18112.
Pinty, B., Roveda, F., Verstraete, M.M., Gobron, N., Govaerts, Y., Martonchik, J.V., Diner, D.J., and Kahn, R.A. (2000-B):	*Surface albedo retrieval from Meteosat: Part 2:*	Applications, Journal of Geophysical Research, 105, 18113-18134.
Pinty, B., A. Lattanzio, J. V. Martonchik, M. M. Verstraete, N. Gobron, M. Taberner, J.-L. Widlowski, R. E. Dickinson, and Y. Govaerts (2005):	*Coupling Diffuse Sky Radiation and Surface Albedo.*	J. Atmos. Sci., 62, 2580–2591. doi: http://dx.doi.org/10.1175/JAS3479.1
Rahman, H., B. Pinty, and M. M. Verstraete (1993).	*Coupled surface-atmosphere reflectance (CSAR) model. 2. Semi-empirical surface model usable with NOAA Advanced Very High Resolution Radiometer data,*	Journal of Geophysical Research, 98, 20,791-20,801.
Rao, C. R. N., J. Chen, J. T. Sullivan, and N. Zhang (1999).	*Post-launch Calibration of Meteorological Satellite Sensors,*	Advances in Space Research, 23(8), 1357-1365.
Roujean, J.L., and Lacaze, R. (2002).	*Global mapping of vegetation parameters from POLDER multiangular measurements for studies of surface-atmosphere interactions: A pragmatic method and its validation.*	JGR-Atmos, 107, 4150, doi:10.1029/2001JD000751.

Author	*Title*	*Publisher*
Schaaf, C.B., Gao, F., Strahler, A.H., Lucht, W., Li, X.W., Tsang, T., Strugnell, N.C., Zhang, X.Y., Jin, Y.F., Muller, J.P., Lewis, P., Barnsley, M., Hobson, P., Disney, M., Roberts, G., Dunderdale, M., Doll, C., d'Entremont, R.P., Hu, B.X., Liang, S.L., Privette, J.L., Roy, D. (2002). First operational BRDF, albedo nadir reflectance products from MODIS. Remote Sens. Environ. 83, 135-148.	*First operational BRDF, albedo nadir reflectance products from MODIS.*	Remote Sens. Environ. 83, 135-148.
Schaaf, C.B., J. Cihlar, A. Belward, E. Dutton, and M. Verstraete, 2009.	*Albedo and Reflectance Anisotropy, ECV-T8: GTOS Assessment of the status of the development of standards for the Terrestrial Essential Climate Variables,*	ed., R. Sessa, FAO, Rome.
Schaaf, C., Martonchik, J., Pinty, B., Govaerts, Y., Gao, F., Lattanzio, A., Liu, J., Strahler, A.H., Taberner, M. (2008).	*Retrieval of Surface Albedo from Satellite Sensors. Advances in Land Remote Sensing: System, Modelling, Inversion and Algorithms,*	Ed. S. Liang, 219-243.
Trigo, I., Freitas, S., Barroso, C., Macedo, J., Perdigão, R., Silva, R., Viterbo, P. (2012).	*Radiation Products based on a constellation of Geostationary Satellites.*	Geophysical Research Abstracts 14, EGU2012-7883.
Vermote, E., D. Tanré, J. L. Deuzé, M. Herman, and J. J. Morcrette, 1997:	*Second simulation of the satellite signal in the solar spectrum: An overview.*	IEEE Trans. Geosci. Remote Sens., 35–3, 675–686.
Wild, M., Ohmura, A., Gilgen, H., Morcrette, J.J., Slingo, A. (2001).	Evaluation of downward longwave radiation in general circulation models.	J. Clim. 14, 3227-3239. WMO (2006). WMO Commission for Instruments and Methods of Observation (WMO/CIMO) Guide to Meteorological Instruments and Methods of Observation. Preliminary seventh edition. Report WMO-No. 8, Geneva, Switzerland

APPENDIX E

Acronyms and Terms Used in this Document

Acronym	*Meaning*
ADC	Atlantic data coverage
AERONET	AErosol RObotic NETwork
AVHRR	Advanced Very High Resolution Radiometer
ASM	Atmospheric scattering module
BHR	Bi-hemispherical reflectance
BRDF	Bi-directional reflectance distribution function
BRF	Bi-directional reflectance factor
BSRN	Baseline Surface Radiation Network
CDR	Climate data record
CORINE	Coordination of Information on the Environment
DCP	Data consistency procedure
DHR	Directional hemispherical reflectance
DIM	Data interpretation module
ECMWF	European Centre for Medium-Range Weather Forecasts
ECV	Essential climate variable
ERA-Interim	ECMWF Re-Analysis Interim
ESA	European Space Agency
EUMETSAT	European Organisation for the Use of Meteorological Satellites
FAPAR	Fraction of absorbed PAR
FCDR	Fundamental climate data record
FUB	Freie Universität Berlin
GCMPs	GCOS climate monitoring principles
GCOS	Global Climate Observing System
GMS	Geostationary Meteorological Satellite (Japan)
GOES	Geostationary Operational Environmental Satellite (US)
GSA	Geostationary Surface Albedo
GSICS	Global Space-based Inter-Calibration System
IGBP	International Geosphere-Biosphere Programme
IODC	Indian Ocean data coverage
ITCZ	Intertropical convergence zone
JMA	Japan Meteorological Agency
LSA SAF	Land Surface Analysis Satellite Applications Facility

Acronym	*Meaning*
LUT	Look-up table
MFG	Meteosat First Generation
MISR	The Multi-angle Imaging SpectroRadiometer
MODIS	Moderate Resolution Imaging Spectroradiometer
MSA	Meteosat Surface Albedo
MVIRI	Meteosat Visible and Infra-Red Imager
NOAA	National Oceanic and Atmospheric Administration
PFT	Plant functional type
RMSE	Root mean square error
SAF	Satellite Applications Facility
SCOPE-CM	Sustained, Co-Ordinated Processing of Environmental Satellite Data for Climate Monitoring
SEVIRI	Spinning Enhanced Visible Infra-Red Imager
SRB	Surface radiation budget
SSP	Sub-satellite point
SSR	Sensor spectral response
TAM	Time averaging module
TCDR	Thematic climate data record
VIS	Visible part of the spectrum
WMO	World Meteorological Organization
XADC	Extended ADC